Università degli Studi di Cagliari

PHD DEGREE
Chemical Science and Technology

Cycle XXXIII

TITLE OF THE PHD THESIS

Synthesis and characterizations of new organic molecules luminescent for applications in lighting and bioimaging

Scientific Disciplinary Sector

CHIM/06 – Organic Chemistry

PhD Student: Andrea Cocco

Supervisor   Prof. Francesco Secci

Co-Supervisor   Prof. Carlo Ricci

Co-Supervisor   Prof. Eli Zysman-Colman

Final exam. Academic Year 2019/2020
Thesis defence: January 2022 Session

Abstract

In recent years, devices based on thermally activated delayed fluorescence (TADF) emitters have proven to be the most promising and efficient approach to convert dark triplet states into emissive singlet states.

TADF materials are characterized by a small energy gap between the excited singlet state (S_1) and the excited triplet state (T_1), this gap called ΔE_{ST} is generally less than 0.2 eV. As with phosphorescent emitters, purely organic TADF emitters can recruit excitons from both singlet and triplet states for light emission and thus allow to construct OLED devices reaching 100% internal quantum efficiencies (IQE). An important advantage of these emitters is related with their organic molecular skeleton, thus avoiding the problems associated with the use of heavy metal-based organometallic complexes. Thanks to their unique photophysical properties, organic TADF materials are being studied for a wide range of domains, such as in organic light emitting diodes (OLEDs), solar cells, photocatalysis, etc. Furthermore, TADF-based materials have a unique advantage in some imaging techniques due to their longer life than promptly fluorescent materials. These organic compounds are particularly promising in bioimaging applications due to their low cytotoxicity compared to traditional compounds such as lanthanide complexes.

In the course of this thesis, the synthesis and photophysical characterization of new organic TADF molecules was carried out, specifically new coumarin and spiro structures, candidates for the construction of new OLED and as non-toxic biomarkers with efficient emissions in the blue-green spectral region.

Summary

List of Abbreviations

$CDCl_3$ - Deuterated chloroform

CIE - Commission Internationale de l'Eclairage

CLF -Chloroform

CRI - color rendering index

CT - Intramolecular charge transfer

CV - cyclic voltammetry

DCM – Dichloromethane

DF - Delayed fluorescence

DFT - Density functional theory

DMSO - Dimethyl sulfoxide

DPV - Differential pulse voltammetry

DSSC - Dye-sensitized solar cell

EBU - European Broadcast Union

EDG - Electron donating group

EL - Electroluminescence

EQE - External quantum efficiency

EWG - Electron withdrawing group

HOMO - Highest occupied molecular orbital

HTM - Hole-transport materials

IC - Internal conversion

IQE - Internal quantum efficiency

ISC - Intersystem crossing

LUMO - Lowest unoccupied molecular orbital

NIR - Near infrared

NPs - Nanoparticles

NTSC - National television system committee

OLED - Organic light emitting diode

ORTEP - Oak Ridge Thermal Ellipsoid Plot

PF - Prompt fluorescence

PH - Phosphorescence

PL - Photoluminescence

PLQY - Photoluminescence quantum yield

PMMA - Polimetilmetacrilato

RT - Room temperature

rISC - Reverse intersystem crossing

SBF - Spirobifluorene

SFX - Spiro [fluorene-9,9′-xanthene]

SOC - Spin-orbit coupling

TADF -Thermally activated delayed fluorescence

TDA - Tamm-Dancoff approximation

TD-DFT - Time-dependent density-functional theory

TFA - Trifluoroacetic acid

TGA - Thermogravimetric analysis

TRFI - Time-resolved fluorescence imaging

TTA - Triplet-triplet annihilation

Chapter 1: introduction

1.1 Motivation

Organic luminescent materials, whose luminescence characteristics such as color, emission intensity and duration, have aroused considerable interest both in the academic world and in the industrial scientific community, due to the wide advanced applications in various fields. In particular Thermal Activated Delayed Fluorescence (TADF) have received big attention thanks to the work of Adachi and collaborators since 2012.[1] TADF materials are characterized by a small energy gap between the excited singlet state (S_1) and the excited triplet state (T_1), this gap called ΔE_{ST} is generally less than 0.2 eV. As with phosphorescent emitters, purely organic TADF emitters can recruit excitons from both singlet and triplet states for light emission and thus allow to construct OLED devices reaching 100% internal quantum efficiencies (IQE). An important advantage of these emitters is related with their organic molecular skeleton, thus avoiding the problems associated with the use of heavy metal-based organometallic complexes. Thanks to their unique photophysical properties, organic TADF materials are being studied for a wide range of domains, such as in organic light emitting diodes (OLEDs), solar cells, photocatalysis, fluorescence imaging, biosensing and also in photodynamic therapy.[2] In particular since the first reported purely organic OLED based on a TADF emitter in 2011, huge efforts have been made in order to improve their photophysical performances. Electroluminescent devices based on TADF emitters have become a notable research topic as demonstrated by the remarkable increase in publications in this field from 2011 to present (Figure 1). In addition, an increasing number of studies focusing on biology and medicine have revealed that organic TADF emitters have tremendous potential in diagnostics and therapies applications.[3]
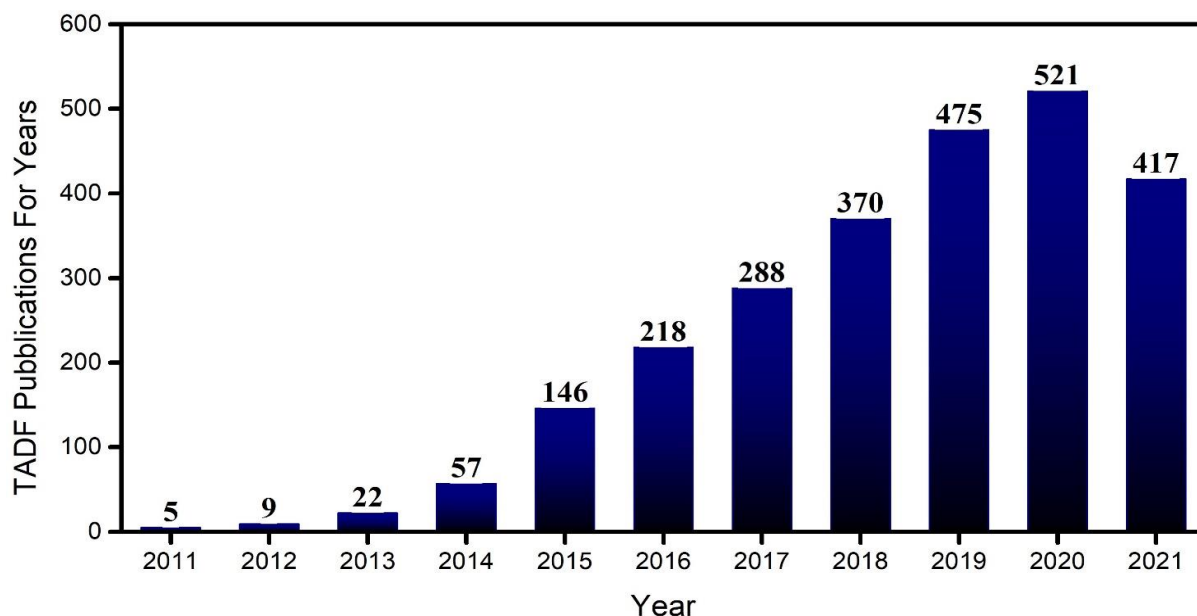
Figure 1. Number of TADF publications per year. Keyword: "thermally activated delayed fluorescence" or "TADF". Scopus search conducted: 03/09/2021.

Organic emitters can be classified into three types in terms of photophysical properties: 1) traditional fluorescent molecules, 2) phosphorescent molecules, and 3) DF delayed fluorescence molecules. Conventional organic fluorophores exhibit short-lived fluorescence with a nanosecond time scale and no exciton formation in the triplet state because intersystem crossing (ISC) process ($S_1 \rightarrow T_1$) is theoretically forbidden. In fact, the intersystem crossing represents a non-radiative process due to the transition between two electronic states with different spin multiplicity. The Pauli exclusion principle implies that two electrons in the same quantum state cannot have parallel spins: following excitation, the formation of a singlet state is favored compared to that of a triplet, which, possessing parallel spins, requires a further transition of spin to form.

In practice, intersystem crossing consists of a process that leads to the formation of an excited state consisting of a pair of unpaired electrons. The probability that this process occurs is all the greater the closer the energy levels of the triplet and singlet state are, with the vibrational sublevels tending to overlap..[4]

In general, the ΔE_{ST} energy gaps of traditional fluorescent molecules are large (> 0.5 eV). Unlike conventional fluorophores, in which singlet excited states are mainly produced, ISC processes in phosphorescent complexes are spin-allowed, leading to a high production of excitons in the triplet state, spin conversion is allowed in organometallic complexes. This type of materials generally exhibit a long-lived emission with a time scale of micro- to milli-seconds. In organic TADF molecules that possess small ΔE_{ST}, the reverse intersystem crossing (rISC) process is possible, generating new singlet excitons that promote delayed fluorescence (DF). The energy level of the S_1 state is usually above that of the T_1 state; therefore, rISC in the TADF process becomes an endothermic process, which makes it thermally activated with stronger delay emission at high temperature. The so produced fluorescence is in the order of microseconds, which makes them very promising candidates for various biomedical applications from fluorescence imaging to photodynamic therapy.

Over the past decade, fluorescence imaging has been proven as a powerful trend for clinical diagnostics due to its distinct advantages, such as high sensitivity, high spatial resolution, and ease of use. However, the development of optical diagnostic agents remains a challenge due to the major drawbacks of signals from autofluorescence and light scattering. To improve signal-to-noise ratios, long-lived fluorescent agents are highly desired to remove interference from short-lived background fluorescence. Heavy metal complexes have been investigated as potential candidates for time-resolved fluorescence imaging (TRFI) due to their advantageous photophysical properties, including relatively long phosphorescence times (in about milliseconds) and the ability to efficiently populate the lowest triplet excited states. However, the cost and high toxicity of heavy metals limits the practical applications of these complexes. For all of these reasons, the

identification of available, economic, non-toxic and tunable organic TADF materials can contribute to open new research fields and solve these challenges.[5]

The research investigations reported in this thesis focuses on the rational design, synthesis and photophysical characterization of new organic TADF molecules and their study for potential for lighting and bioimaging applications.

1.2 Background Theory

The luminescence in organic molecules is a radiative relaxation of excitons from the excited state (S_1, S_2,…, S_n) to the ground state (S_0), which can occur with different multiplicities of spins, such as singlet or triplet excited states and lead to fluorescence and / or phosphorescence, as described in figure 2.[6]
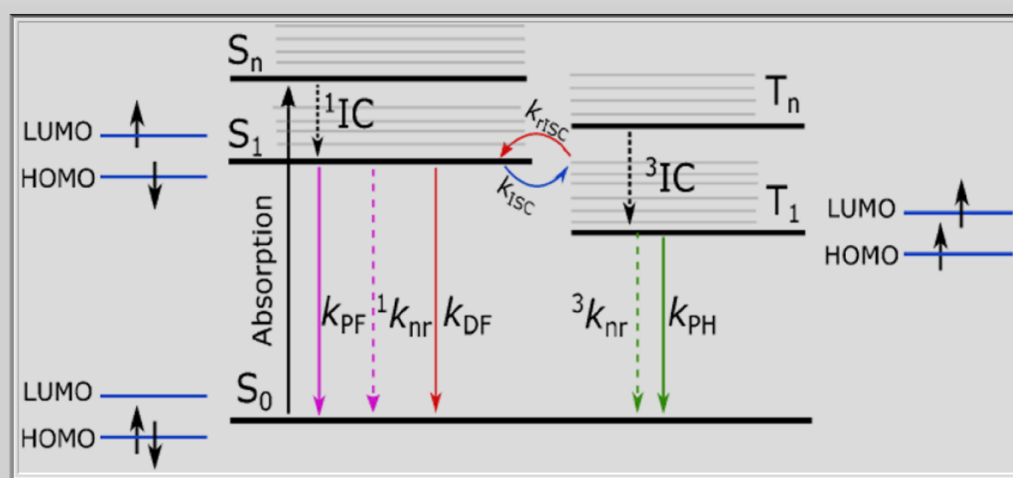
Figure 2. Jablonski diagram

As a matter of fact, after light absorption, various processes can occur. When electrons are promoted to S_n, they usually quickly relax to S_1 (about 10^{-12} s) without photon emission (non-radiative process), this transition is called internal conversion (^1IC). This process is then followed by three distinct processes: 1) radiative emission that produces

prompt fluorescence (PF), a rapidly decaying component (nanosecond interval) with an assigned kinetic constant k_{PF}; 2) non-radiative decay, $^1k_{nr}$; or 3) intersystem crossing (ISC) to triplet states, followed by relaxation to the lowest energy triplet state (^3IC). Once reach the triplet states, T_1 can recombine to the ground state by a formally forbidden radiative emission to spin, referred to as phosphorescence (k_{PH}), non-radiative processes ($^3k_{nr}$), or by further inversion of spin, back to the singlet state, reverse intersystem crossing (k_{rISC}). Phosphorescence is a formally forbidden process but occurs due to spin-orbit coupling (SOC); and as a result, the rate constants for triplet emission are several orders of magnitude smaller than those for fluorescence. Molecules containing heavy atoms such as bromine and iodine could promote phosphorescence as heavy atoms enhance the cross between systems and thus increase the phosphorescence quantum yields. Another type of radiative emission is the delayed fluorescence (DF). The electrons that occupy triplet states after ISC can return to singlet states through various processes such as triplet-triplet annihilation or thermally activated delayed fluorescence and the subsequent decay of S_1 into S_0 producing delayed fluorescence (DF). The DF will therefore have the same spectral shape as that of the prompt fluorescence (as explained in figure 3), but with a much longer duration.[7]
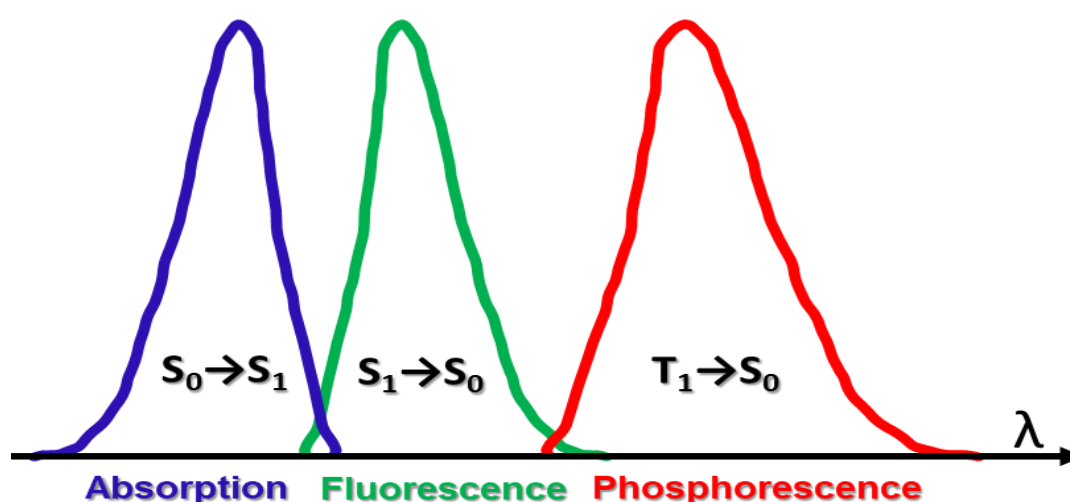
Figure 3. Examples of absorption, fluorescence and phosphorescence spectra.

1.2.1 TADF Story

The first TADF phenomenon reported in organic molecules was found by studying the Eosin Y (Figure 4) photophysical proprieties in 1961.[8] For this reason the recorded delayed fluorescence (DF) was later called DF "type E". Since TADF was discovered as a second emission band with a long duration, apart from the phosphorescence, and showed an identical profile compared to the Eosin rapid fluorescence band: this emission was classified by Parker and Hatchard as DF of the same excited singlet state. Furthermore, investigations on Copper (I) complexes, conducted by McMillin and colleagues suggested another mechanism for the emission of two excited states in thermal equilibrium.[9] However, during the study of fullerenes TADF derivatives in 1996 Berberan-Santos and co-workers described the rate equations that reveal the time-resolved processes for TADF processes.[10]

In these early reports the TADF mechanism was only partially effective, due to a fairly large energy gap ΔE_{ST} (0.37 eV) for eosin. Therefore, there was no clear design rules for the molecular structure to improve the efficiency of TADF. This became the critical point preventing the development of TADF materials. Thus, before 2009 applications for TADF materials were rare and the phenomenon was simply seen as an intriguing photophysical phenomenon. However, the real breakthrough regarding TADF molecules for OLED applications was achieved using pure organic molecules by the Adachi research group in 2012. They described an analysis of quantum mechanics and found that reducing the overlap between the highest occupied molecular orbital (HOMO) and the lowest unoccupied molecular orbital (LUMO) can achieve small ΔE_{ST} for efficient TADF. Following this result, a molecular structure design strategy was proposed, which involve the construction of such molecules with a twisted electron donor-acceptor (D-A) structure caused by the steric clutter of bulky substituents. Host materials containing

TADF molecules are generally excited through the application of a short electrical pulse, to promote the triplet excited state. This approach was first developed by Adachi for the excitation of a Sn (IV)-porphyrin complex OLED based (Figure 4).[11] In 2010 Peters developed an OLED doped with another copper (I) organic metal complex, which exhibits high performance with an external quantum efficiency (EQE_{max}) of 16.1%.[12] These pioneering works have shown that triplet excitons, which represent 75% of the total excitons generated in the device, can be collected very efficiently through the DF channel.
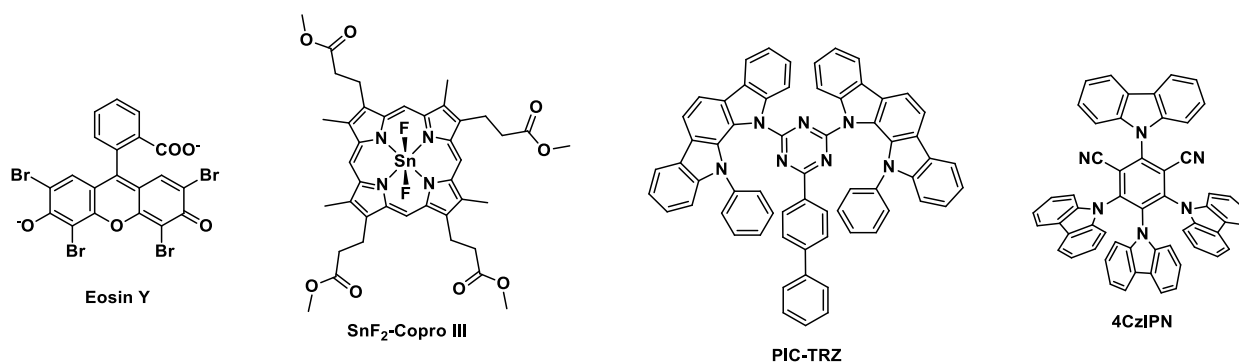
**Figure 4.** Molecular structure of some TADF molecules

On the other hand, devices realized by using other organic molecules such as PIC-TRZ (Figure 4)[13] as emitter layer showed a EQE values of about 5.3%, approaching the theoretical limit of conventional fluorescent molecules. The same group continued to pursue these studies showing a very small ΔE_{ST} along with a high rate of radiative decay of the final S_1 excitons. Again, in 2012 they also reported a series of new and high efficient TADF emitters based on carbazolyl dicyanobenzene (CDCB),[1] showing high photoluminescence efficiencies and a wide range of emission color ranging from blue to orange.

Due to the torsion of the carbazolyl unit with respect to dicyanobenzene, the HOMO and LUMO of these emitters are mainly located on the donor and acceptor parts respectively,

leading to a small ΔE_{ST}. Using these materials for the preparation of multilayer OLED devices, a very high EQE was achieved, of 19.3% for green OLED (4CzIPN, Figure 4) while orange and light blue OLEDs showed EQE values of 11.2% and 8.0% respectively. All of these results highlighted a significant advance over conventional fluorescence-based OLEDs, demonstrating that the use of organic TADF materials in triplet exciton collection by delayed fluorescence could actually help to achieve ultra-high performance OLED devices. In the same period, Adachi and co-worker reported the use of exciplexes formed between donor and acceptor molecules to achieve efficient DF and good OLED performance, with an EQE_{max} close to 10%.[14] It should be noted that exciplexes are well known and represent an undesirable radiative pathway for normal OLEDs. Since the molecular structures are limitless in design and can be easily changed, the emission wavelength can be tuned over the entire visible spectrum, making it ideal for display and lighting applications. Additionally, by avoiding the use of expensive noble metals such as iridium (Ir) and platinum (Pt), pure organic luminescent materials are also cheaper candidates for OLED applications. However, the critical bottleneck of conventional fluorescence-based OLEDs is their low EQE, where the theoretical maximum value should only reach approximately the 5%. Therefore, studies on TADF molecules have opened a new way for the collection of triplet excitons using pure organic dyes which are relatively inexpensive for the fabrication of high-performance OLEDs. Nowadays, the EQE of organic TADF-based OLEDs, where the active emitter layer is made up of pure organic molecules from exciplex systems, can reach values from 20 to 30%. These results are comparable to the best phosphorescent OLED (PHOLED) and TADF materials which are now classified as "third generation emitters".[15]

1.2.2 TADF exciplex

The formation of an exciplex, a complex formed between D and A molecules, is a bimolecular process where an electronically excited species forms a complex with another ground state molecule through coulombic attraction. Generally, the exciplex formation process could be described as follows:

$$D + A + h\nu \rightarrow D^* + A \text{ or } D + A^* \rightarrow (A^{\delta-}D^{\delta+})^* \rightarrow h\nu_{exciplex} + A + D$$
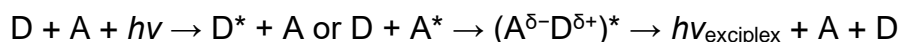
After photoexcitation, the interaction between the donor-based excited-state (D* + A) and acceptor-based excited state (D + A*) creates new electronically excited species (DA)*. The complex formation occurs only in the excited state, as the interaction between the donor and acceptor species in the ground state is repulsive in nature and attractive in the excited state. Therefore, the electronically excited state (DA)* has a minimum on its potential energy surface which corresponds to the exciplex. The exciplex then could either emit radiatively at lower energy than D/A or dissociate into its constituents (D* + A/D + A*).[16] As shown in figure 5, with an efficient RISC process, the emission of electronically excited state ^{1}(DA)* and ^{3}(DA)* of the exciplex involves prompt fluorescence (PF) and DF processes, along with the competition between internal conversion (IC) from S_1 to S_0 and nonradiative transition of triplet excitons from T_1 to S_0.
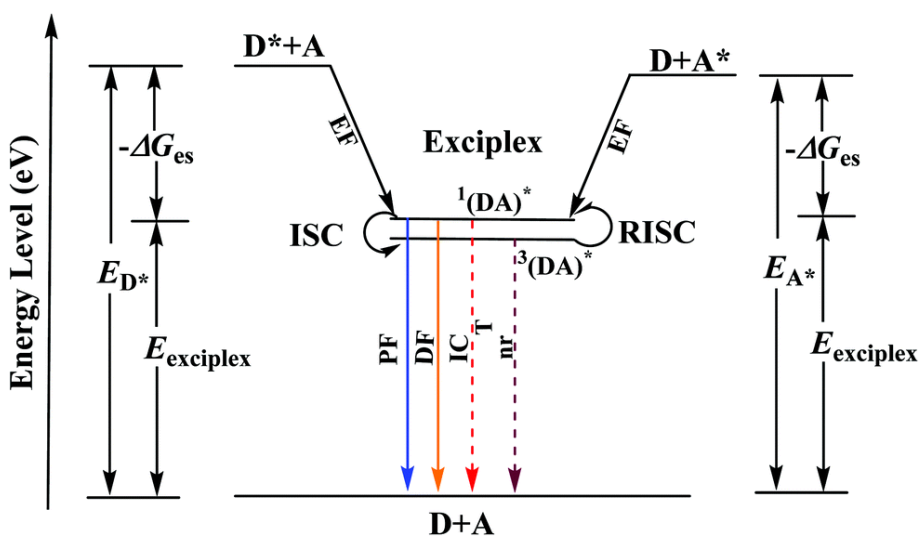
Figure 5. Electronic energy diagrams showing the formation process and working mechanism of a TADF exciplex. EA* and ED* are the exciton energies of the acceptor and donor, respectively; $-\Delta G_{es}$ is the Gibbs energy for exciplex formation, and $E_{exciplex}$ is the exciplex photon energy; EF is the exciplex formation; ISC is the intersystem crossing process from the S_1 to T_1 state; RISC is the reverse intersystem crossing process from the T_1 to S_1 state; PF is the prompt fluorescence process from S_1 to S_0; DF is the delayed fluorescence process from T_1 to S_1, then to S_0; IC is the internal conversion process from S_1 to S_0; and nrT is the nonradiative transition of triplet excitons from T_1 to S_0. Following the development of the TADF exciplex emitters, it can be seen that their EL performance was comparable to that of the current state of the art single molecule TADF emitters. In contrast to single-molecule TADF emitters, exciplex systems can naturally realize relatively small ΔE_{ST} (0–0.1 eV) since their HOMOs and LUMOs are positioned on two different molecules. By introducing specific constituent materials to realize suitable excited-state energy alignments, increase the additional RISC channels, enhance the SOC effect, or optimize the exciton distance and exciton distribution, TADF exciplex emitters have successfully exhibited remarkable EQEs over 20% in OLEDs.[17]

1.2.3 Design of TADF emitters

Efficient TADF molecules must simultaneously satisfy the following conditions: a) show to small energy gap between the singlet and triplet excited states (ΔE_{ST}) b) minimize the non-radiative decay to ensure that the triplet excited state lives long enough to maximize the possibility of triplet collection through the thermally activated inverse intersystem crossing mechanism (rISC), c) maximizing the fluorescence yield. S_0 a small ΔE_{ST} is therefore fundamental to maximize the rISC and therefore its rate constant k_{rISC} given by equation 1:

$$k_{RISC} \propto e^{\frac{\Delta E_{ST}}{k_B T}} \qquad (1)$$

where k_B is Boltzmann constant and T is the temperature.

When calculating the energy of the lowest excited states of singlet (E_{S1}) and triplet (E_{T1}), three different aspects are usually considered: a) the orbital energy (E_{orb}), i.e. the energy associated with an electron's orbital for a given nuclear picture in the excited state, b) the electron repulsion energy (K), this is the first order Coulomb correction, and c) the exchange energy (J), i.e. the first order quantum mechanical correction that it involves the electron-electron repulsion due to the Pauli principle, which affects the two unpaired electrons in the excited state, i.e. one electron in the HOMO and the other in the LUMO. Therefore, for singlet and triplet electronic states with the same electronic configuration, the three components contribute equally. However, due to the different spin arrangement of the excited states of singlet and triplet, the exchange term increases the energy in the S_1 state and decreases it in the T_1 state by the same amount, according to equations (2) and (3). The singlet-triplet energy gap (ΔE_{ST}) is therefore given by the equation (4).

$$E_s = E + K + J \qquad (2)$$

$$E_T = E + K - J \qquad (3)$$

$$\Delta E_{ST} = E_S - E_T = 2J \qquad (4)$$

Where E is orbital energy, K is electron repulsion energy and e J is the exchange energy.

J is defined by the following equation (5):

$$J = \iint \varphi H(r1) \varphi L(r2) \frac{1}{|r2-r1|} \varphi H(r2) \varphi L(r1) dr1 dr2 \qquad (5)$$

where φH and φL are the spatial distributions of the HOMO and LUMO, respectively, and r_1 and r_2 are position vectors. Thus, it follows that reducing the overlap integral

between the HOMO and LUMO decrease both J and ΔE_{ST}. This is achieved by molecules containing portions of electron donors (D) and electron acceptors (A), which promote the transfer of electrons D – A in the excited state. TADF molecules are therefore generally formed by D and A units, linked by an aromatic bridge, and form excited states with a strong CT character. The singlet-triplet energy gap can be further reduced by rotating the D and A units around the axis D – A and obtaining the relative orientation D – A close to orthogonality or, alternatively, by increasing the distance D – A, using a molecular bridge.

Another parameter to consider in TADF molecular design is the oscillator strength f, which is an index for the light emission intensity, which is proportional to the square of the transition dipole moment Q (equation 6):

$$f \propto |Q|^2 \qquad (6)$$

Here, the magnitude of Q also depends on the orbital overlap between the HOMO and LUMO, i.e. (7)

$$Q = \iint \varphi H(r1) \varphi L(r2) |r2 - r1| \varphi H(r2) \varphi L(r1) dr1 dr2 \qquad (7)$$

These equations indicate that a well-tuned partial orbital overlap between the HOMO and LUMO is a requisite condition for obtaining both a small ΔE_{ST} and high PLQY. The molecular design of a D-A pair combined with π-linkers providing a large dihedral angle or π-spacers can separate the HOMO and LUMO with a small orbital overlap.[18]

The donor and acceptor fractions used to design TADF emitters play a critical role in the photophysical properties of TADF molecules and therefore should be carefully selected. The connectivity between units D and A also has a profound impact on the singlet-triplet energy gap and on the rate of the intersystem crossing. In general, the singlet-triplet energy difference is reduced by introducing strong donor and acceptor fractions.

23

However, there are also other ways to further reduce ΔE_{ST}. Twisted geometries around the D – A linker were used to obtain D – A molecules with relative orientation near orthogonality and even smaller ΔE_{ST}. Similar effects can be obtained by increasing the distance D – A. These molecular geometries lead to strongly localized HOMO and LUMO orbitals and therefore to smaller ΔE_{ST} values. Unfortunately, there is a clear trade-off between the efficiency of the rISC mechanism and the electron coupling between the ground state and the excited singlet state. While negligible orbital overlap leads to very small ΔE_{ST}, it also leads to low radiative rates and hence to low photoluminescence quantum yields (Φ_f). Furthermore, weak donors and acceptors induce a less significant HOMO and LUMO localization, which results in a relatively larger singlet-triplet energy gap, thus decreasing the TADF contribution.[19]

Further research is therefore needed to find structures with well-balanced ΔE_{ST} and Φ_f values. A strong contribution of TADF with relatively high fluorescence yields is, in principle, also obtainable in molecules using a weak donor combination, coupled with a stronger electron acceptor unit. In these cases, several weak donors are often used to enhance the donor character of the TADF molecule while maintaining a relatively high fluorescence yield. The most frequently used combinations of electron donor and acceptor units in TADF compounds are derivatives of the molecules shown in Figure 6.
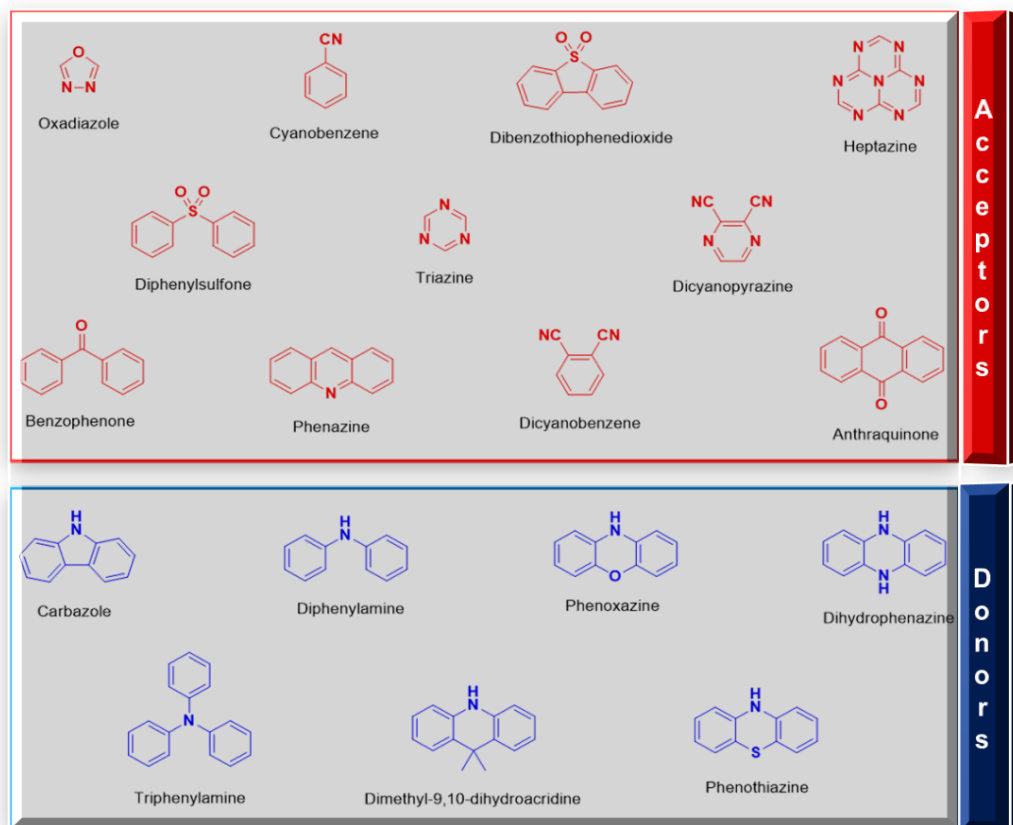
Figure 6. Molecular structures of the most common electron donor and acceptor units used in TADF molecules, acceptors (red) and donors (blue).

Despite significant advances in the development of TADF molecules in recent years, further studies are needed to design molecular structures with better regulation of their emission and improved stability. Most of the TADF molecules have emission in the green region. However, some blue emitters and some red emitters have been reported recently, but of course more structures are needed in these spectral regions. The design of blue TADF emitters is difficult because they require small ΔE_{ST}, while keeping the emission in blue. This requires the use of weak donors and acceptors, so the charge transfer (CT) emission is not strongly shifted to lower energies. The red TADF emitters are particularly limited, as the excited states are strongly affected by the non-radiative decay, in accordance with the energy gap law. This decay competes actively with the rISC mechanism and turns off the population of the excited state, leading to lower

quantum yields. Further molecular design is therefore required to obtain blue and red emitters with small ΔE_{ST} and greatly minimizing non-radiative decay.[20]

1.2.4 TADF Mechanism

The photophysics involved in the TADF mechanism is best perceived when the luminescence of these emitters is studied using time-resolved methods. Following the excitation with a fast laser pulse, the luminescence in the TADF molecules shows a fast component, identified as prompt fluorescence (PF), due to the radiative decay of excited singlet states that are formed directly by excitation, according to Jablonski diagram reported in figure 2. This rapid decay, which usually occurs within a few nanoseconds, is followed by an emission tail due to the presence of DF. This occurs as a result of thermally activated reverse intersystem crossing from T_1 to S_1 and is usually identified as TADF. The fluorescence yield of TADF emitters (Φ_f) depends on the equilibrium between excited states of singlet and triplet due to the intersystem crossing (k_{ISC}) and reverse intersystem crossing (k_{rISC}), these are indeed key parameters in the observation of TADF. Strong DF is observed in molecules with a relatively strong yield of triplet formation, Φ_{ISC}, and where the yield of singlet states formed by reverse intersystem crossing is very high.[21]

1.2.5 TADF in bioimaging

Fluorescent compounds based on small organic molecules are powerful tools for visualizing biological events in living cells and organisms. Since the discovery of the first fluorescent organic compounds in the late 19th century, numerous efforts have been made to see the behaviors of specific biomolecules in living systems using these dyes

as labels. Following the development of fluorescent metal ion indicators, many fluorescent probes or biosensors, which are defined as molecules that exhibit a change in fluorescence properties in the presence of their target molecule, have been reported and applied in biological research. Today a variety of probes are available that target metal ions, pH, enzyme activities and so on. For example, Seung Kim and collaborators in 2009 synthesized a new coumarin (figure 7) having a remarkable ability to complex Cu (II).[22] Thanks to its solubility in water, the permeability of membranes and its non-toxicity, this coumarin has been tested as a probe for the detection of Cu (II) in living cells.
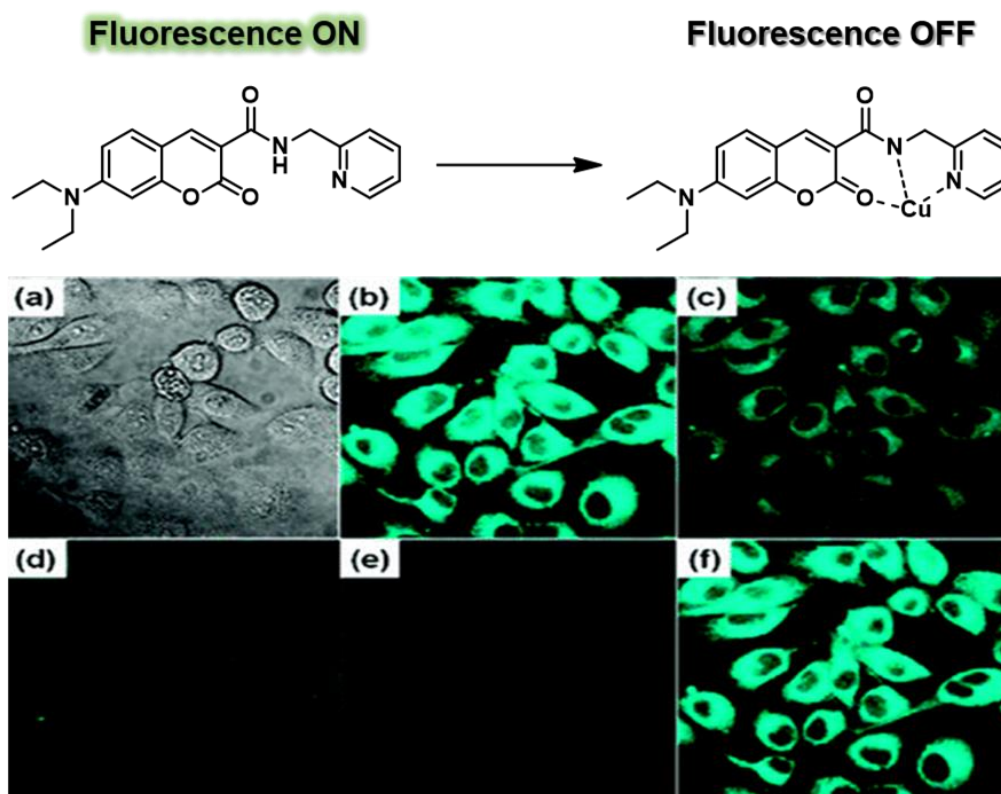
Figure 7. Confocal fluorescence images of Cu^{2+} in LLC-MK2 cells (Zeiss LSM 510 META confocal microscope, 40× objective lens). (a) Bright-field transmission image of LLC-MK2 cells. (b) Fluorescence image of LLC-MK2 cells incubated with coumarin (5 µM). Further incubated with addition of various concentrations of $CuCl_2$ [(c) 5, (d) 10, and (e) 20 equiv, respectively]. (f) Return of intracellular Cu^{2+} to the resting level was achieved by addition of EDTA (500 µM). This image was taken from the paper "Journal of the American Chemical Society" from the work of Seung Kim and collaborators.[22]

Another example in 2011 always Seung Kim and his collaborators synthesized another coumarin (figure 8) capable of effectively and selectively recognizes thiols based on a Michael-type reaction, showing a preference for cysteine over other biological materials including l homocysteine and glutathione.[23] This coumarin in the confocal microscopy study showed a marked improvement in fluorescence for cysteine compared to other thiol functionalized amino acids.
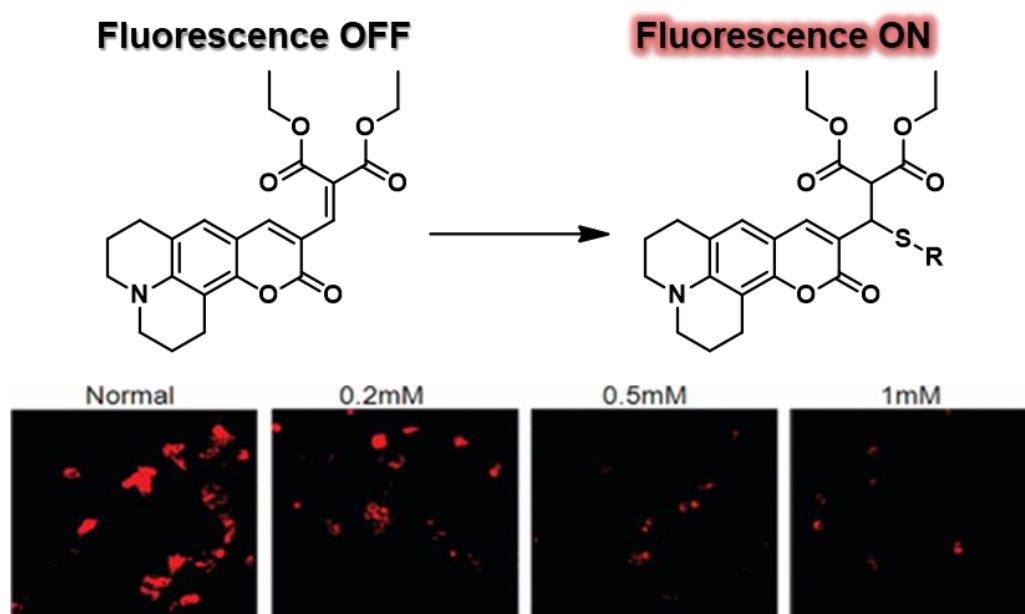
Figure 8. Confocal microscopic analysis of HepG2 cells treated with coumarin. The images of the cells were obtained using excitation at 488 nm and a long-path (>560 nm) emission filter. For the NEM-treated samples, before the media were finally replaced with PBS containing coumarin, the cells were incubated with media containing NEM at various concentrations for 1 h at 37 °C. This image was taken from the paper "Organic Letters" from the work of Seung Kim and collaborators.[23]

Since our bodies and cells generally do not give visual information sufficiently detectable with the naked eye, this does not allow us to understand specific biological events, such as cell signaling and protein expression. Therefore, the tools that allow us to observe cells are essential not only for basic biology research, but also for the diagnosis and treatment of diseases. Suitable methods must satisfy several conditions. First, the technique should be sensitive enough to visualize biological compounds at physiological

concentrations, which in most cases range from nanomolar to micromolar. Second, the method should have sufficient spatial and temporal resolution to analyze dynamic cell signaling processes. Third, the method should be non-invasive, meaning detection should be possible from the outside of the samples. Last, but not least, it should rely on tools that are not too special or expensive. Fluorescence imaging is an ideal methodology that meets all these requirements, compared to other technologies based on radioactivity, bioluminescence, electromagnetism and electrochemistry. This is why live fluorescence imaging is becoming widely used in cell biology. Another advantage of the technology that we should point out here is that a molecule's fluorescence signal can be drastically modulated by the molecular design. The fluorescein and rhodamine derivatives are particularly important, as they are currently among the most widely used organic molecules in fluorescent labels and probes used for bioimaging. Bright and photostable dyes with red to near infrared (NIR) fluorescence are particularly in demand for in vivo imaging in animals and humans due to the transparency of tissues in this wavelength region.
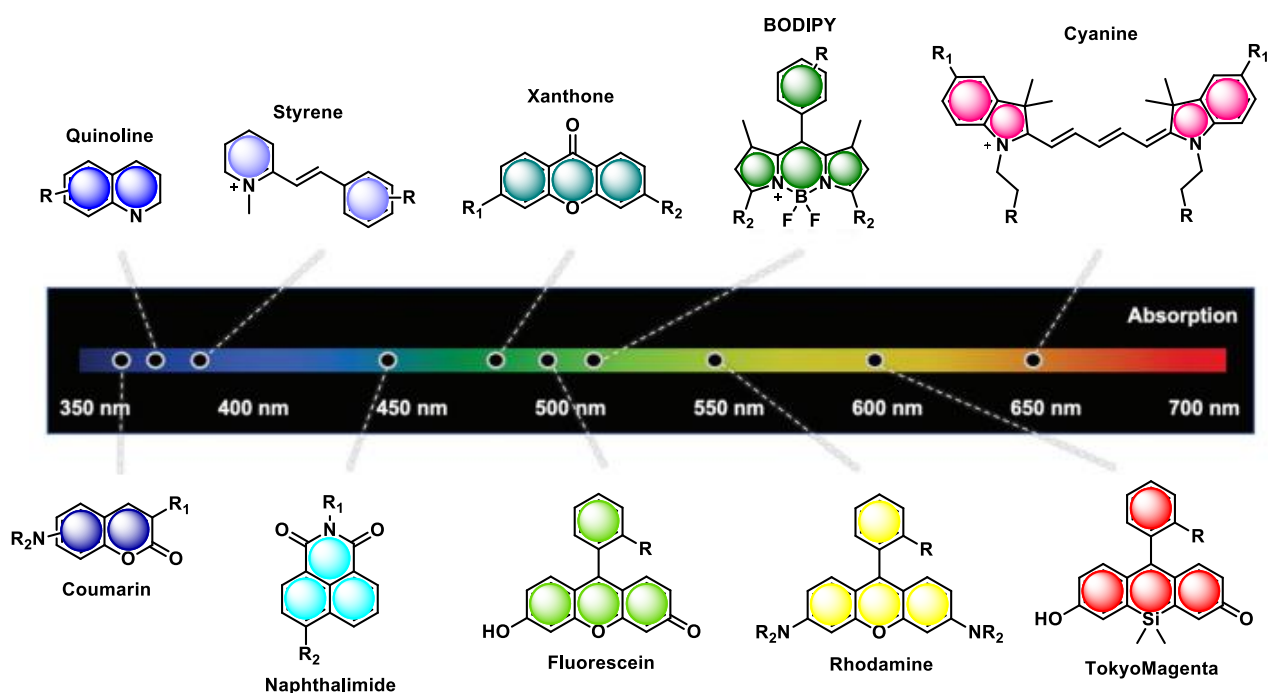
Figure 9. Core fluorescent scaffolds. Common scaffolds listed in order of increasing absorption values. R groups indicate sites for common functionalization.

Due to the difficulty of predicting a priori the photophysical properties of molecules under physiological conditions, most of the new fluorescent molecules have been discovered by chance or by screening multiple compounds. With the aim of accelerating rational and efficient development, numerous efforts have been made to date to explain and predict the optical properties of fluorescent molecules by quantum computation. It might eventually be possible to combine organic and computational chemistry to obtain new fluorescent scaffolds with properties superior to the classical ones. There are currently many fluorescent probes available, aimed at a variety of targets. Without doubt, they have made a significant contribution to our understanding of dynamic and complicated processes in biological systems.[24]

Thanks to the development of time-resolved fluorescence imaging (TRFI) techniques, biological information can be visualized better than ever by eliminating background signals of short duration. To implement TRFI techniques, fluorescence probes should have a relatively long fluorescence duration (generally, more than 10 nanoseconds) to distinguish their fluorescence from short-lived background signals using time-gated detection with a short delay time after excitation. To date, a variety of long-life fluorescent probes have been extensively explored for TRFI, such as transition metal complexes, lanthanoids, inorganic nanomaterials. However, the potential toxicity of these probes and the high costs of heavy metals limit practical applications. In recent years, organic TADF molecules have emerged as alternative candidates for TRFI due to their sufficiently long excited state lifetimes.[25]

To overcome the sensitivity of the T_1 state, many strategies have been proposed to obtain excellent organic TADF systems with long fluorescence durations and good biocom-

patibility for biomedical applications. For example, exploiting nanotechnology techniques, TADF nanoparticles (NPs) have been proposed water dispersible with optimal characteristics and are considered an effective material to protect sensitive T_1 states from molecular oxygen. TADF NPs are generally manufactured by encapsulating TADF molecules with amphiphilic molecules or polymers or by anchoring TADF molecules with silica nanoparticles. In this way, organic TADF materials can be applied in biology and biomedicine with all their desirable photophysical properties plus the additional benefits of excellent cell uptake and accumulation from easy chemical modifications to NPs surfaces. Alternatively, the integration of aggregation-induced emission (AIE) and TADF into a single molecule has been demonstrated as another potential strategy. The characteristics of aggregation-induced delayed fluorescence (AIDF) can effectively protect sensitive T_1 states from the surrounding environment, leading to efficient RISC and enrichment in the radiative transition. Furthermore, covalent modification of hydrophobic TADF molecules by introducing hydrophilic / target groups has been shown to be a possible way to address their drawbacks.[26]

For example Huang and collaborators in 2017 published the first work on the use of nanomaterials containing an organic emitter TADF for applications in TRFI (figure 10).[27]
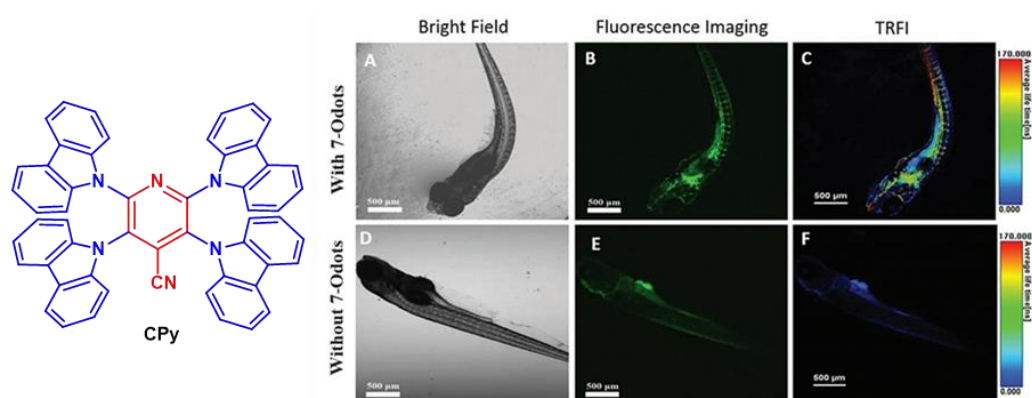
Figure 10. Confocal fluorescence images of zebrafish: A–) zebrafish injected with CPy-Odots; D–F) zebrafish noninjected with CPy-Odots; (A, D) were bright field images; (B,

E) were confocal fluorescence images recorded with 480–580 nm bandpass filters for CPy-Odots upon excitation at 405 nm; (C, F) were lifetime images. This image was taken from the paper "Advanced Science" from the work of Huang and collaborators.[27]

For all of these reasons further studies on TADF materials are needed to overcome these drawbacks and limitations. As an example; improve the optoelectronic performance of these chromophores, to achieve greater efficiency of TADF in the blue and red regions, to design and synthesize new TADF chromophores at the in order to obtain greater solubility in water, lower cytotoxicity and high selectivity for the analytes, so that these materials can be exploited in bioimaging and detection applications. This will require theoretical work, design and synthesis of new molecules and a broad photophysical characterization.

1.2.6 References

1. Uoyama, H., Goushi, K., Shizu, K., Nomura, H. & Adachi, C. Highly efficient organic light-emitting diodes from delayed fluorescence. *Nature* **492**, 234–238 (2012).

2. Li, X. *et al.* Small-molecule based thermally activated delayed fluorescence materials with dual-emission characteristics. *Sci. China Chem.* **64**, 534–546 (2021).

3. Nguyen, V.-N., Kumar, A., Lee, M. H. & Yoon, J. Recent advances in biomedical applications of organic fluorescence materials with reduced singlet–triplet energy gaps. *Coordination Chemistry Reviews* **425**, 213545 (2020).

4. Wong, M. Y. & Zysman-Colman, E. Purely Organic Thermally Activated Delayed Fluorescence Materials for Organic Light-Emitting Diodes. *Adv. Mater.* **29**, 1605444 (2017).

5. Yang, Z. *et al.* Recent advances in organic thermally activated delayed fluorescence materials. *Chem. Soc. Rev.* **46**, 915–1016 (2017).

6. Barman, D., Gogoi, R., Narang, K. & Iyer, P. K. Recent Developments on Multi-Functional Metal-Free Mechanochromic Luminescence and Thermally Activated Delayed Fluorescence Organic Materials. *Front. Chem.* **8**, 483 (2020).

7. Bizzarri, C., Hundemer, F., Busch, J. & Bräse, S. Triplet emitters versus TADF emitters in OLEDs: A comparative study. *Polyhedron* **140**, 51–66 (2018).

8. Parker, C. A. & Hatchard, C. G. Triplet-singlet emission in fluid solutions. Phosphorescence of eosin. *Trans. Faraday Soc.* **57**, 1894 (1961).

9. Kirchhoff, J. R. *et al.* Temperature dependence of luminescence from $Cu(NN)^{2+}$ systems in fluid solution. Evidence for the participation of two excited states. *Inorg. Chem.* **22**, 2380–2384 (1983).

10. Berberan-Santos, M. N. & Garcia, J. M. M. Unusually Strong Delayed Fluorescence of C_{70}. *J. Am. Chem. Soc.* **118**, 9391–9394 (1996).

11. Endo, A. *et al.* Thermally Activated Delayed Fluorescence from Sn^{4+}-Porphyrin Complexes and Their Application to Organic Light Emitting Diodes - A Novel Mechanism

for Electroluminescence. *Adv. Mater.* **21**, 4802–4806 (2009).

12. Deaton, J. C. *et al.* E-Type Delayed Fluorescence of a Phosphine-Supported Cu_2 (μ-$NAr_2)_2$ Diamond Core: Harvesting Singlet and Triplet Excitons in OLEDs. *J. Am. Chem. Soc.* **132**, 9499–9508 (2010).

13. Endo, A. *et al.* Efficient up-conversion of triplet excitons into a singlet-state and its application for organic light emitting diodes. *Appl. Phys. Lett.* **98**, 083302 (2011).

14. Endo, A. *et al.* Efficient up-conversion of triplet excitons into a singlet-state and its application for organic light emitting diodes. *Appl. Phys. Lett.* **98**, 083302 (2011).

15. Adachi, C. Third-generation organic electroluminescence materials. *Jpn. J. Appl. Phys.* **53**, 060101 (2014).

16. Zhang, M., Zheng, C.-J., Lin, H. & Tao, S.-L. Thermally activated delayed fluorescence exciplex emitters for high-performance organic light-emitting diodes. *Mater. Horiz.* **8**, 401–425 (2021).

17. Zhang, N. et al. Improving the efficiency of exciplex based OLEDs by controlling the different configurations of the donor. *J. Mater. Chem. C* **9**, 600–608 (2021).

18. Tsuchiya, Y. *et al.* Molecular Design Based on Donor-Weak Donor Scaffold for Blue Thermally-Activated Delayed Fluorescence Designed by Combinatorial DFT Calculations. *Front. Chem.* **8**, 403 (2020).

19. Park, I. S., Komiyama, H. & Yasuda, T. Pyrimidine-based twisted donor–acceptor delayed fluorescence molecules: a new universal platform for highly efficient blue electroluminescence. *Chem. Sci.* **8**, 953–960 (2017).

20. Liu, Y., Li, C., Ren, Z., Yan, S. & Bryce, M. R. All-organic thermally activated delayed fluorescence materials for organic light-emitting diodes. *Nat Rev Mater* **3**, 18020 (2018).

21. Dias, F. B., Penfold, T. J. & Monkman, A. P. Photophysics of thermally activated delayed fluorescence molecules. *Methods Appl. Fluoresc.* **5**, 012001 (2017).

22. Jung, H. S. et al. Coumarin-Derived Cu^{2+} -Selective Fluorescence Sensor: Synthesis, Mechanisms, and Applications in Living Cells. *J. Am. Chem. Soc.* **131**, 2008–2012 (2009).

23. Jung, H. S. et al. Coumarin-Based Thiol Chemosensor: Synthesis, Turn-On Mechanism, and Its Biological Application. *Org. Lett.* **13**, 1498–1501 (2011).

24. Zhao, W., Wei, H., Liu, F. & Ran, C. Glucose ligand modififed thermally activated delayed fluorescence targeted nanoprobe for malignant cells imaging diagnosis. *Photodiagnosis and Photodynamic Therapy* **30**, 101744 (2020).

25. Terai, T. & Nagano, T. Small-molecule fluorophores and fluorescent probes for bioimaging. *Pflugers Arch - Eur J Physiol* **465**, 347–359 (2013).

26. Nguyen, V.-N., Kumar, A., Lee, M. H. & Yoon, J. Recent advances in biomedical applications of organic fluorescence materials with reduced singlet–triplet energy gaps. *Coordination Chemistry Reviews* **425**, 213545 (2020).

27. Li, T. et al. Thermally Activated Delayed Fluorescence Organic Dots (TADF Odots) for Time-Resolved and Confocal Fluorescence Imaging in Living Cells and In Vivo. *Adv. Sci.* **4**, 1600166 (2017).

Chapter 2: Synthesis and photophysical properties of fluorescent D-π-A coumarin derivatives

2.1 introduction

Coumarins (2H-chromen-2-ones) are a class of naturally occurring compounds, that have been widely investigated for their electronic, photonic and pharmaceutical applications, and are suitable materials for optoelectronic devices due to their excellent photostability.[28-30]

Coumarin derivatives represent an important class of heterocyclic compounds that possess many significant optoelectronic properties as well as exhibiting diverse biological activities. These molecular scaffolds are generally characterized by high photoluminescence quantum yield (PLQY), large Stokes shifts, sensitivity, and intramolecular charge transfer (ICT) properties. For all these reasons, coumarin derivatives find application in various research fields such as laser dyes and the manufacture of organic light-emitting diodes (OLED) and dye-sensitized solar cell (DSSC), as cell imaging biomarkers and optical brighteners.[31-36]

The visible absorption properties of these compounds are highly controlled by the insertion of various substituents directly linked to the heteroaromatic structure and in particular, the coumarin functionalization by inserting electron donating group (EDG) groups in the positions C6 or C7 and electron withdrawing group (EWG) in position C3 or C4.[37] By the analysis of different coumarin derivatives used in dye laser applications, Zeidler and collaborators[38] observed that the benzene rings of these compounds exhibited a predominant para-quinoidal resonance state, determined by a "push-pull" effect leading to intramolecular charge transfer ICT resulting in shortening of the C5-C6 and C8-C9 bonds. The increase of the "push-pull" effect reduces the coumarin band-

gaps which lead to the shift of the spectral red in the UV-vis absorption. Furthermore, π-expanded coumarin derivatives, such as benzocoumarins or vertically-expanded derivatives, revealed redshift absorption and emission and better quantum fluorescence yields than simple bicyclic compounds. These results and ongoing investigations in this field indicate how the rational synthesis of fluorescent Donor-π-Acceptor (D-π-A) molecules is still of fundamental importance for their centrality in material sciences.[39-40]

In this chapter we report a rational study concerning the synthesis and the photophysical characterization of new coumarin structures containing various aromatic spacers between the heteroaromatic coumarin scaffold and the electron donor group (EDG), aimed at increasing the conjugation of the push-pull system and selecting new candidate molecules for the construction of non-toxic biomarker dyes with efficient emissions in the blue-green spectral region.

2.2 Bioimaging

As anticipated into chapter 1 when organic molecules are used for bioimaging applications, several factors need to be considered. Chemical stability is essential and the fluorophore must have an appropriate photophysical profile for the application of interest. A high PLQY is desirable, but it is not considered a key requirement. Low quantum yields can be tolerated if the molar extinction coefficient (ϵ) is very high, as the luminosity will remain high. In terms of wavelengths, those with lower energy are favored, generally greater than 500 nm, which are less harmful in biological environments. The use of longer excitation wavelengths also reduces the background emission, which is called autofluorescence, caused by intrinsic fluorophores present in proteins, cells, tissues, and so on. Other important photophysical characteristics to consider are the

Stokes shift and the photostability of the compounds. In general, the use of fluorescent dyes with small Stokes displacements should be avoided because they can generate artifacts during analysis caused by the scattering effects of excitation light. Finally, water solubility should be sought as bioimaging is performed almost exclusively in aqueous environments. Unfortunately, many small organic compounds with interesting photophysical and biological properties are hydrophobic and are usually not even soluble in water. In these cases, before the experimental use, these compounds can be dissolved in a solvent vehicle miscible with water, generally dimethylsulfoxide is used, the dissolved dye is subsequently diluted with the aqueous-based medium used in the application.[41-44] Some coumarin structures used for bioimaging applications are reported below (figure 11).[45-51]
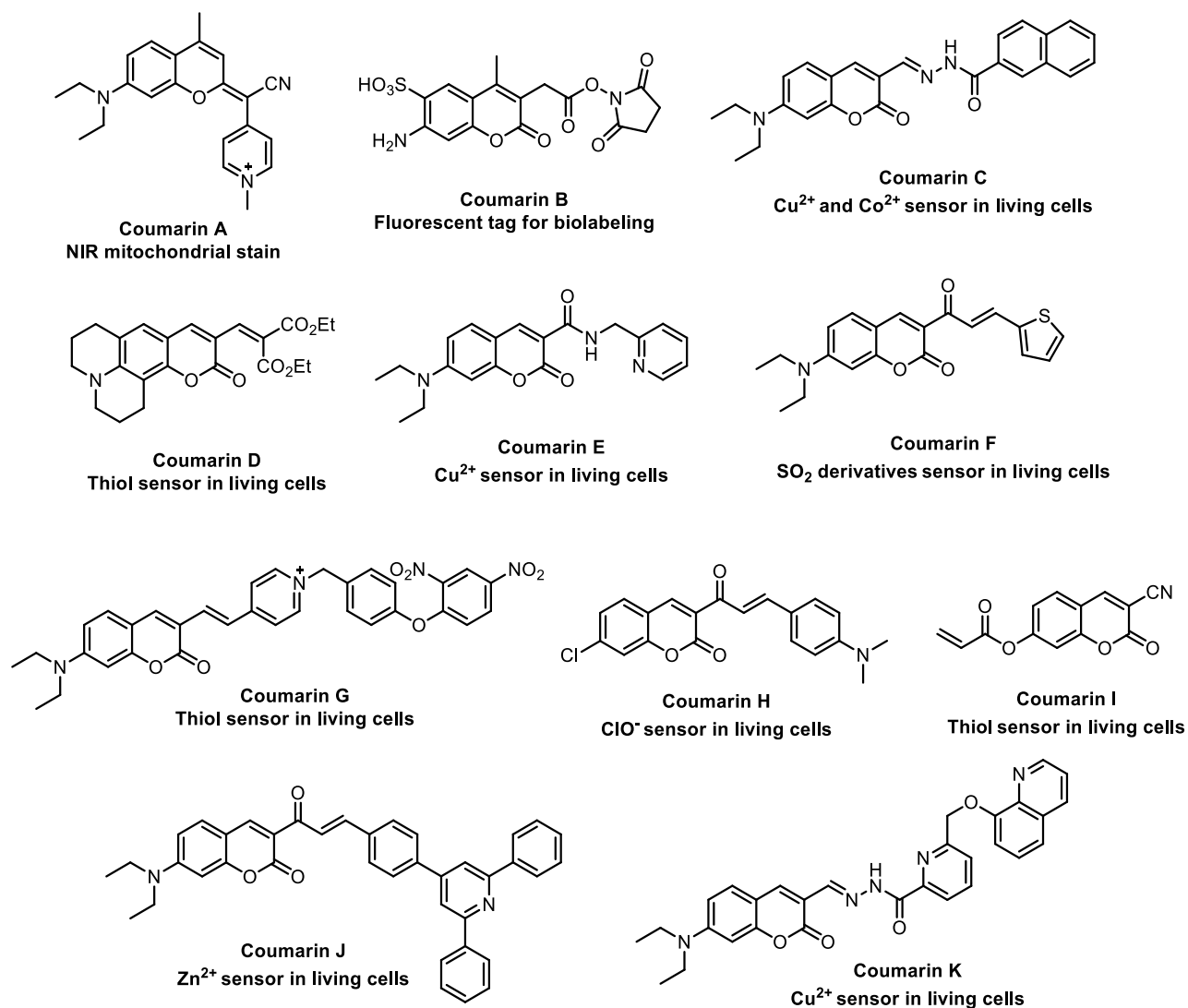
Figure 11. Some examples of coumarins used in bioimaging.

2.3 Coumarin push-pull systems

Coumarin mother structure and its derivatives without an electron donor group (EDG) have negligible emission (Figure 12).
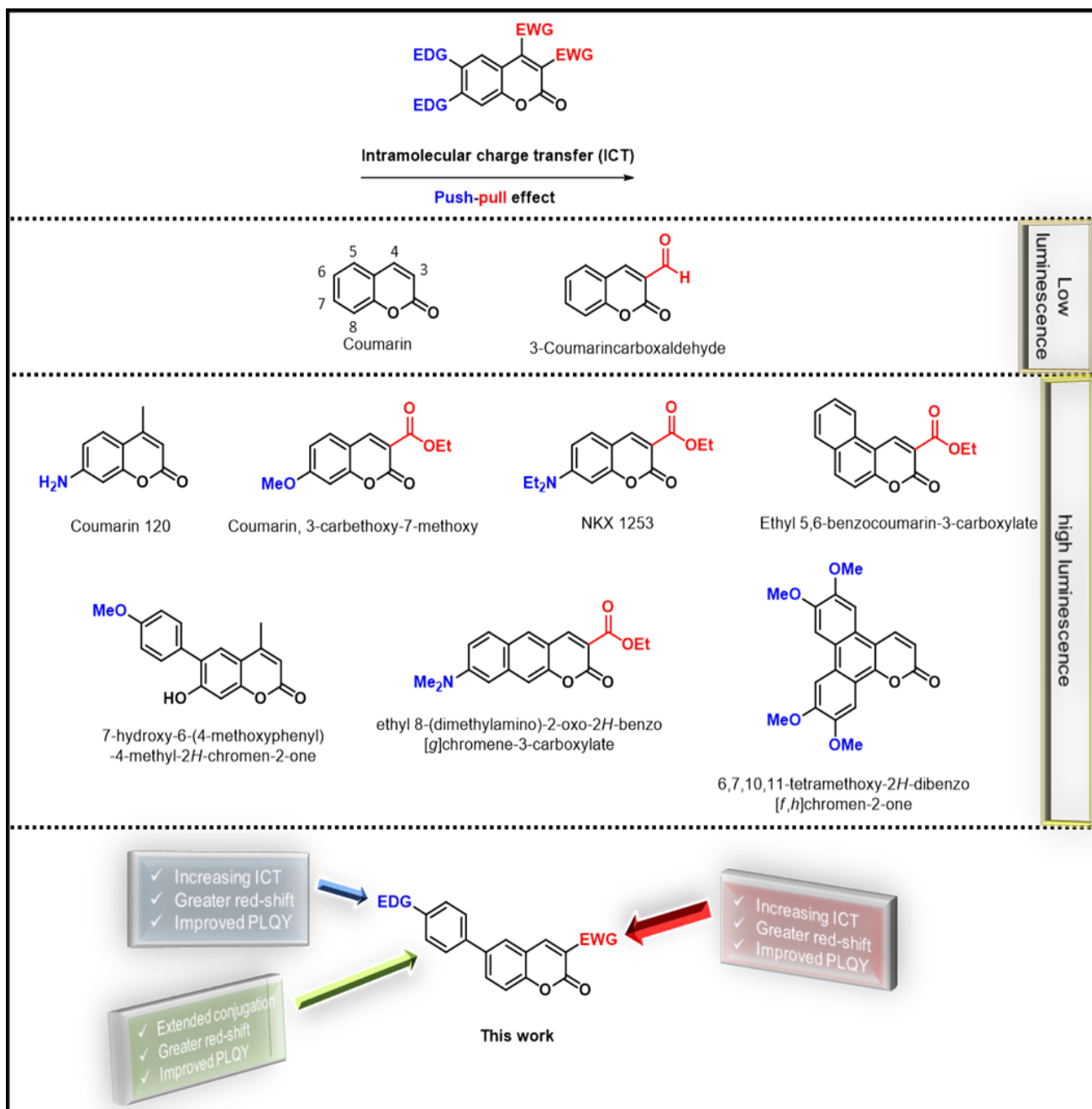
Figure 12. Examples of luminescent coumarin structures.

Position 6 and 7 is often replaced with an EDG, typically with an ether or amine, to induce fluorescence. This creates an electronic "push-pull" effect in which the carbonyl group of the lactone ring acts as the electron-withdrawing acceptor unit. Methoxy-substituted coumarins tend to exhibit higher quantum yields in highly polar solvents such as methanol or water. In contrast, amino-substituted derivatives tend to be quenched in

protic solvents while exhibiting higher quantum yields in ethyl acetate. The presence of an electron-withdrawing group (EWG) in position 3 further strengthens the intramolecular charge transfer (ICT), which results in a significant redshift and greater solvatochromic behavior. The rigid planar core increases the efficiency of the push-pull effect and typically leads to good quantum yields. However, the absence of extended conjugation generally results in poor molar extinction coefficients and therefore in limited brightness. Extended π coumarins are therefore generally more suitable for bioimaging. 5- and 8-substituted coumarins are less common but exist as subfamilies of fused ring derivatives such as pyran or furanocoumarins. Although their blue-shifted excitation profiles sometimes limit their application in biological environments, coumarin-based imaging agents are quite popular due to easy access, high photostability and, in many cases, excellent quality fluorescent.[52]

2.4 Results and discussion

In this work a series of 6- and 6,8-diaryl coumarins were synthesized starting from 5-bromosalicylaldehyde through a simple two-step procedure consisting of a Knovenagel condensation[53-54] of a series of malonate derivatives and followed by a Suzuki cross-coupling reaction catalyzed by $Pd(PPh_3)_4$ with selected boronic acids. This strategy allowed to obtain the corresponding adducts in a multigram scale with good to excellent yields. Following the same strategy, 6,8-diaryl-coumarins were prepared starting from dibromosalicylaldehyde as summarized in schemes 1 and 2.
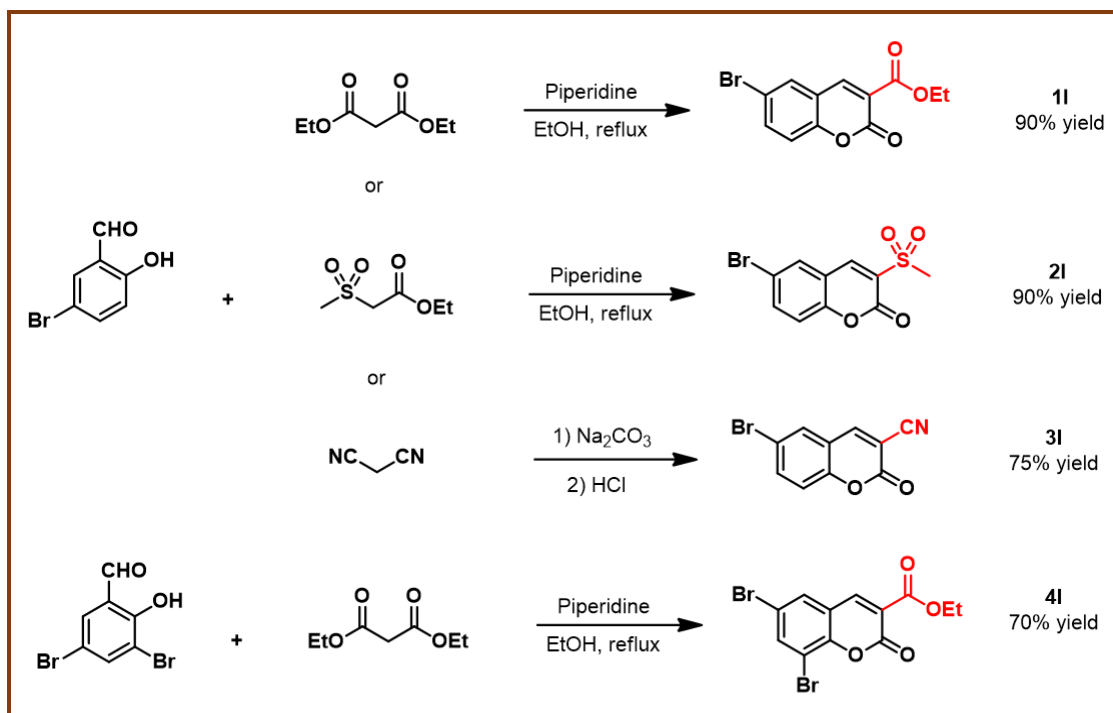
Scheme 1. Synthesis of bromocoumarin derivatives through a pirrolidine/AcOH catalyzed Knoevenagel condensation
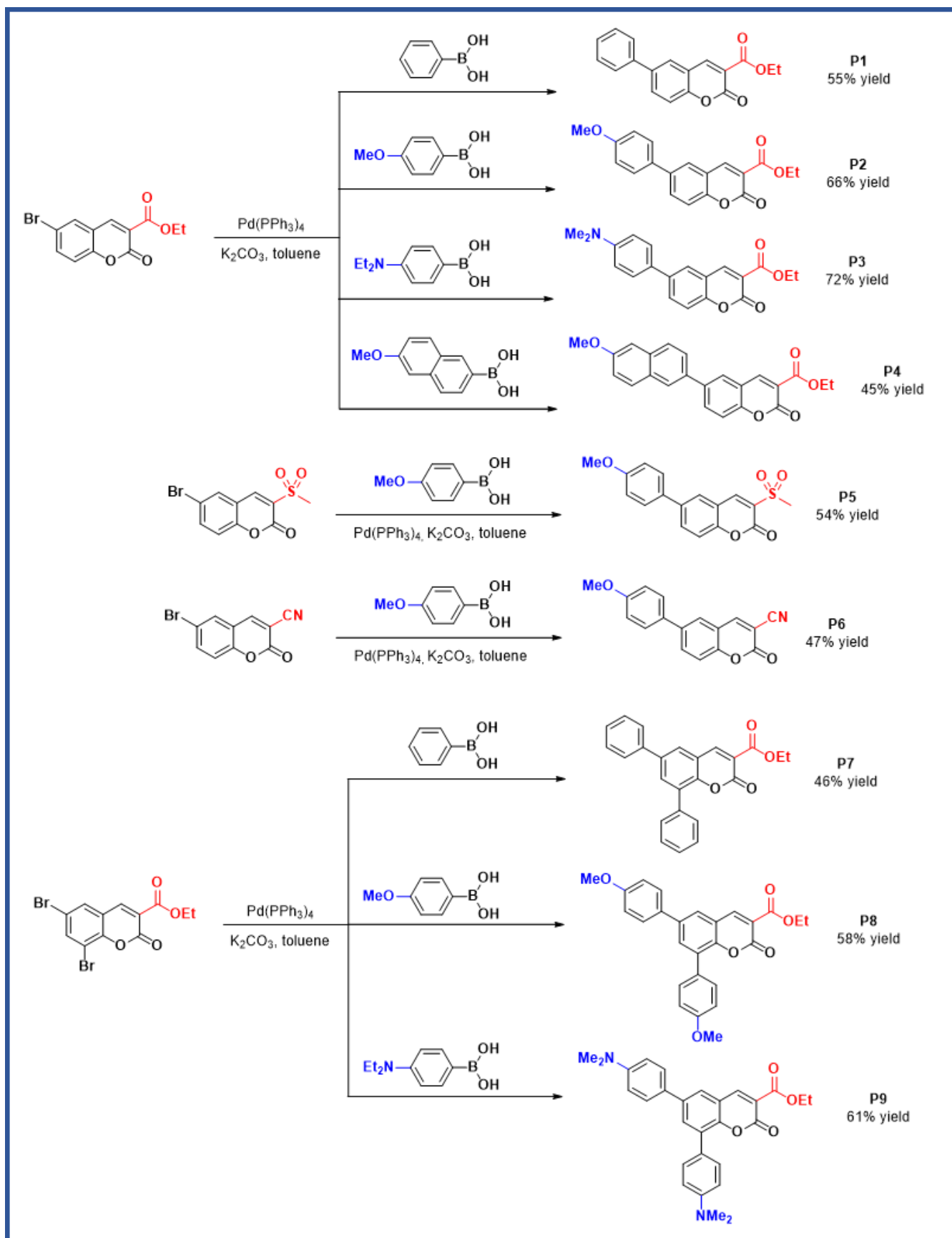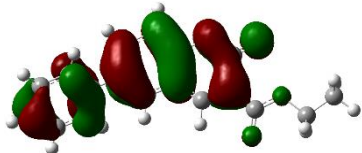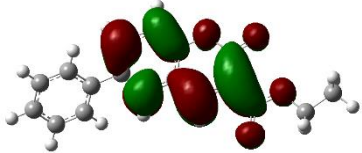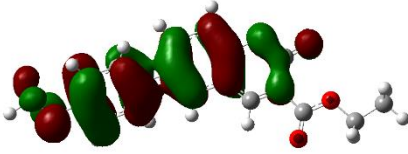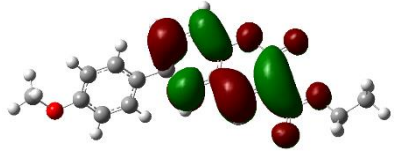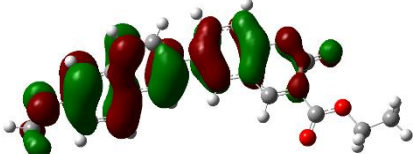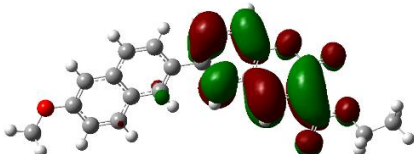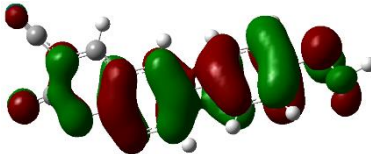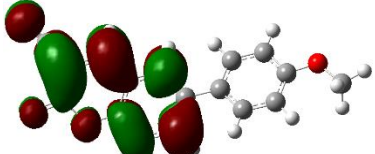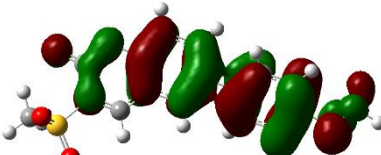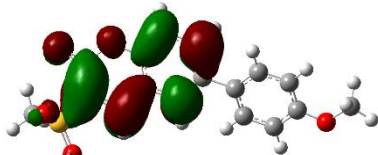
Scheme 2. Synthesis of arylcoumarin derivatives through Pd(0)-catalyzed Suzuki cross-coupling

2.4.1 Theoretical Calculations

Quantum chemical calculations were performed in order to predict and rationalize the electronic properties of compounds **P1-P9**. The Density Functional Theory (DFT) calculations, including geometry optimization of the emitters, were performed by the Gaussian 09 Revision D.01 software in the gas phase using DFT level using B3LYP functional and a 6-31G(d,p) basis set. The ground state molecular geometries of coumarins were optimized starting from their molecular structures as drawn in GaussView 5.0. The simulations were accomplished in the vacuum and with a model solvent, chloroform (CLF). In the latter case solvation effects arising from the interaction of coumarin derivatives with CLF were treated with the Self Consistent Reaction Field (SCRF) model by simulating the dielectric solvent through the Polarizable Continuum Model (PCM) calculation with-in the integral equation formalism (IEFPCM).

From this first investigation, we observed that these derivatives do not assume a planar geometry as expected, since the electron withdrawing groups tend to rotate with respect to the coumarin plane. The analysis of atomic distances and angles indicated that in the excited state all the coumarin derivatives studied have a more planar structure than in the ground state, as a consequence of the redistribution of the electric charge.

Table 1. Calculated geometry, absorption and emission characteristics (in vacuum and in Chloroform solvent in brackets) and the HOMO and LUMO molecular orbitals (H = white atom, O = red atom, C = gray atom, S = atom atom yellow; the isocontour value is 0.02 au).

Sample id	λ_{abs} (nm)	λ_{em} (nm)	HOMO	LUMO
P1	362 (372)	444 (457)		
P2	401 (419)	494 (526)		
P4	435 (453)	539 (573)		
P6	420 (442)	512 (549)		
P5	400 (420)	498 (537)		
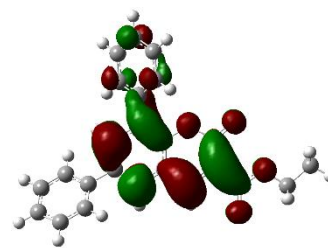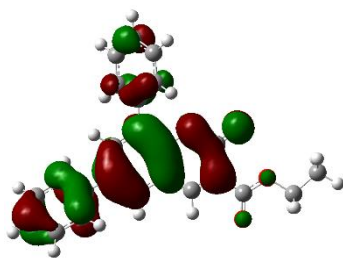
P7	380 (386)	482 (481)	
P8	423 (432)	540 (544)	
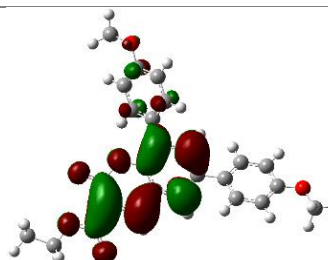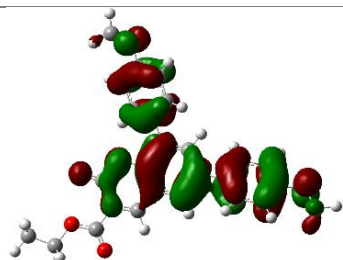
As regards the product **P1**, the dihedral angle between the coumarin plane and the retreating group changes of about 11% in the excited state with respect to the ground state, while the electric charge changes mainly on the carbon atoms of the coumarin rings, with the greater decrease of negative charge recorded in the position 3, the one that acts as a bridge to the acceptor group. Similar results have been achieved for the other synthesized products, with a variation of the dihedral angle in the range 5-11%, the lowest variation is recorded for **P4**. In the case of double substitution with two electron donor groups in position 6 and 8, both groups undergo a similar variation in the excited state compared to the fundamental one, leading to a more planar structure. These data are confirmed by molecular orbitals (MOs) calculations for both the HOMO and LUMO energies. Upon excitation, the molecule undergoes a structural and electrical reorganization that leads to an electron density pinned on the coumarin plane and partially to the acceptor group, without any contribution from the donor group. A complete charge transfer to the acceptor group is observed only for the compound **P3**. Further TD-DFT calculations allowed to estimate absorption and emission

characteristics, which have been summarized in Table 1. The simulated optical properties indicate that the substitution with EDG with increasing donating character, from phenyl group (**P1**) to paramethoxy-phenyl (**P2**) and 6-methoxy-naphthyl (**P4**) groups, leads to an increase in the wavelength of the estimated optical absorption and, consequently, of the emissions of about 75 nm, shifting the HOMO-LUMO transition from the near UV (362 nm for **P1**) to the blue range (435 nm for **P4**) and the from blue (444 nm for **P1**) to the green range (532 nm for **P4**). The variation of the acceptor group, from ethyl ester (**P2**) to cyano (**P6**) or methylsulfoxide (**P5**) groups, shown that in the **P1** case a red shift of the optical characteristics of about 20 nm is obtained while there are no significant differences for compounds **P2** and **P6**. Moreover, regarding the substitution with two electron donating groups such as **P7** and **P8**, the absorption is red shifted by about 20 nm while the emission of about 40 nm with respect to the corresponding monosubstituted derivative for both compound **P7** and **P8**. Finally, as previously mentioned, for all simulated coumarins, the presence of a solvent causes an almost rigid red shift for the calculated optical properties.

2.4.2 Photophysical properties

The figure 13 shows the absorption and emission spectra of the synthesized coumarins **P1**-**P8**. As illustrated, spectra show two main excitations, the first in the far UV around 300 nm, and the second in the 300-400 nm spectra region. Moreover, the greatest redshift was observed in the near UV-Vis range for sample **P6**, in agreement with the simulated results.
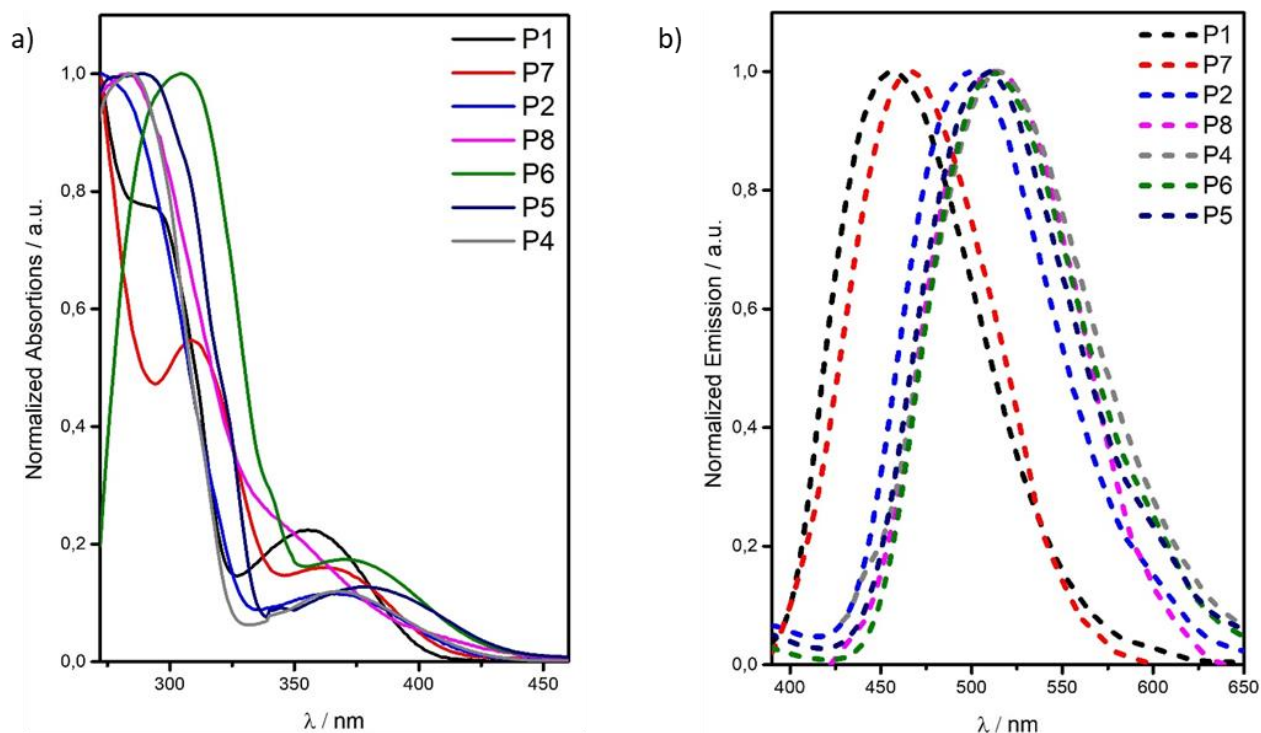
Figure 13. Absorption (a) and emission (b) spectra of the investigated coumarins **P1-P8** at 10-5M in chloroform, λ_{exc} = 350nm.

The experimental spectra are in good agreement with the calculated values, showing a red shift of the near UV-Vis absorption peak by changing the substituent from phenyl group (**P1**) to paramethoxy-phenyl (**P2**) and 6-methoxy-naphthyl (**P4**). The predicted absorption and emission variation were also confirmed, by experimental data achieved for the derivatives **P2** and **P5**, also scoring a redshift of about 20 nm for the molecule **P6**. In contrast, the calculations indicated that di-aryl substituted adducts do not caused significant changes in the absorption spectra. This discrepancy could be related to the poorly estimated interaction between the two substituents with the pseudopotential B3LYP. As for the effect of the substitution on the emission properties, the recorded spectra show that a large shift of about 70 nm is observed between the bluer molecule (**P1**) and the greenest one (**P4**). Compared to the calculated data, we noticed that the emission peaks of the compounds **P2**, **P4**, **P5** and **P6** were almost superimposable. As shown in figure 13, the disubstituted coumarins **P7** and **P8**, show an emission redshift

of about 15 and 20 nm with respect to the corresponding monosubstituted derivatives **P1** and **P2** which show about half of the shift expected by the computational calculation. The experimental analysis also show that an appropriate functionalization of the benzenoid ring with EDG having an increasing donor character causes an efficient red shifting of about 60 nm.

Furthermore, solvatochromic studies conducted in *n*-hexane, toluene, diethyl ether and chloroform, showed large emission shifts of about 60 nm for the coumarins **P2**, **P4**, **P5** and **P6** while for coumarin **P1** showed a red-shift of only 15 nm (figure 14). This can be explained by the fact that coumarin **P1** has a less marked charge transfer states (CT) character than the other coumarins analyzed. In fact, the solvatochromism observed for these coumarins is caused by the formation of CT states, where the ground state has a very different geometry compared to that of the excited state. This large geometry change strongly depends on the polarity of the solvent in which the emitter is dispersed. In fact CT emitters have higher dipole moments in the excited state than in the ground state. After excitation, the solvent dipoles interact strongly with the dipole moment of the excited molecule and the dipoles rearrange to minimize the energies, resulting in a more strongly relaxed excited state. For more polar solvents, the relaxation effect of the solvent is increased and thus the emission shifts to lower energies. Emissions from the CT states are also devoid of features, and this may be associated with the fact that there is a distribution of several solvated complexes and all of these different spectral contributions resulted in an almost Gaussian form overlap. All coumarins λ_{Emax} values are listed in Table 2.
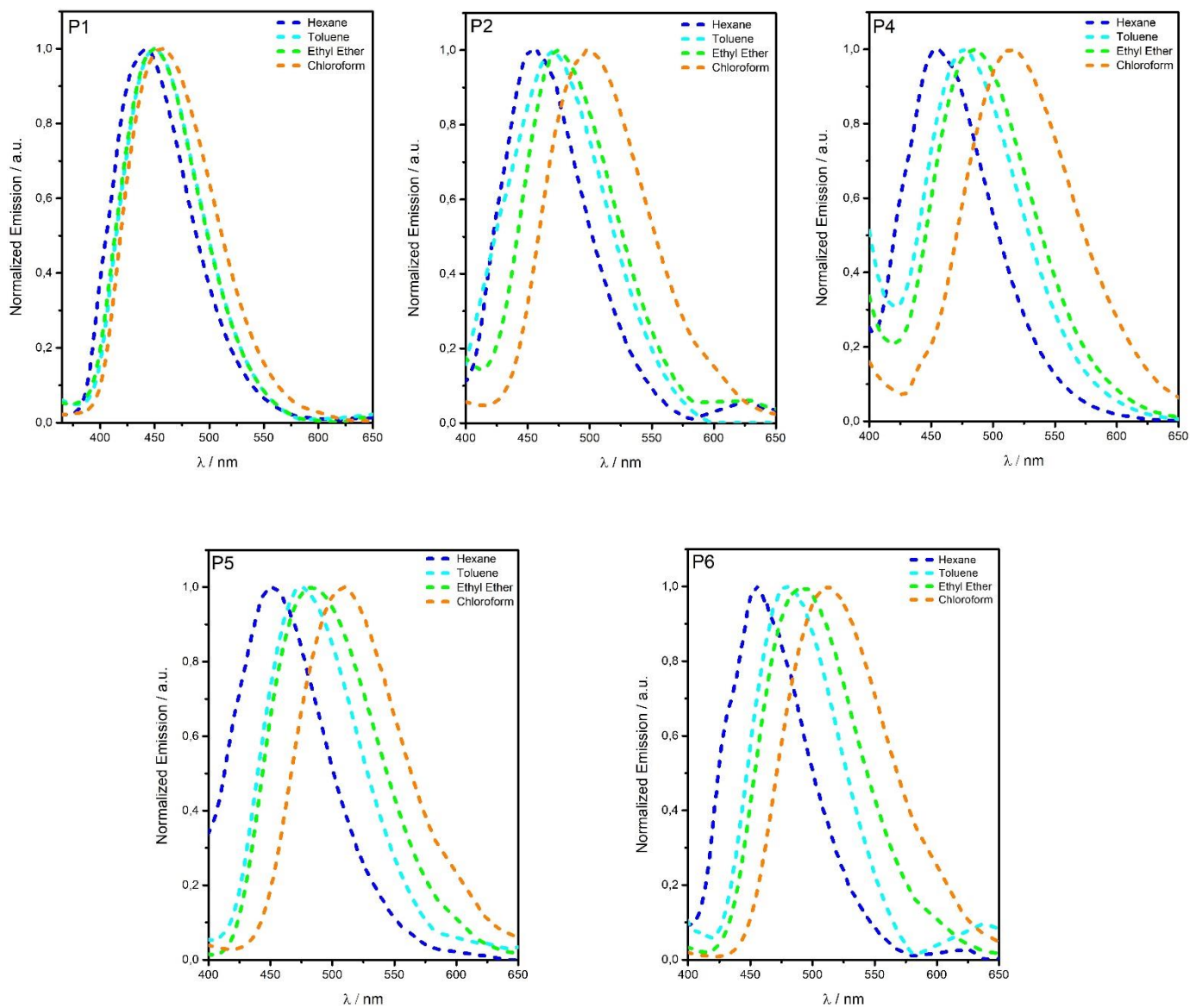
Figure 14. Emission spectra of **P1**, **P2**, **P4**, **P5** and **P6** samples in different solvents, under excitation at 300 nm.

Table 2. λem = maximum emission wavelength

Coumarin	λ PL (nm) Hexane	λ PL (nm) Toluele	λ PL (nm) Diethyl ether	λ PL (nm) Chlorofom
P1	441	449	450	457
P2	454	470	475	498
P4	455	477	485	515
P5	452	476	484	510
P6	454	480	493	512

The decay time of the coumarins in solution was recorded under excitation at 350 nm showing that all tested derivatives shown a single exponential decay with life time ranging from sub-nanosecond for **P1** and **P7** to 9 and 13 ns for **P5** compounds and **P6** respectively (Figure 15). We also noted that variation in acceptor groups causes an increase over the course of life, while almost no variation was observed for disubstituted versus monosubstituted coumarins.
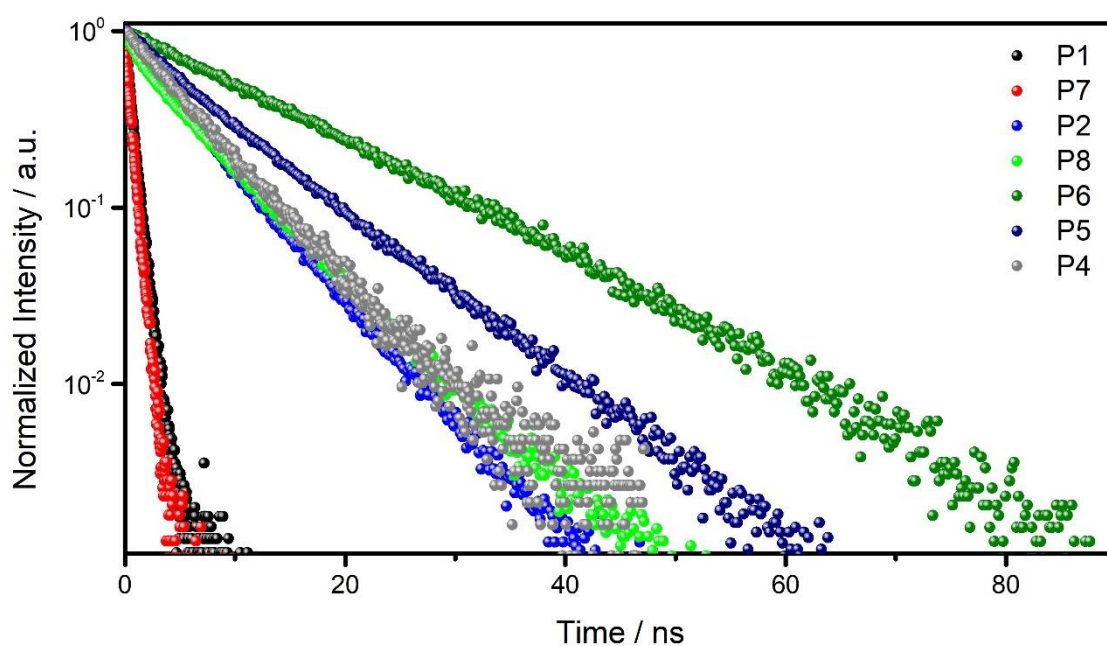
Figure 15. Decay time plot of coumarins **P1-P8** in chloroform, excited at 350 nm

Furthermore, in table 3 we summarized the spectral characteristics of the coumarins analyzed in chloroform solutions. From these analyzed we notice that compound **P5** and **P6** exhibiter large Stokes shift leading to green emissions, and also have the largest PLQY of the series.

Table 3. Photophysical properties of the coumarins **P1-P8** in chloroform solution. *Φ calculated using rhodamine 6G as a reference.[55]

Coumarin	λ Abs (nm)	λ PL (nm)	Φ*	τ(ns)
P1	258, 295, 357	456	0.05	0.7
P7	252, 309, 365	465	0.03	0.6
P2	274, 370	500	0.15	6.0
P8	280	520	0.12	5.7
P6	283, 380	512	0.45	9.3
P5	288, 368	510	0.69	13.0
P4	303, 372	515	0.13	6.0

Fluorescence emission experiments were also performed with coumarins **P2**, **P5** and **P6**, at a concentration of 10 µM in chloroform, to highlight any acidochromism effects (Figure 15). These investigations were performant by using TFA. However, by increasing the acid concentration, a general decrease in the fluorescence maximum and sensitive red-shifts from 512 to 536 nm **P6**, 510 to 533 nm for **P5**, and 496 to 508 for **P2** were achieved. This emission red shift should be mainly due to the protonation of the nitrile EWG group for compound **P6** and the ester function for the adducted **P2** and **P5**.
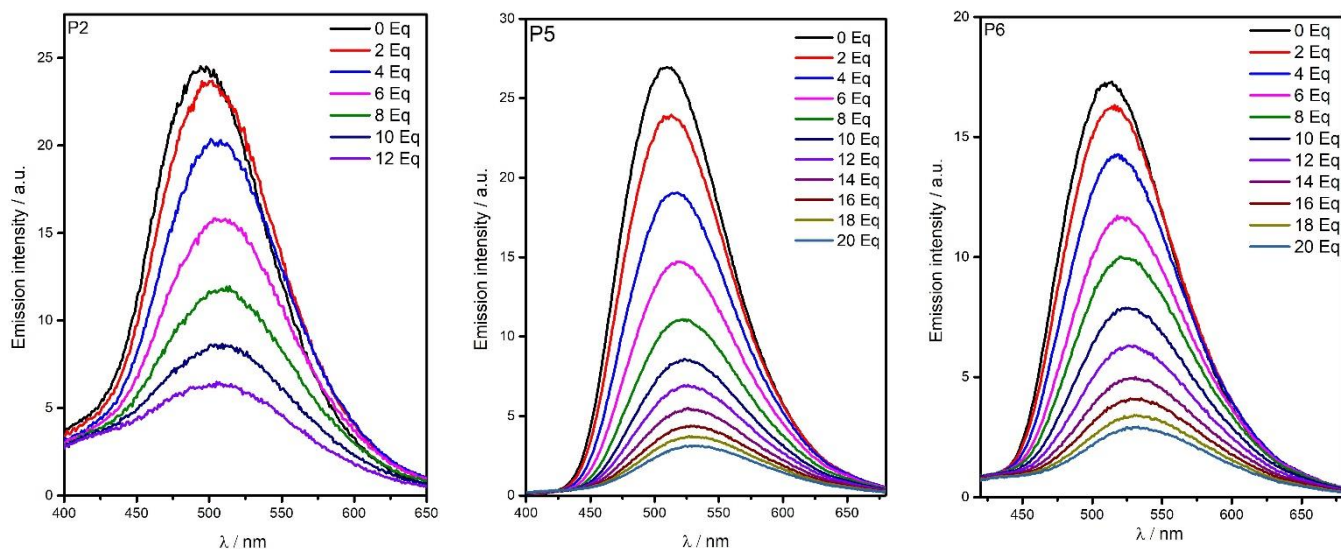
Figure 15. Changes in the emission spectra of compound **P2**, **P5** and **P6** (10 μM) with the incremental addition of TFA in Chloroform (λexc = 350 nm)

Subsequently, compounds **P4** and **P5** were subjected to a series of other titrations with C- or N-protected amino acids. Furthermore, **P5** and **P6** were tested with a panel of selected metal salts (Co^{2+}, Sn^{2+}, Ca^{2+}, Cu^{2+}, Al^{3+}, Gd^{3+}, Fe^{3+}) by fluorescence spectroscopy. It aims to highlight any interaction with organic or inorganic entities that would indicate potential sensor properties. However, the experiments conducted with the amino acid were ineffective, as reported in the figures 16-21.

While coumarins **P5** and **P6** showed a noticeable change in their emission spectra when Al^{3+}, Fe^{3+} and Cu^{2+} were added to their solutions (Figure 22). Especially in the case of Fe^{3+}, the emission spectra of **P5** and **P6** showed an appreciable decrease in fluorescence intensity, even if this only happens at high Fe^{3+} concentrations (Figures 23-24). On the other hand, the addition of Al^{3+} to **P5** and **P6** caused an increase in fluorescence and a blue shift as reported in Figure 22.
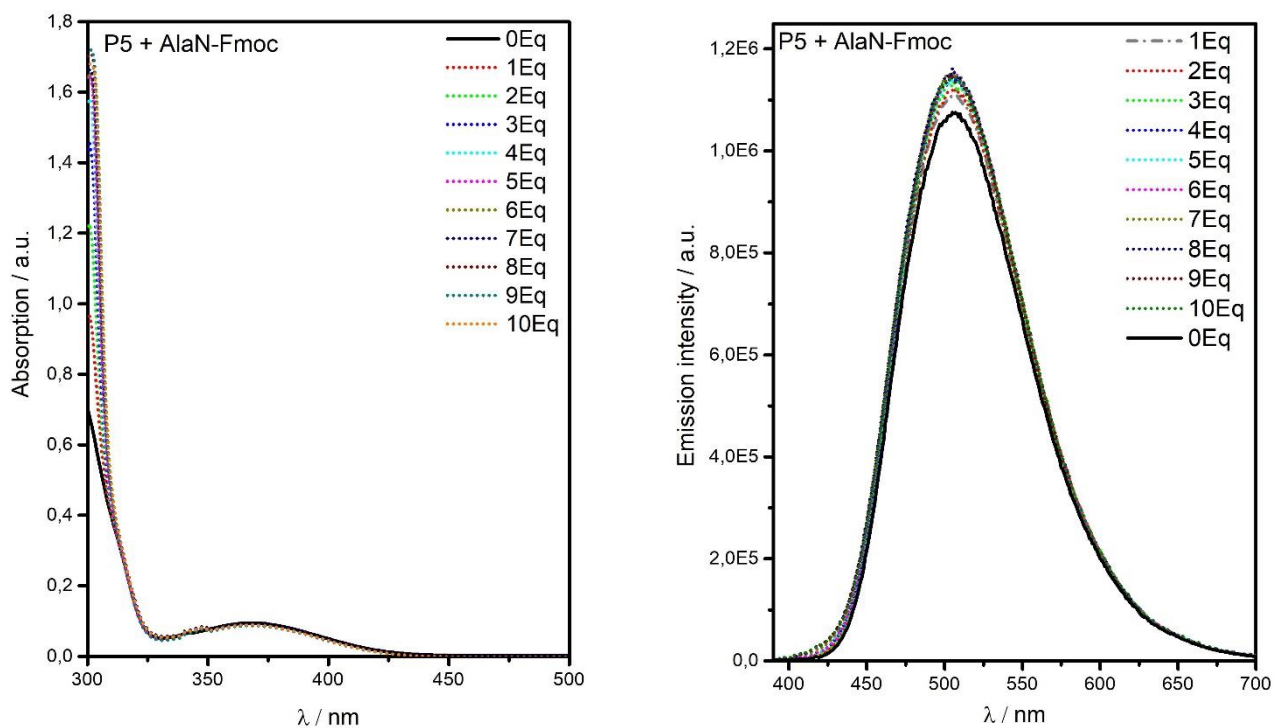
Figure 16. Changes in the absorption and PL of **P5** (10 µM) with the incremental addition of *N*-Fmoc-alanine in Chloroform (λex = 350 nm).
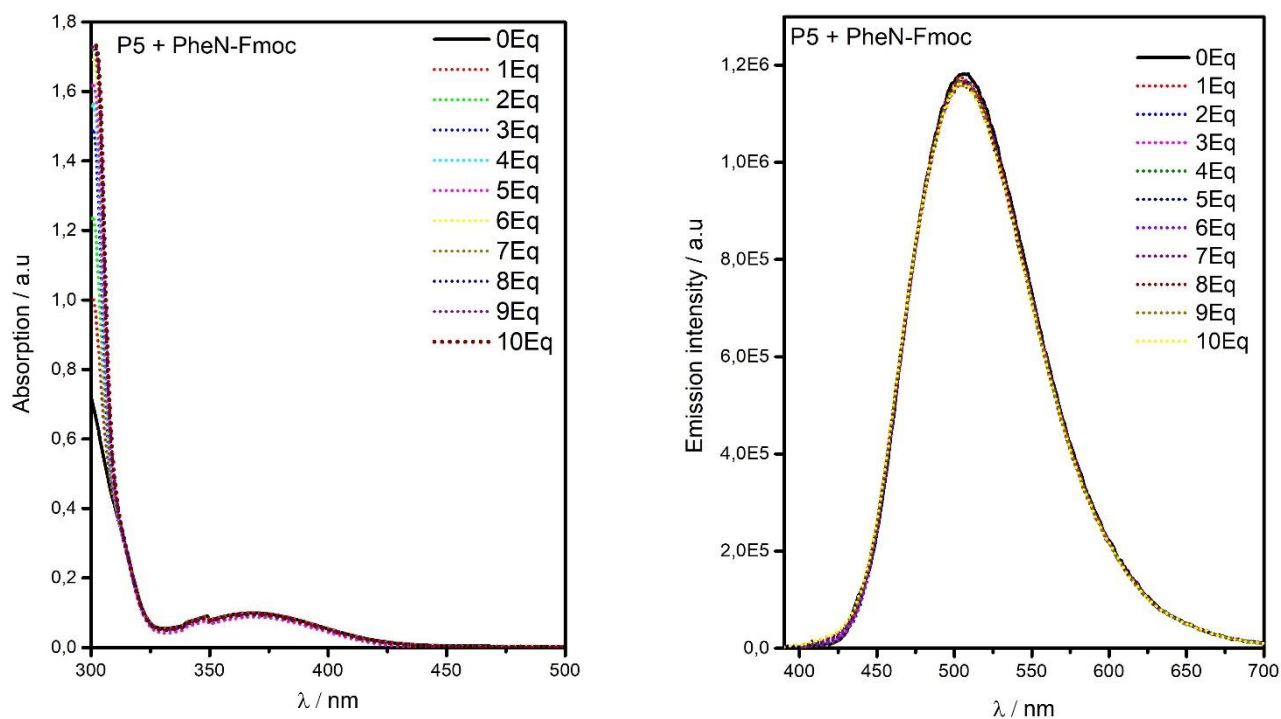

Figure 17. Changes in the absorption and PL of **4f** (10 µM) with the incremental addition of *N*-Fmoc-phenylalanine in Chloroform (λex = 350 nm).
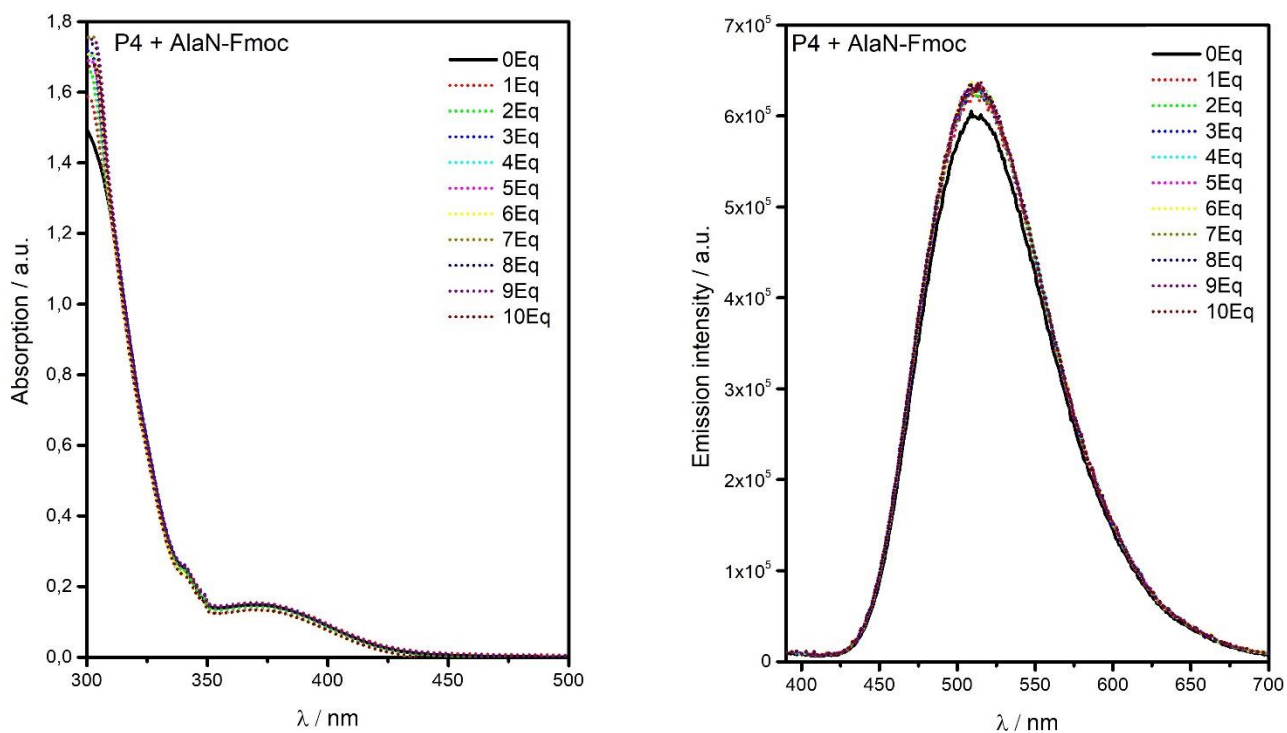
Figure 18. Changes in the absorption and PL of **P4** (10 µM) with the incremental addition of *N*-Fmoc-alanine in Chloroform (λex = 350 nm).
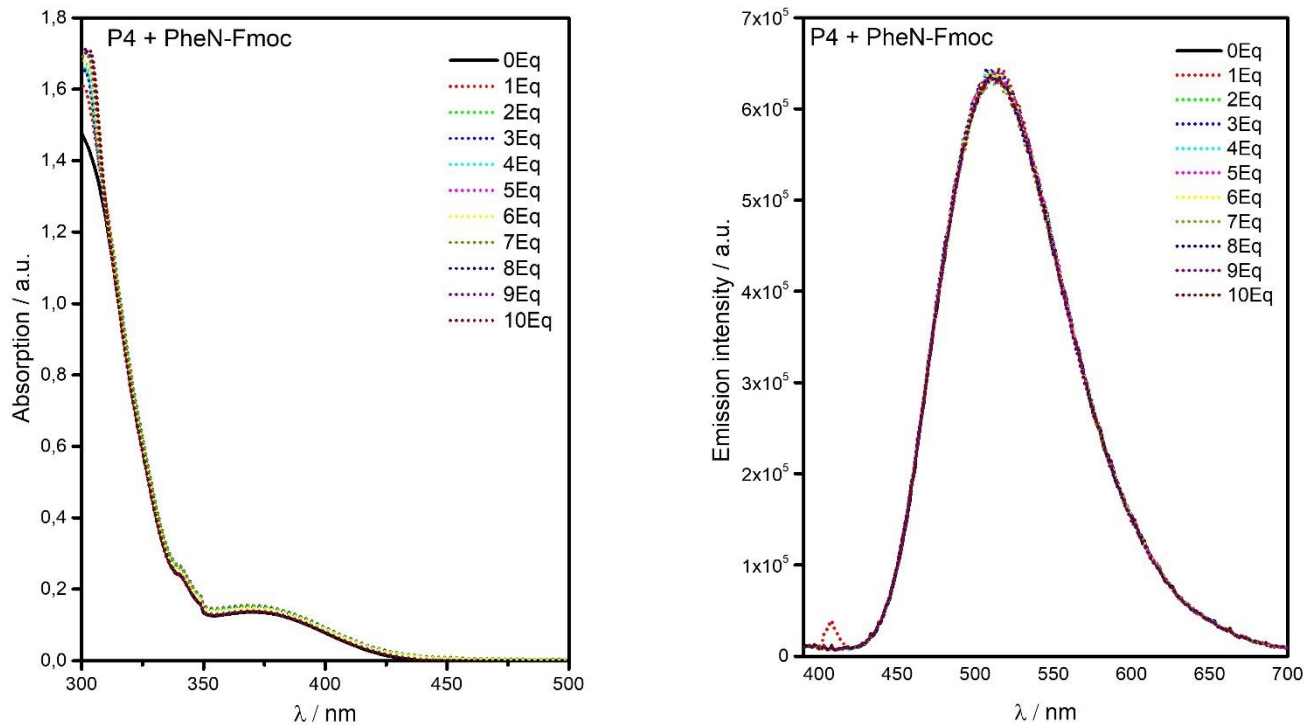
Figure 19. Changes in the absorption and PL of **P4** (10 µM) with the incremental addition of *N*-Fmoc-phenylalanine in Chloroform (λex = 350 nm).
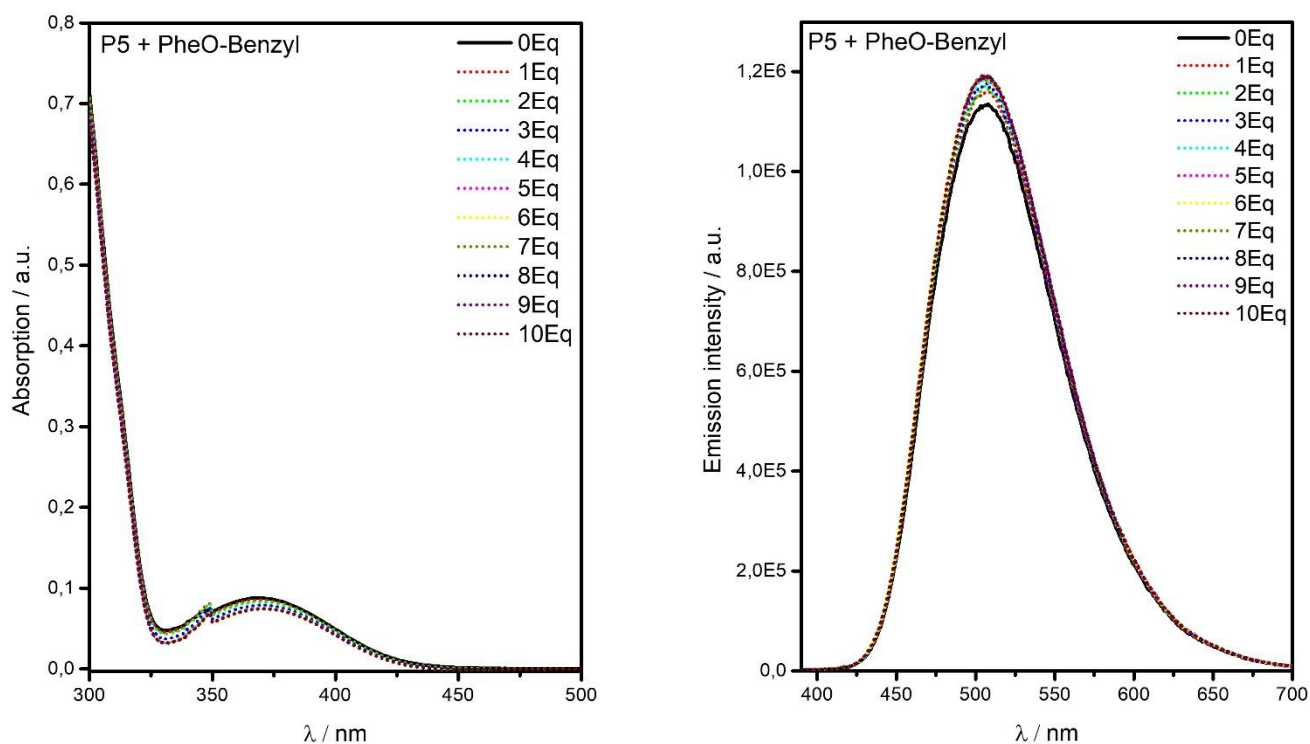
Figure 20. Changes in the absorption and PL of **P5** (10 µM) with the incremental addition of Benzyl 3-phenyl-L-alaninate in Chloroform (λex = 350 nm).
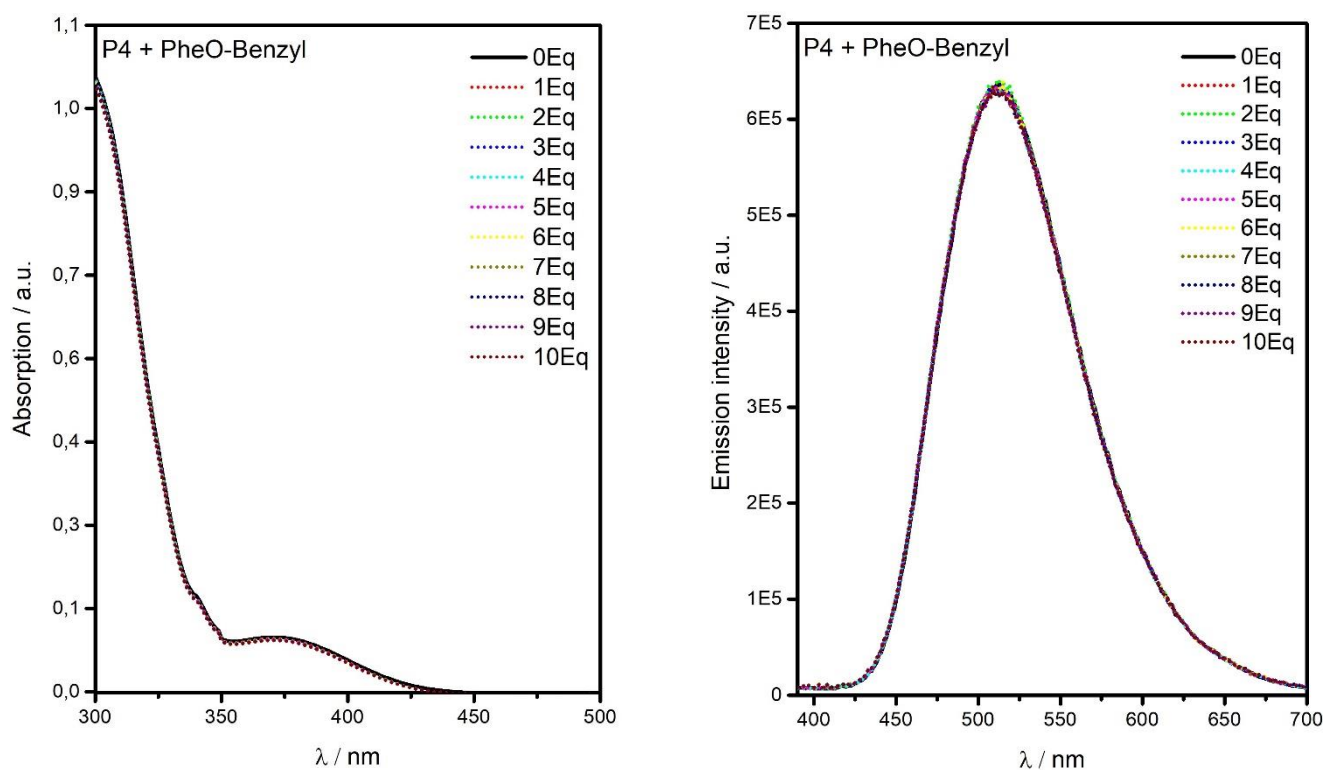
Figure 21. Changes in the absorption and PL of **P4** (10 µM) with the incremental addition of Benzyl 3-phenyl-L-alaninate in Chloroform (λex = 350 nm).
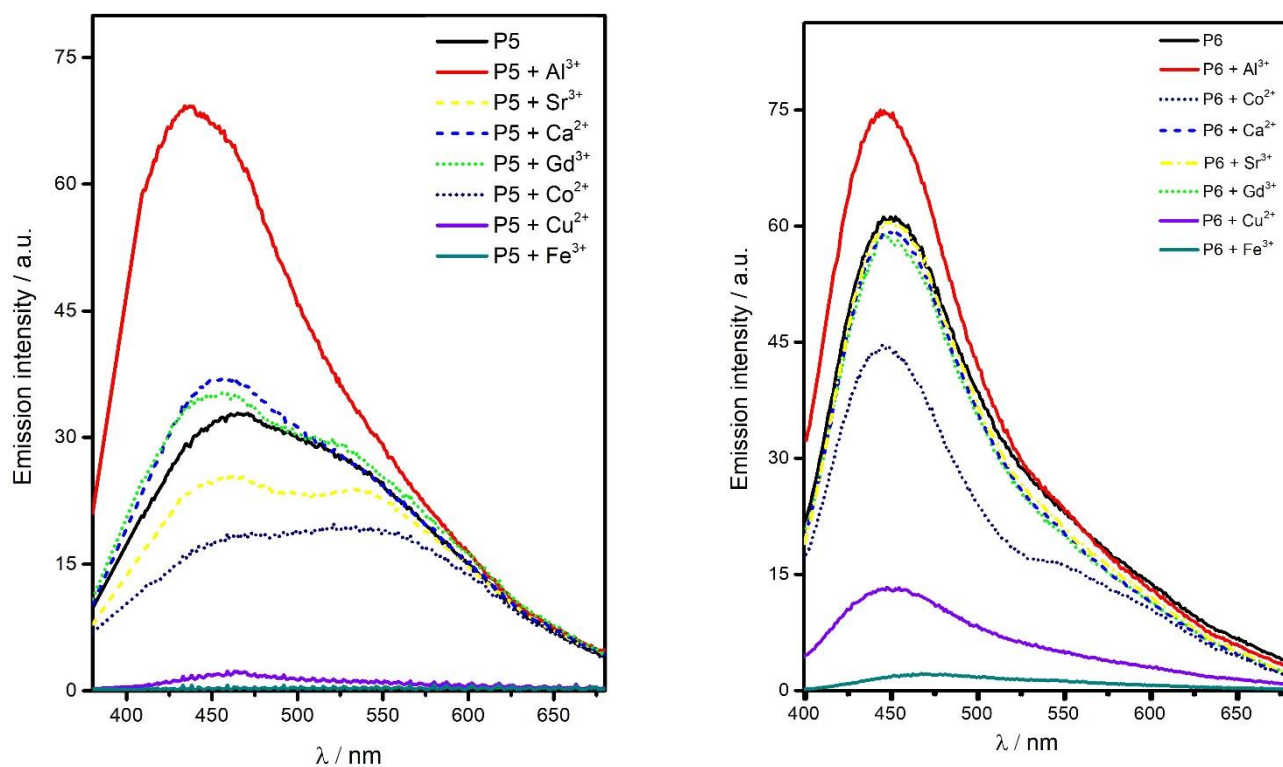
Figure 22. Fluorescence spectra of **P5** and **P6** (10 μM) in the presence of different metal ions (100 equiv.) in methanol.
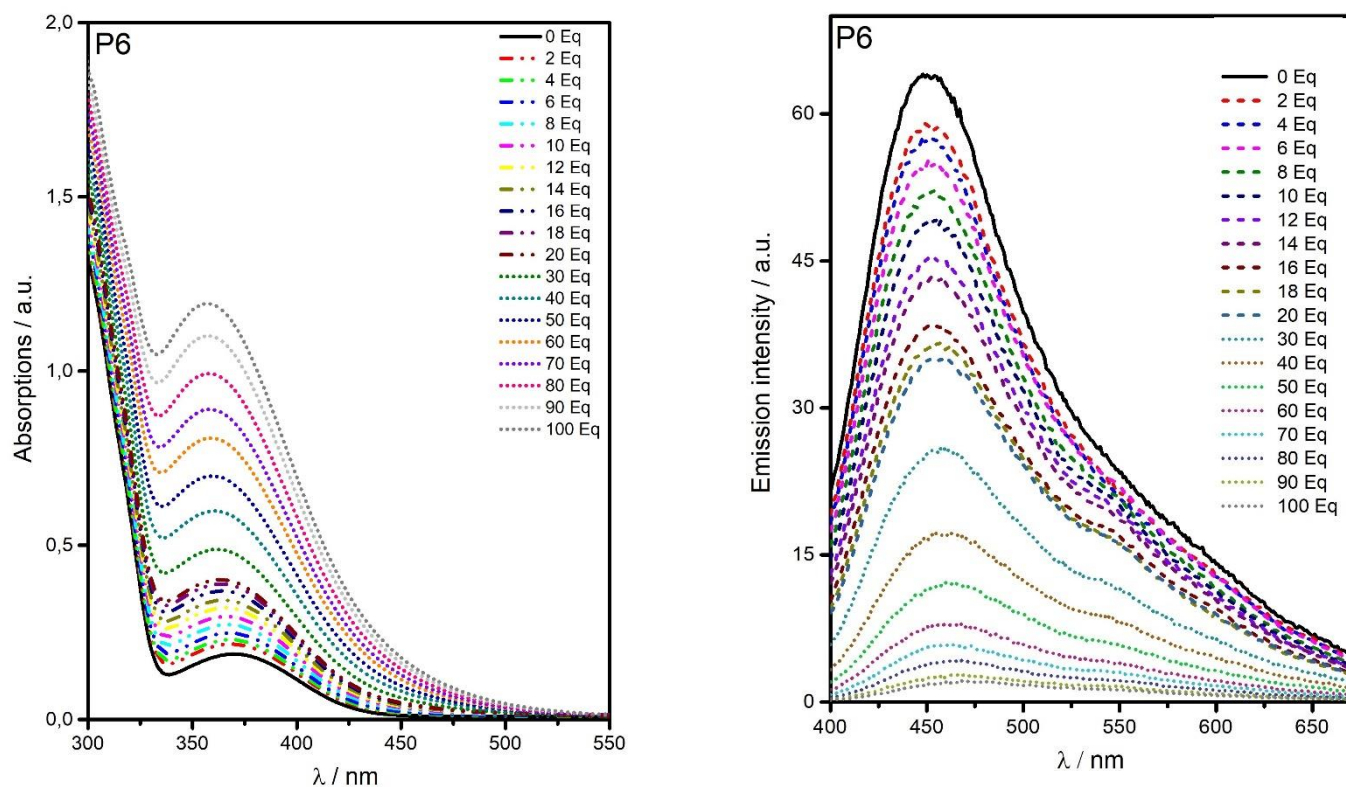
Figure 23. Absorption and PL of **P6** (10 μM) titrated with Fe3+ (0−100 equiv.) in methanol.
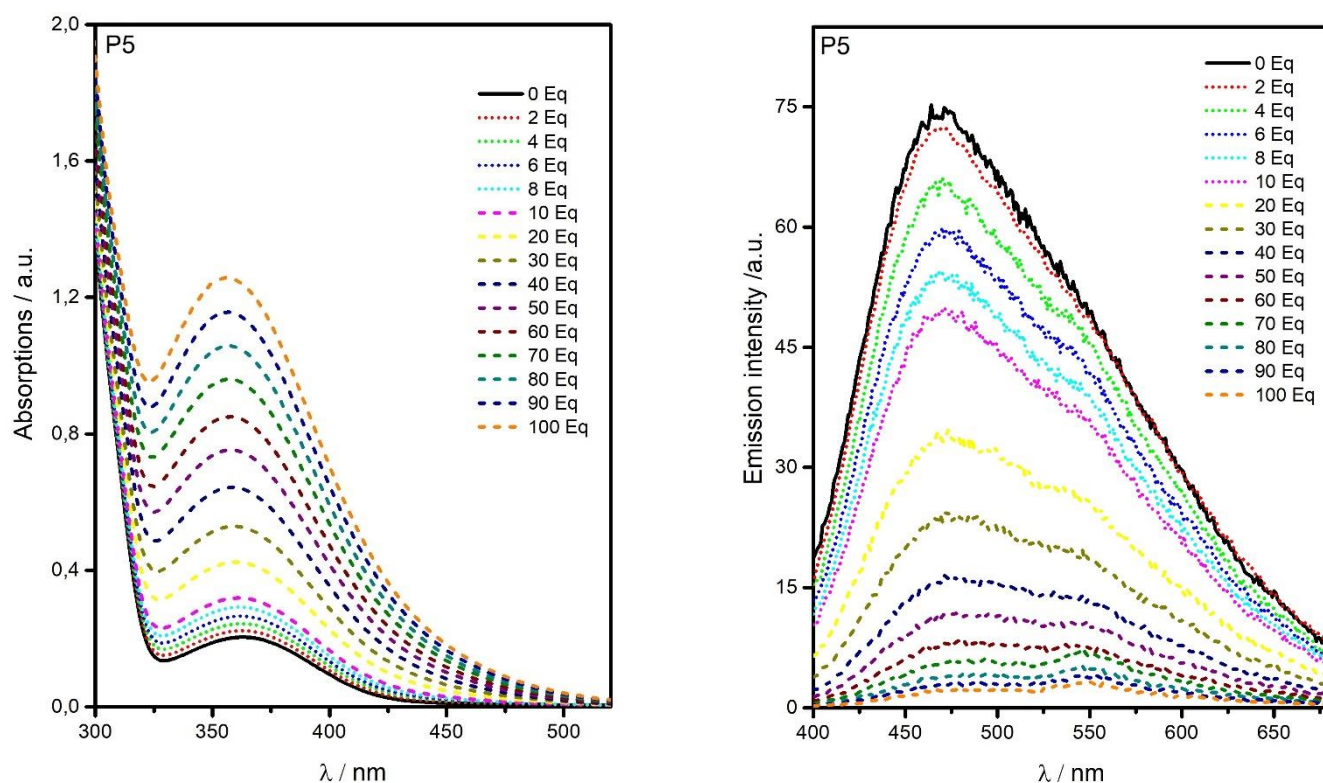
Figure 24. Absorption and PL of **P5** (10 μM) titrated with Fe^{3+} (0–100 equiv.) in methanol.

2.4.3 Cytotoxicity and bioimaging application

Finally, to assess the photophysical behavior of coumarins **P4** and **P5**, as potential biomarkers for imaging applications, we evaluated their cytotoxicity using a cell-based assay. For this purpose, Nthy-ori3–1 cells (Simian Virus 40 (SV40)-immortalized normal human thyrocytes) were treated with different concentrations (10-100 μM) of **P4** and **P5**. Cell viability was determined after 24 h at 37 °C by the MTT method.[56] As shown in Figure 25, both coumarins have proved to be not cytotoxic against cell monolayers (CC50 = >100 μM). In parallel, Nthy-ori3–1 cells were incubated with **P4** and **P5** (1.0 μM), for bioimaging studies and then analyzed by an epifluorescence microscope using blue (excitation 470–495 nm; emission 510–550 nm) and orange filters (excitation 530–550 nm; emission 575 nm). As clearly depicted in figure 26, no fluorescence was

detected in the external buffer or the nucleus whereas, collected images showed that both coumarin dyes **P4** and **P5** are emissive in the cytoplasmic compartments.
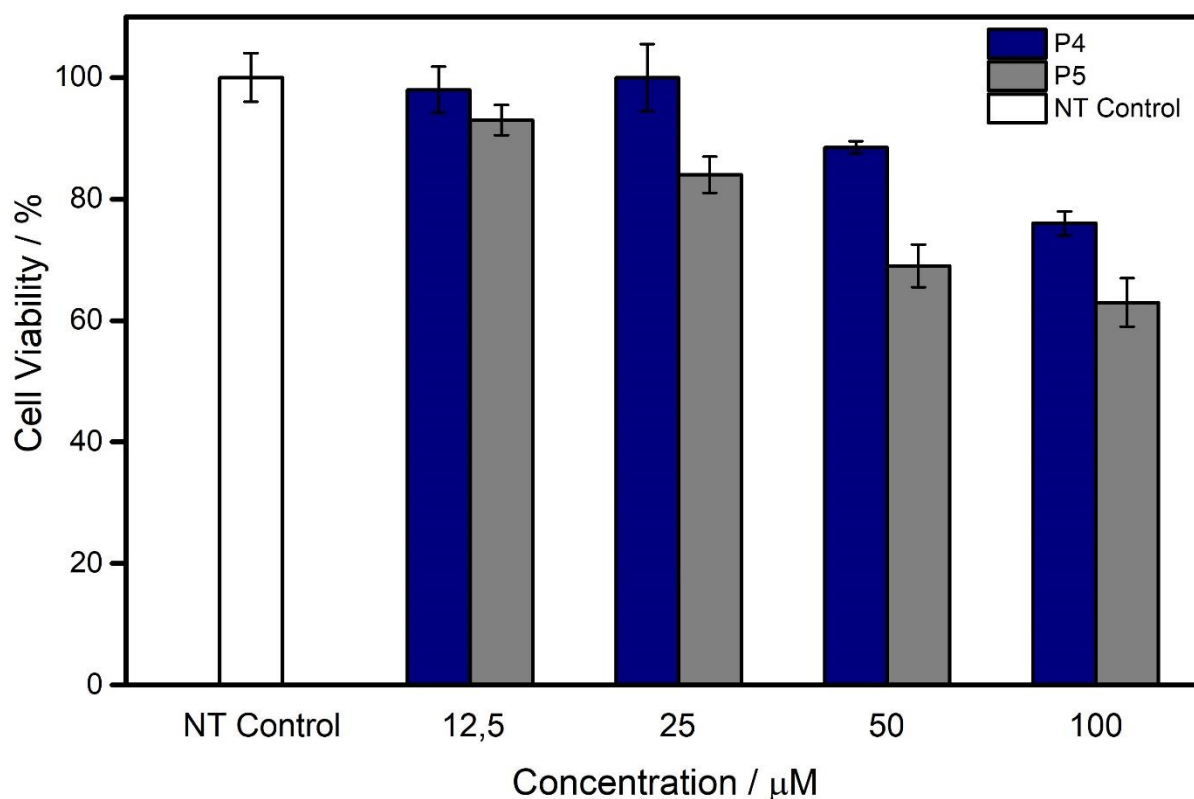
Figure 25. Viability of Nthy-ori3–1 cell line in the presence of **P4** and **P5**. Cells were treated at different concentration and cytotoxicity was determined using the MTT assay by monitoring formazan absorbance at 570 nm. Data represent mean values (±SD) for three independent determinations.

Furthermore, the intracellular environment did not affect the fluorescence properties of these compounds. These pieces of evidence prompted us to deduce that coumarins tend to interact at the cytoplasmic lipophilic substructures, as they are poorly soluble in water. However, to confirm this hypothesis, a further study will be necessary assisted by higher resolution confocal microscopes and using any contrast agents.
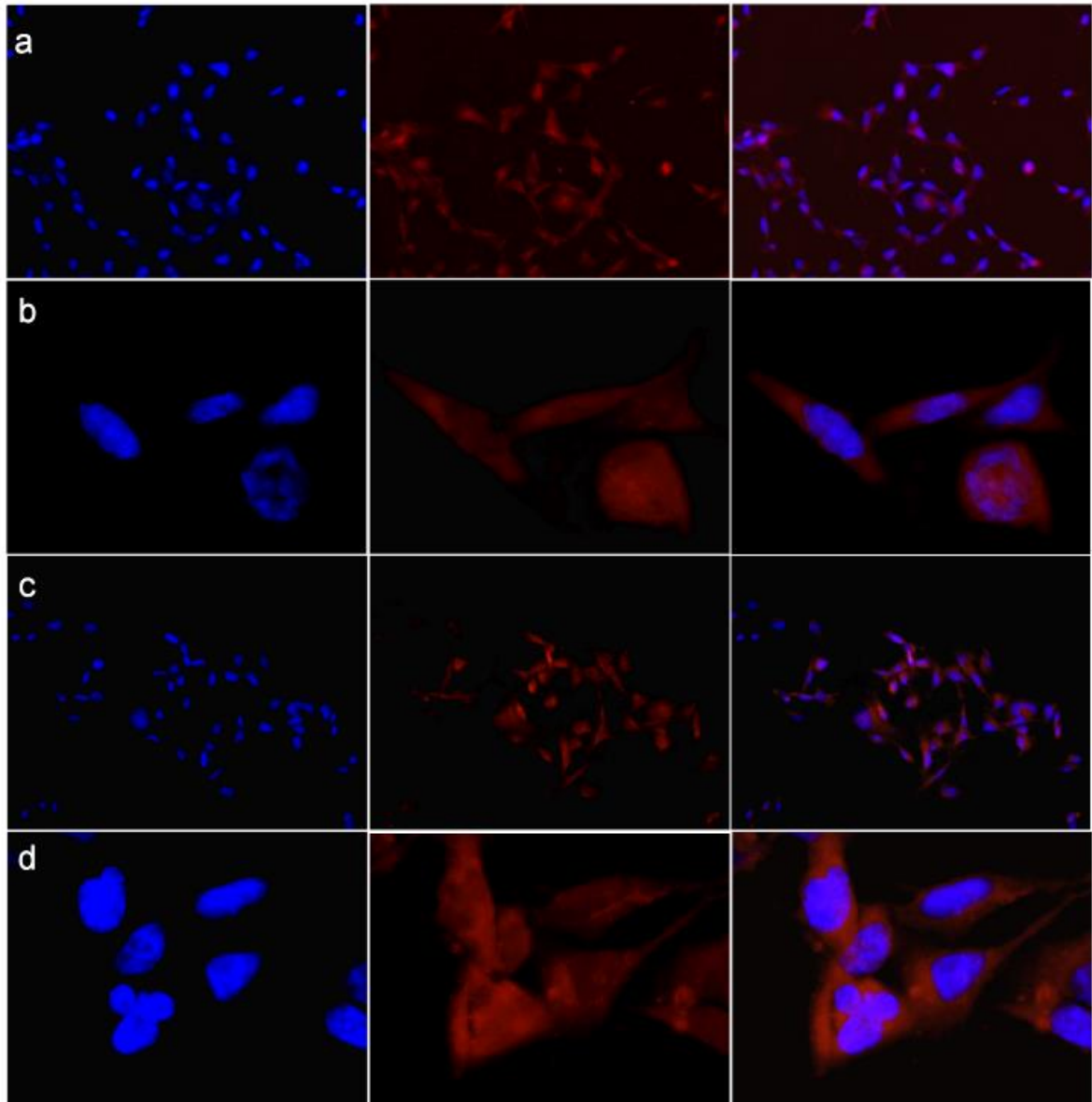
Figure 26. Bioimaging of Nthy-ori3–1 cells treated with **P4** and **P5** coumarins (1µM). a) (20X) and b) (100X) fluorescent images of Nthy-ori3–1 cells stained with DAPI (blue), **P4** (1µM) orange (excitation 530–550 nm; emission 575), overlay between **P4** and DAPI images. c) (20X) and d) (100X) fluorescent images of Nthy-ori3–1 cells stained with DAPI (blue), **P5** (1µM) orange (excitation 530–550 nm; emission 575), merged images (**P5** and DAPI).

2.5 Conclusions

The synthesis of novel D-π-A push-pull coumarins was successfully performed in a two-step's strategy affording the corresponding derivatives in good to excellent yields. The photophysical characterization of these compounds, allowed us to identify two compounds (**P5** and **P6**) with good quantum fluorescence efficiencies and their modulation by the exposition of these coumarins to increasing concentrations of Al^{3+} and Fe^{3+} solutions. Furthermore, in vitro biological assays highlighted the low toxicity of coumarins **P4** and **P5** which were therefore investigated as potential candidates for bio-imaging applications. To this end, further studies are currently underway in our laboratory, aimed at identifying the possible selectivity of these compounds towards specific cytoplasmic subunits.

2.6 References

28.   Kivala, M. & Diederich, F. Acetylene-Derived Strong Organic Acceptors for Planar and Nonplanar Push−Pull Chromophores. *Acc. Chem. Res.* **42**, 235–248 (2009).

29.   Jagtap, A. R., Satam, V. S., Rajule, R. N. & Kanetkar, V. R. The synthesis and characterization of novel coumarin dyes derived from 1,4-diethyl-1,2,3,4-tetrahydro-7-hydroxyquinoxalin-6-carboxaldehyde. *Dyes and Pigments* **82**, 84–89 (2009).

30.   Xie, L. *et al.* Fluorescent coumarin derivatives with large stokes shift, dual emission and solid-state luminescent properties: An experimental and theoretical study. *Dyes and Pigments* **92**, 1361–1369 (2012).

31.   Chethan Prathap, K. N. & Lokanath, N. K. Synthesis, characterization, crystal structure and quantum chemical investigations of three novel coumarin-benzenesulfonohydrazide derivatives. *Journal of Molecular Structure* **1158**, 26–38 (2018).

32.   Traven, V. F. *et al.* Photoinduced formation of the laser dye coumarin 6 from its dihydro derivatives. *Dyes and Pigments* **146**, 159–168 (2017).

33.   Zhou, X. *et al.* Inverted transparent multi-layered vacuum deposited organic light-emitting diodes with electrically doped carrier transport layers and coumarin doped emissive layer. *Synthetic Metals* **138**, 193–196 (2003).

34.   Beyer, B. *et al.* Small molecule bulk heterojunction organic solar cells with coumarin-6 as donor material. *Thin Solid Films* **536**, 206–210 (2013).

35.   Signore, G., Nifosì, R., Albertazzi, L., Storti, B. & Bizzarri, R. Polarity-Sensitive Coumarins Tailored to Live Cell Imaging. *J. Am. Chem. Soc.* **132**, 1276–1288 (2010).

36.   Bayrakçeken, F., Yaman, A. & Hayvalı, M. Photophysical and photochemical study of laser-dye coumarin-481 and its photoproduct in solution. *Spectrochimica Acta Part A: Molecular and Biomolecular Spectroscopy* **61**, 983–987 (2005).

37.   Yuan, S., Zhang, Y., Lu, R. & Yu, A. Photoinduced electron transfer between coumarin dyes and *N,N*-dimethylaniline in imidazolium-based room temperature ionic liquids: Effect of the cation's alkyl chain length on the bimolecular photoinduced electron transfer process. *Journal of Photochemistry and Photobiology A: Chemistry* **260**, 39–49 (2013).

38.   Liu, X. *et al.* Molecular Origins of Optoelectronic Properties in Coumarin Dyes: Toward Designer Solar Cell and Laser Applications. *J. Phys. Chem. A* **116**, 727–737 (2012).

39.   Tasior, M. *et al.* π-Expanded coumarins: synthesis, optical properties and applications. *J. Mater. Chem. C* **3**, 1421–1446 (2015).

40.   Kim, D., Xuan, Q. P., Moon, H., Jun, Y. W. & Ahn, K. H. Synthesis of Benzocoumarins and Characterization of Their Photophysical Properties. *Asian Journal of Organic Chemistry* **3**, 1089–1096 (2014).

41.   Jung, Y., Jung, J., Huh, Y. & Kim, D. Benzo[g]coumarin-Based Fluorescent Probes for Bioimaging Applications. *Journal of Analytical Methods in Chemistry* **2018**, 1–11 (2018).

42.   Yoon, S. A., Chun, J., Kang, C. & Lee, M. H. Self-Calibrating Bipartite Fluorescent Sensor for Nitroreductase Activity and Its Application to Cancer and Hypoxic Cells. *ACS Appl. Bio Mater.* **4**, 2052–2057 (2021).

43.   Yang, Y., Zhao, Q., Feng, W. & Li, F. Luminescent Chemodosimeters for Bioimaging. *Chem. Rev.* **113**, 192–270 (2013).

44.   Jun, J. V., Chenoweth, D. M. & Petersson, E. J. Rational design of small molecule fluorescent probes for biological applications. *Org. Biomol. Chem.* **18**, 5747–5763 (2020).

45.   Li, S. et al. A novel fluorescent sensor for specific recognition of GSH based on the copper complex and its bioimaging in living cells. *Bioorganic Chemistry* **100**, 103923 (2020).

46.   Shen, Y. et al. A ratiometric fluorescent probe for visualization of thiophenol and its applications. *Spectrochimica Acta Part A: Molecular and Biomolecular Spectroscopy* **230**, 118061 (2020).

47.   Wang, Z.-G. et al. A highly selective colorimetric and fluorescent probe for quantitative detection of Cu^{2+}/Co^{2+}: The unique ON-OFF-ON fluorimetric detection strategy and applications in living cells/zebrafish. *Spectrochimica Acta Part A: Molecular and Biomolecular Spectroscopy* **228**, 117763 (2020).

48.   Qiao, H. et al. A simple coumarin-based fluorescent probe for specific detection of cysteine over homocysteine and glutathione. *Chem. Pap.* **72**, 1461–1466 (2018).

49.   Gómez, M. et al. Detection of SO_2 derivatives using a new chalco-coumarin derivative in cationic micellar media: application to real samples. *RSC Adv.* **8**, 31261–31266 (2018).

50.   Sun, Q., Zhang, W. & Qian, J. A ratiometric fluorescence probe for selective detection of sulfite and its application in realistic samples. *Talanta* **162**, 107–113 (2017).

51.   Tan, Y. et al. A new fluorescent probe for Zn^{2+} with red emission and its application in bioimaging. *Dalton Trans.* **43**, 8048–8053 (2014).

52.   Colas, K., Doloczki, S., Posada Urrutia, M. & Dyrager, C. Prevalent Bioimaging Scaffolds: Synthesis, Photophysical Properties and Applications. *Eur. J. Org. Chem.* **2021**, 2133–2144 (2021).

53.   Sairam, M., Saidachary, G. & Raju, B. C. Condensation of salicylaldehydes with ethyl 4,4,4-trichloro-3-oxobutanoate: a facile approach for the synthesis of substituted 2H-chromene-3-carboxylates. *Tetrahedron Letters* **56**, 1338–1343 (2015).

54.   Costa, M., Areias, F., Abrunhosa, L., Venâncio, A. & Proença, F. The Condensation of Salicylaldehydes and Malononitrile Revisited: Synthesis of New Dimeric Chromene Derivatives. *J. Org. Chem.* **73**, 1954–1962 (2008).

55.   Kubin, R. F. & Fletcher, A. N. Fluorescence quantum yields of some rhodamine dyes. *Journal of Luminescence* **27**, 455–462 (1982).

56.   Tronci, L. *et al.* Vitamin C Cytotoxicity and Its Effects in Redox Homeostasis and Energetic Metabolism in Papillary Thyroid Carcinoma Cell Lines. *Antioxidants* **10**, 809 (2021).

Chapter 3: Design, synthesis and molecular characterization of new TADF coumarins

3.1 Introduction

The work described in this chapter is a sort of follow-up to previous research. In this case the goal was to obtain new luminescent coumarins with TADF properties for use in applications such as lighting and bioimaging. In particular, this part of the thesis is devoted to the synthesis of coumarins with delayed fluorescence (DF). In fact, although these molecular structures are well known for their optical characteristics, only three coumarins have been reported as TADF emitters to date.

In chronological order, in 2016 Qi and co-workers[57] reported the synthesis of CDPA (Figure 27), characterized by a strong red fluorescence with long emission lifetime, on the order of a microsecond (neat film) at room temperature.

MAB   **PHzBCO**   **CDPA**

Figure 27. Molecular structure of the three TADF coumarins known in literature.

This makes CDPA a building block to construct red-emitting materials in applications like luminescent devices, bio-markers for biosensor applications.

Another interesting example of coumarin-based TADF emitters is given by the ones developed by Zhang et al. in 2017[58], that are respectively the 3-methyl-6-(10H-phenoxazin-10-yl)-1H-isochromen-1-one (PHzMCO) and 9-(10H-phenoxazin-10-yl)-6H-benzo[c]-

chromen-6-one (PHzBCO) (Figure 27). These molecules are composed of D-A units, where the phenoxazine is the donor and the benzopyrone unit the acceptor. As a consequence of the similar molecular structures, these two coumarin derivatives exhibit similar photophysical properties and HOMO and LUMO distributions and close energy levels. Both materials show high PLQYs of 0.47 and 0.52 and extremely small ΔE_{ST} values of 0.018 and 0.006 eV for PHzMCO and PHzBCO, respectively. Moreover, these TADF emitters show high maximum EQEs of 17.8% for PHzMCO and 19.6% for PHzBCO in the devices.

Finally, Zhang and co-workers synthesized another TADF coumarin that emits sky-blue fluorescence (MAB, figure 27), this molecule shows an extremely small ΔE_{ST} of 0.081 eV and a high PLQY value of 67.9%. The MAB-based OLED exhibits a remarkable maximum (EQE) of 21.7%.[59]

As these coumarins shown a series of analogies with a series of compounds synthetized during our investigation, a comparison between these molecules have to be made. First of all, the acceptor group is given by the coumarin benzopyrone structure, along with the ester group, while the donor groups have been represented by heterocyclic structure such as carbazole, phenoxazine and phenothiazine functional groups.

3.2 Computational Calculations

Before starting with the synthesis of new dyes derivatives, computational calculations were run in order to value the chosen targets and values if these structures could satisfy our expectations. In particular, we looked for a ΔE_{ST} (the S_1 and T_1 energies), in order to evaluate if the designed molecules could be associated with TADF properties. The characterization of the electronic structure and optoelectronic properties of the three couma-

rins was carried out with the aid of DFT calculations. More specifically, we used a methodology that offers a particularly accurate description of the electronic structure, i.e. the PBE0 functional was adopted and the excited state properties were calculated within the Tamm-Dancoff approximation.[60]

The first step in this approach is related to the optimization of desired target structures with the aim of achieving the lowest energy values (figure 28 shows the optimized structure of the three coumarins).
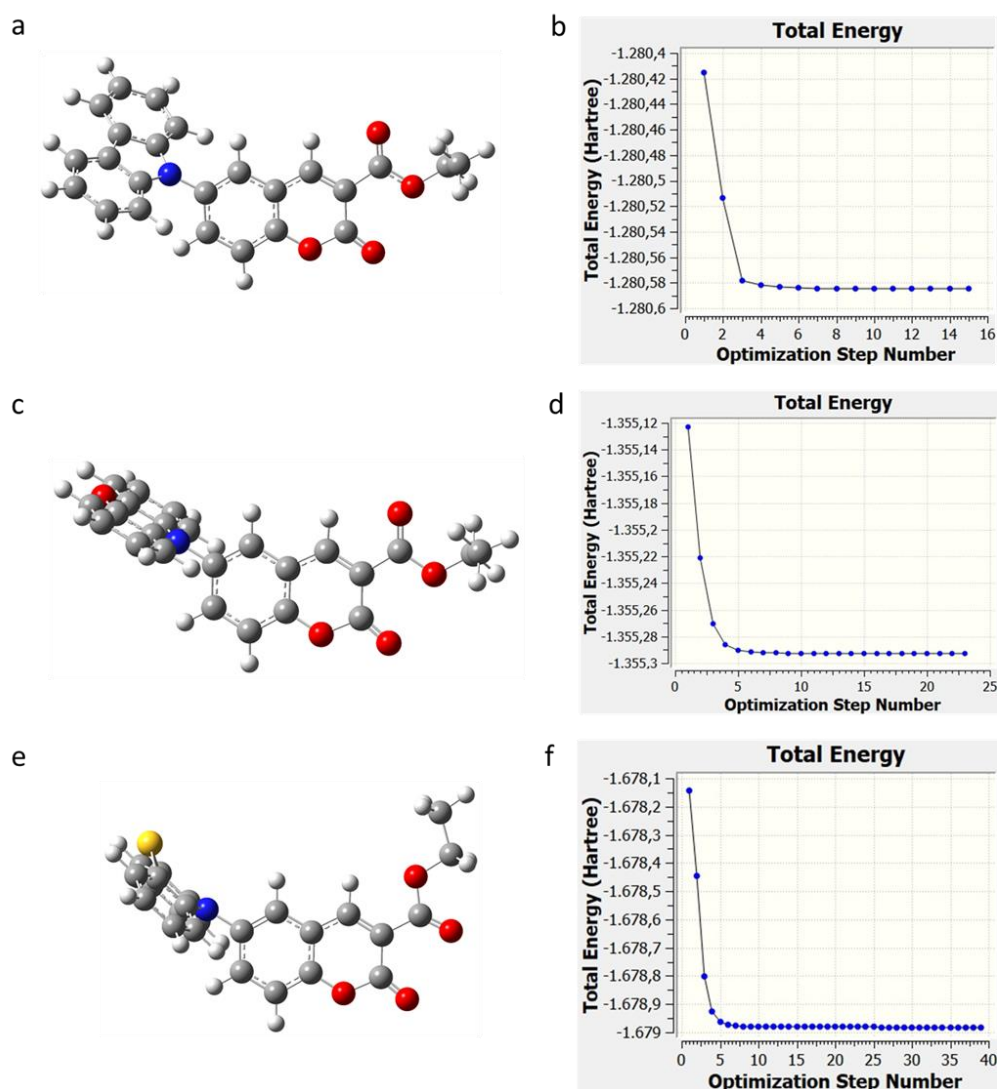
Figure 28. a) c) e) Optimized structures of **Cmr-Cz**, **Cmr-Pxz** and **Cmr-Ptz** and b) d) f) their respective graphs of the total energy. Heteroatoms: O, red; N, blue; S, green.

To corroborate our optimization process, vibration frequency calculation were performed. The absence of imaginary frequencies is generally taken as proof that we are in a minimum of energy. Finally, to extract the energies of the electronic excited states, a TDDFT calculation was performed. The results obtained after our calculations for a series of 6-functionalized coumarins were summarized in scheme 3.
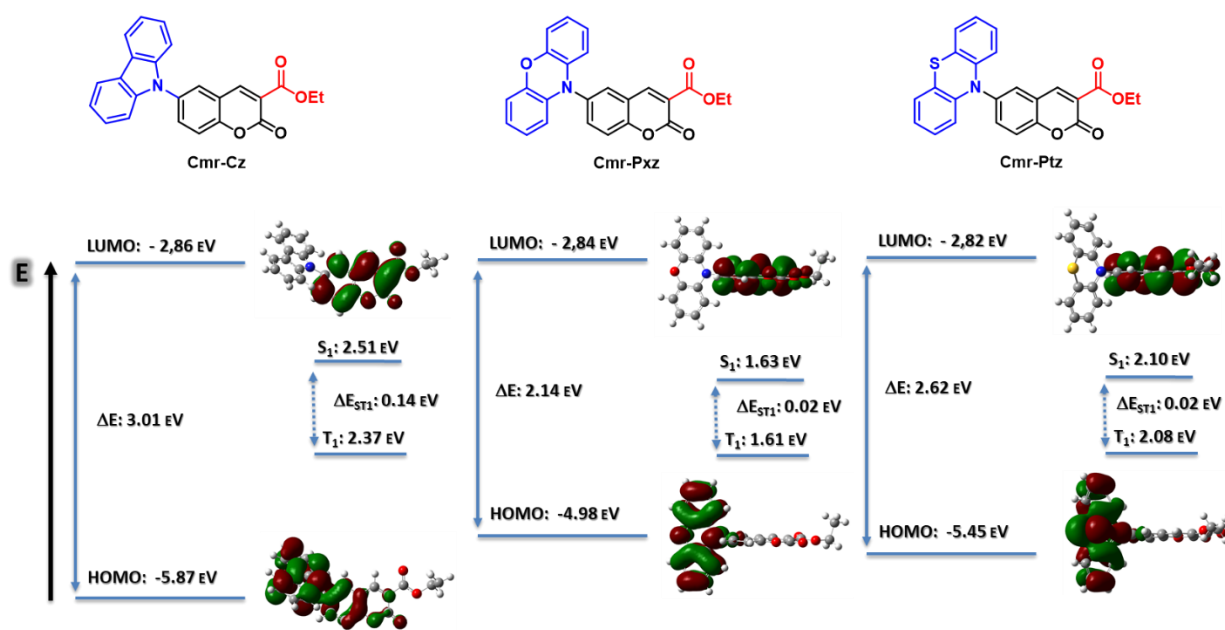
Scheme 3. Calculated HOMO and LUMO (as obtained at DFT PBE0 6-31G(d,p) level), S_1 and T_1 energies (as obtained at TDA-DFT PBE0 6-31G(d,p) level), of **Cmr-Cz, Cmr-Pxz** and **Cmr-Ptz**.

From these calculations we observed that, the LUMOs for three compounds (**Cmr-Cz**, **Cmr-Pxz** and **Cmr-Ptz**) show similar values. This result is related to the fact that the acceptor group is the same for both compounds. On the other hand, the HOMO of **Cmr-Pxz** and **Cmr-Ptz** has a higher energy than that of **Cmr-Cz**; this depends on the fact that phenoxazines and phenothiazines are well known stronger donor groups than carbazole, for two main reasons; first of all, the heteroatom contributes to the donation through mesomeric effects. Secondly, the lone pair of the nitrogen heteroatom is not involved in

the resonance and for this reason it can be easily transferred along the conjugation system, unlike in the case of carbazole. This difference in HOMO energy leads to a smaller ΔE for **Cmr-Pxz** and **Cmr-Ptz**, so the emitted radiation will have a longer wavelength.

Also, for these investigations, we could see that the f value for **Cmr-Pxz** and **Cmr-Ptz** is equal to zero, it means that the emission intensity should be zero or very low for this compound, even if a ΔE_{ST} value suitable for a TADF emission. After these evaluations, we proceeded with the synthesis of the three coumarin derivatives, following the methodologies described below in scheme 4.

3.3 Synthesis

Bromocoumarins were synthesized as described in chapter 2. Further a Pd(0) catalyzed Buchwald-Hartwig cross-coupling reaction with several N-heterocycles was performed in order to afford the corresponding products **Cmr-Cz**, **Cmr-Pxz** and **Cmr-Ptz** in good
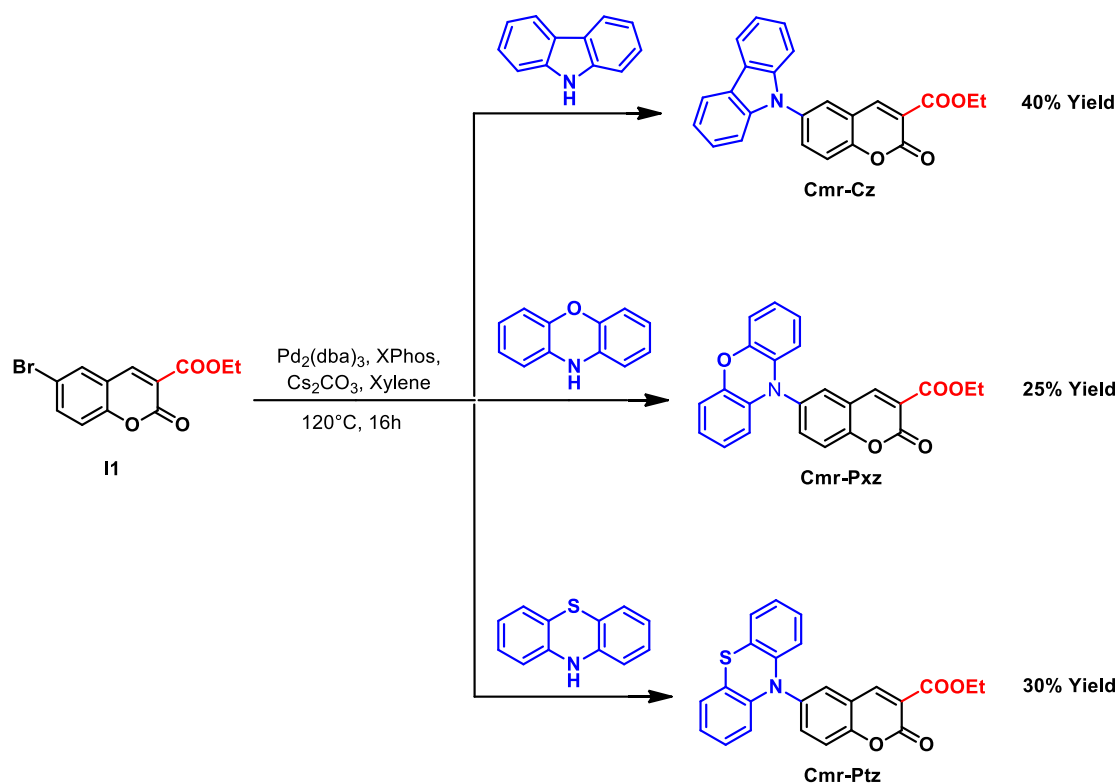
yields.

Scheme 4. Synthetic paths for the three emitters studied: **Cmr-Cz**, **Cmr-Pxz** and **Cmr-Ptz**.

With the aim of obtaining useful quantities of the compound **Cmr-Cz** and being able to perform its photophysical characterizations, we have undertaken the screening of a series of palladium (0)-based catalysts, aryl and alkylphosphines and bases (scheme 5), commonly used in Buchwald-Hartwig reactions. In fact, a first attempt based on copper-catalyzed Ullmann coupling reaction[61] was ineffective (table 4, entry 1).

On the other hand, palladium acetate[45] did not performed well, regardless of the ligand employed for this transformation (entry 2-5). However, the $Pd_2(dba)_3$ catalyst allowed us to access **Cmr-Cz** in 40% yield (entry 8).
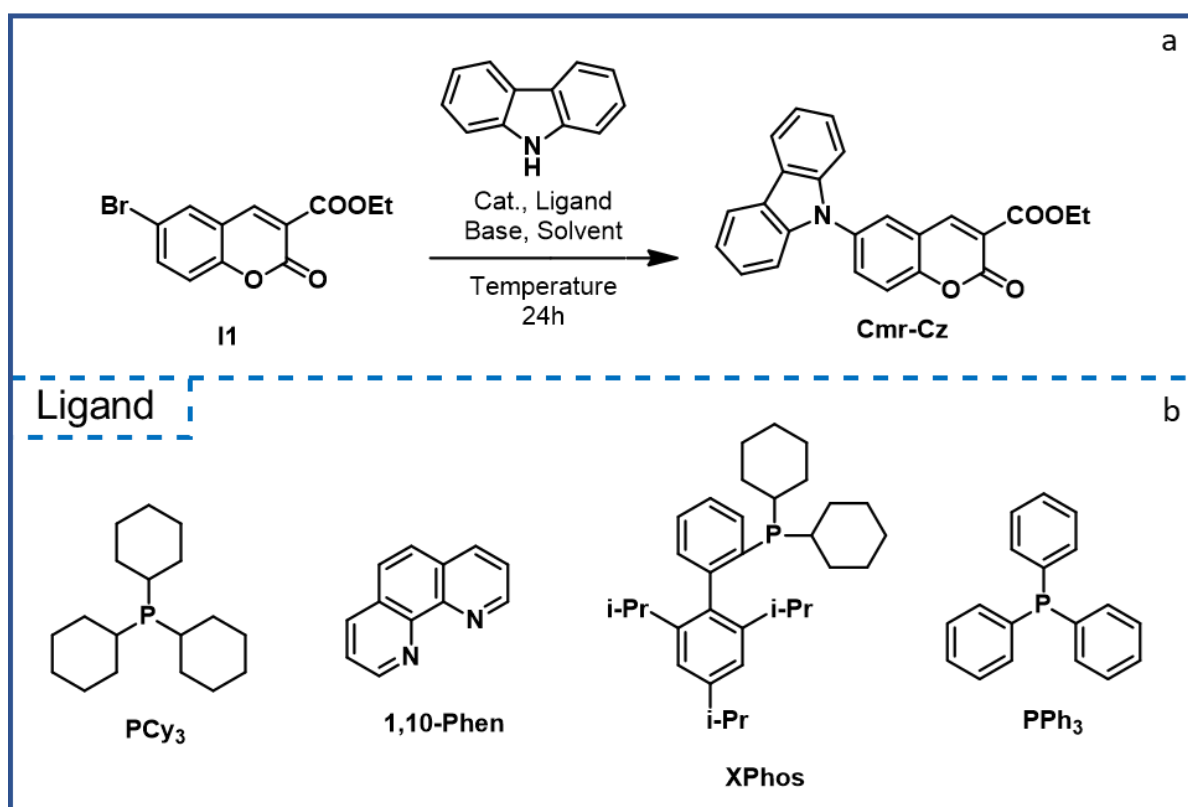
Scheme 5. a) **Cmr-Cz** Buchwald–Hartwig reaction coupling; b) molecular structures of the screened ligands.

Table 4. Coupling reaction conditions, isolated yields after flash chromatography. Reactions were performed with **I1** (130 mg, 0.4 mmol), carbazole (1.1 equiv.), base (2 equiv.), catalyst (5 mol %), ligand (10 mol %) in the solvent (3 mL) for 24 h.

entry	Catalyst (5 mol %)	Ligand (10 mol %)	Base (2 eq)	Solvent	Temperature (°C)	Yield
1	CuI	L-proline	K_2CO_3	DMSO	90	--
2	$Pd(OAc)_2$	PPh_3	K_2CO_3	Toluene	110	--
3	$Pd(OAc)_2$	PCy_3	K_2CO_3	Toluene	110	--
4	$Pd(OAc)_2$	XPhos	K_2CO_3	Toluene	110	--
5	$Pd(OAc)_2$	$[(tBu)_3PH]BF_4$	K_2CO_3	Toluene	110	--
6	$Pd_2(dba)_3$	PCy_3	Cs_2CO_3	Xylene	130	--
7	$Pd_2(dba)_3$	PCy_3	Cs_2CO_3	Xylene	130	--
8	$Pd_2(dba)_3$	XPhos	Cs_2CO_3	Xylene	130	40 %
9	$Pd(dba)_2$	XPhos	Cs_2CO_3	Xylene	130	25 %

3.4 Crystal Structures

To obtain further structural information on the synthesized coumarins, the compounds **Cmr-Cz** and **Cmr-Pxz** were recrystallized in methanol by slow evaporation and submitted for single crystal X-ray diffraction (Figures 29 and 30). **Cmr-Cz** formed light-yellow crystals, crystallized in the monoclinic space group P2$_1$/c. **Cmr-Pxz** generated red crystals in the monoclinic space group P2$_1$/c. The collected data are summarized in Table 5.

Although the **Cmr-Cz** and **Cmr-Pxz** molecules contain planar aromatic moieties and no intermolecular π-π stacking was observed. As shown in Figures 29 and 30, the torsion angle between the planes of carbazole and coumarin and of phenoxazine and coumarin are approximately 83° and 76° respectively. We also observed that solid-state packing is stabilized by the C─H···O and C─H···π interactions, suggesting that such solid-state packaging might play an important role in suppressing the radiation-free quench of fluorescence and leads to a high solid-state PLQY.
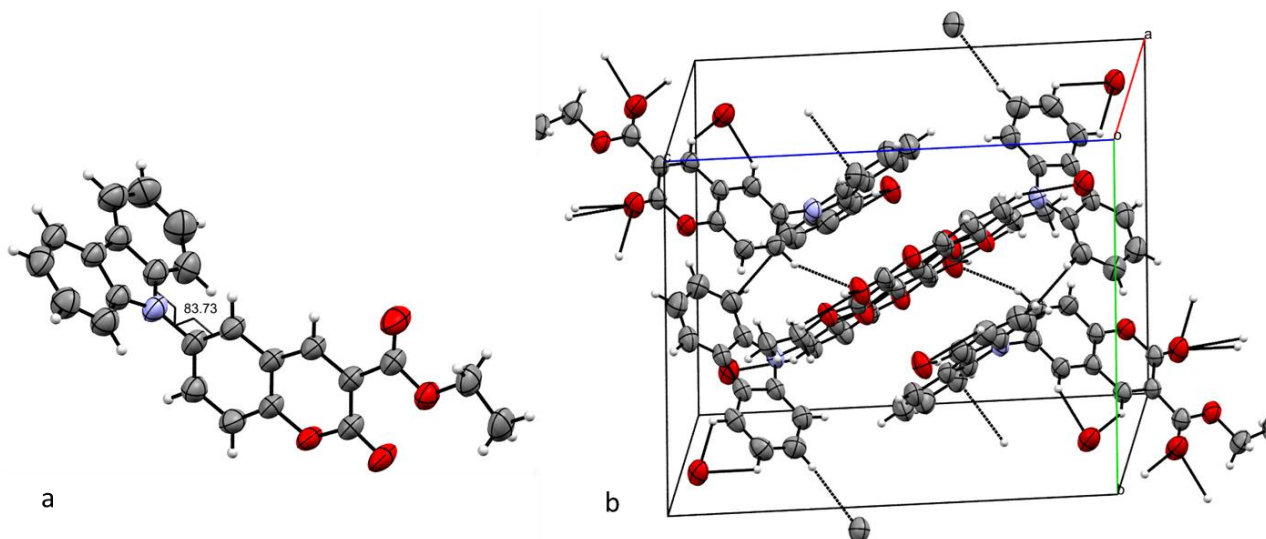
Figure 29. a) ORTEP diagram with 50% probability. b) Solid-state packing of **Cmr-Cz**. Heteroatoms: O, red; N, blue.
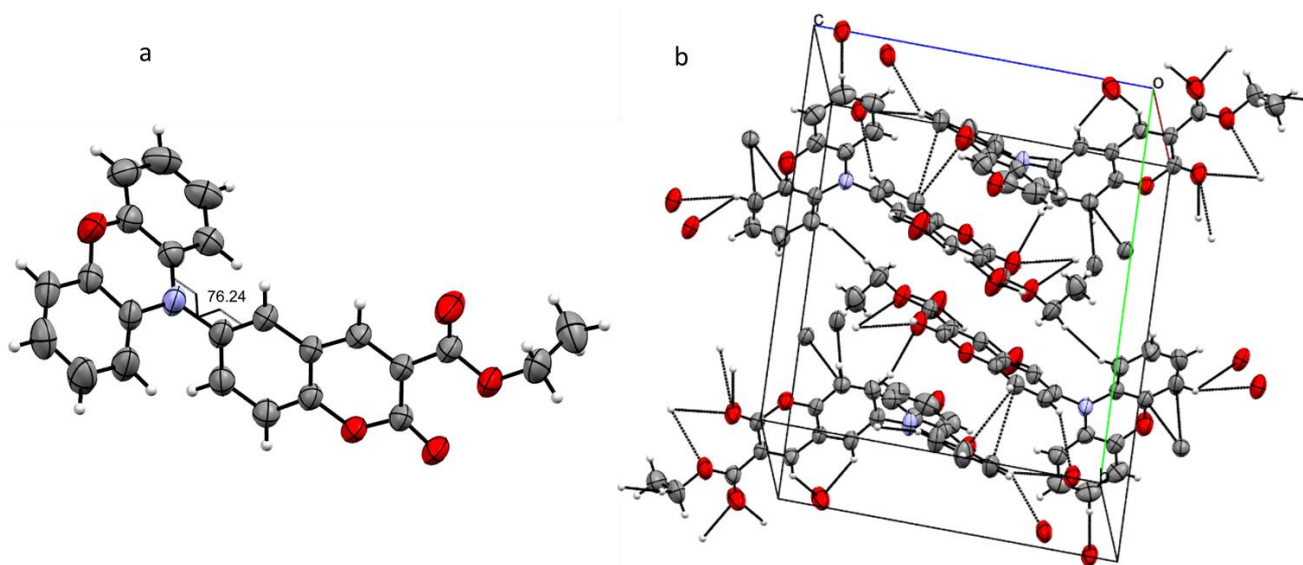
Figure 30. a) ORTEP diagram with 50% probability. b) Solid-state packing of **Cmr-Pxz**. Heteroatoms: O, red; N, blue.

Table 5. Summary of X-ray crystallographic data for **Cmr-Cz** and **Cmr-Pxz**.

	Cmr-Cz	Cmr-Pxz
Chemical formula	$C_{24}H_{17}NO_4$	$C_{24}H_{17}NO_5$
Formula weight	383,40	399,40
Space group	$P2_1/c$	$P2_1/c$
a (Å)	9.0714(8)	8.5019(9)
b (Å)	13.6004(12)	16.8093(18)
c (Å)	15.9078(12)	13.7240(14)
α (°)	90	90
β (°)	102.614(3)	105.442(4)
γ (°)	90	90
V (Å^3)	1915.25	1890.51
Z	4	4
R-Factor (%)	5.26	5.59

3.5 Photophysical characterization

Once the molecules were synthesized, photophysical properties were studied. As depicted in figure 31, **Cmr-Cz** shows an absorption band with a maximum around 375 nm which has been attributable to S_0-S_1 transition. On the other hand, the coumarins **Cmr-Pxz** and **Cmr-Ptz**, showed a red shift with an absorption maximum around 425 nm.
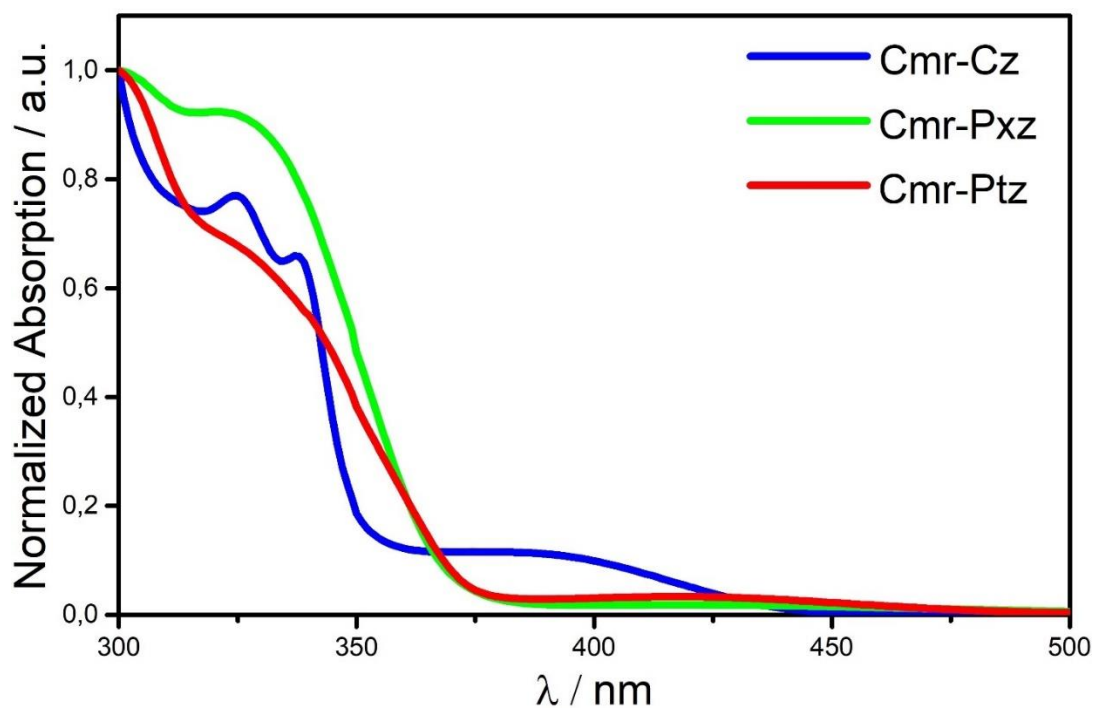
Figure 31. Absorption spectra of **Cmr-Cz**, **Cmr-Pxz** and **Cmr-Ptz** in chloroform, with a concentration of 10^{-5} M.

Based on the recorded absorption spectra, photoluminescence measurements in solution were carried out by exciting the target molecules at the maximum absorption wavelength. As regards the **Cmr-Cz** we observed an emission in the green region while for the other two coumarins an appreciable luminescence was not observed.

A solvatochromic study was then carried out for coumarin **Cmr-Cz** using four different solvents (chloroform, diethyl ether, toluene and hexane). The recorded emission spectra of these solutions showed strong positive solvatochromic effects. The emission measurements in different solvents are summarized in Figure 32 (and Table 6).
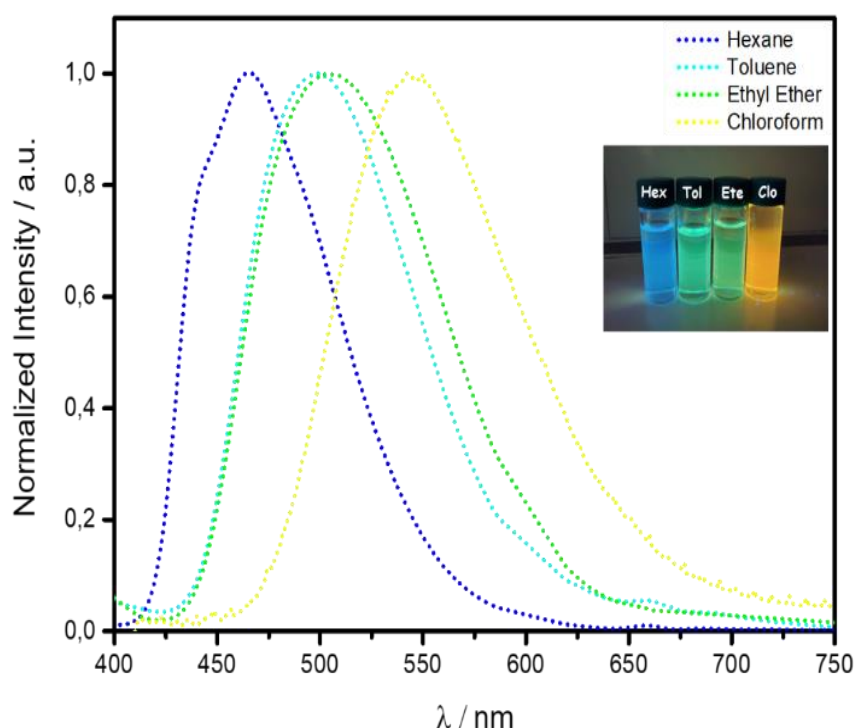
Table 6.

Solvent	λ_{PL} (nm)
n-hexane	464
toluene	497
diethyl ether	505
chloroform	544

Figure 32. Emission spectra (left) of **Cmr-Cz** in different solvents (*n*-hexane, toluene, diethyl ether, chloroform), with a concentration of 10-5 M (λex = 350 nm), showing solvatochromic red effect shift. The table 6 summarizes the λ_{PLmax}.

In addition, lifetime measurements (figure 33) and PLQY analyzes in solution were carried out. From these experiments, we extrapolated that coumarin **Cmr-Cz** exhibit a lifetime of about 10 ns, and a PLQY of about 37% (in chloroform solution using with a reference Rhodamine 6G).
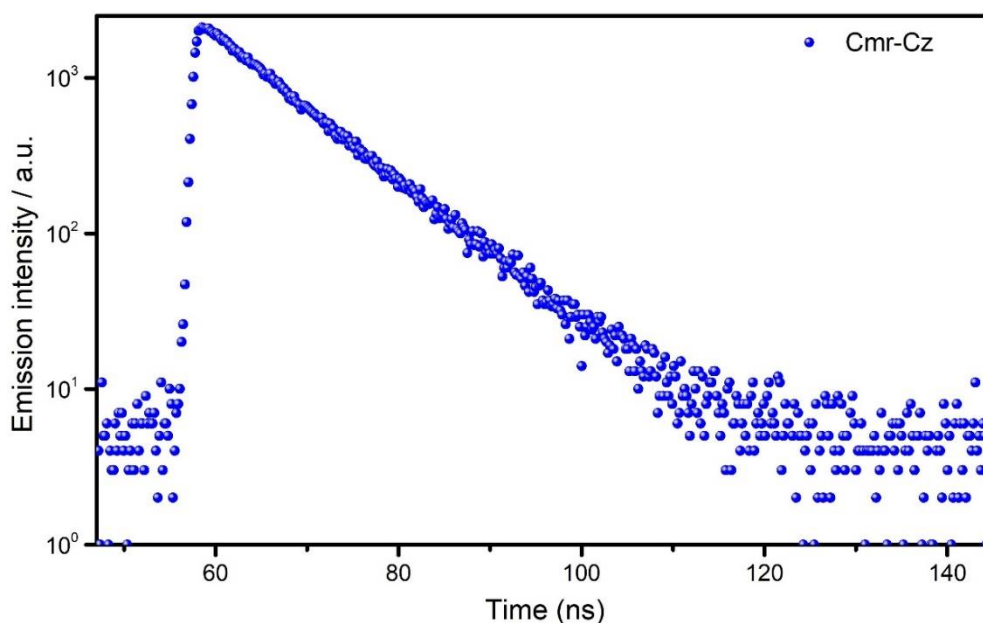
Figure 33. Decay time plot of **Cmr-Cz** excited at 350 nm in chloroform.

Then, another parameter that was been investigated was the thermal stability of the molecule, to do this a thermogravimetric analysis (TGA) was carried out. The experiment consists in the continuous measurement over time of the variation in mass of the sample as a function of temperature, in conditions of an inert atmosphere. As shown in figure 34, the decomposition temperatures (T_d with 5% weight loss) of **Cmr-Cz** was about 260°C.
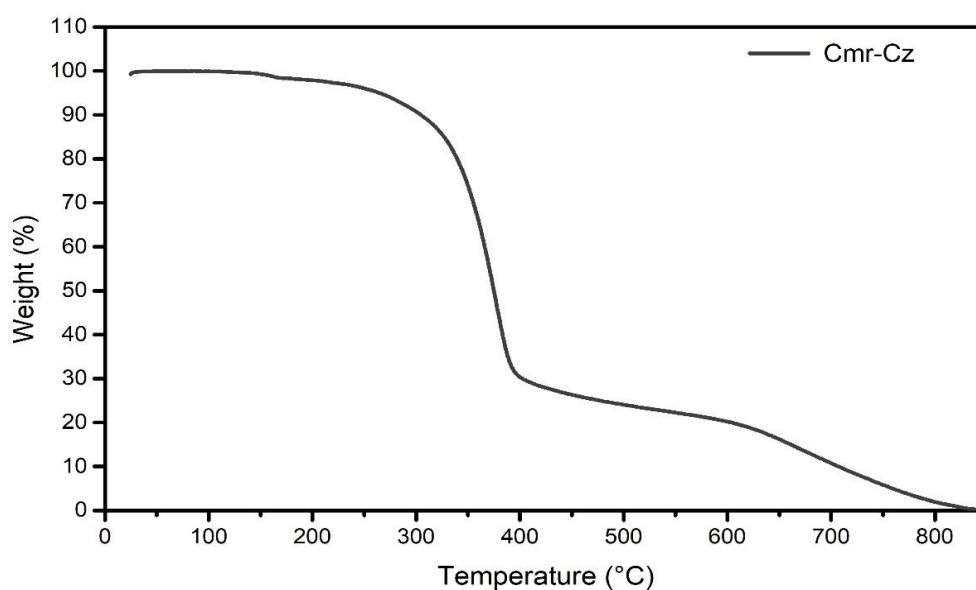
Figure 34. Cmr-Cz coumarin thermogram.

Thin-film state photoluminescence measurements were carried out using coumarin con-
taining PMMA disperse film. Figure 35 shows the excitation and emission spectra. As
expected **Cmr-Cz** emits in the green region with λ_{max} centered at 520 nm while the cou-
marin **Cmr-Pxz** emits in the red with a λ_{max} of 610 nm. This difference is in full agreement
with the computational date. Coumarin **Cmr-Ptz** showed an emission maximum at 580
nm, in good agreement with our computational calculations.
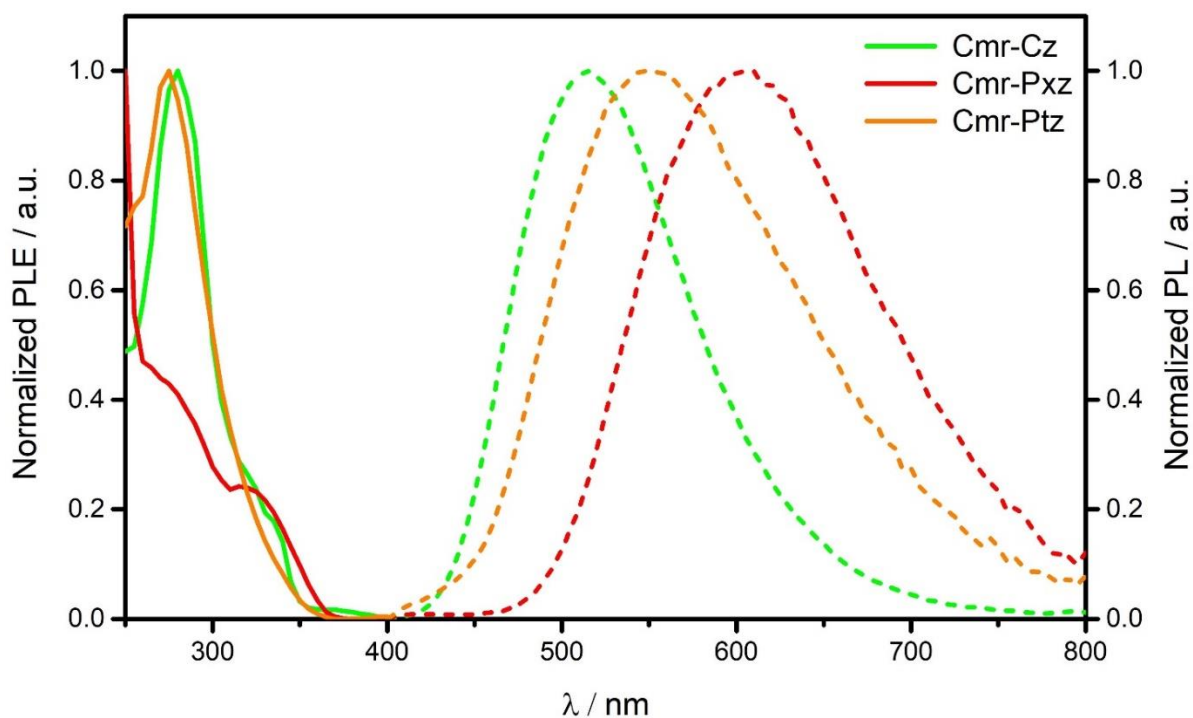
Figure 35. Excitation and photoluminescence spectra of **Cmr-Cz**, **Cmr-Pxz** and **Cmr-
Ptz** (10 wt% in PMMA films).
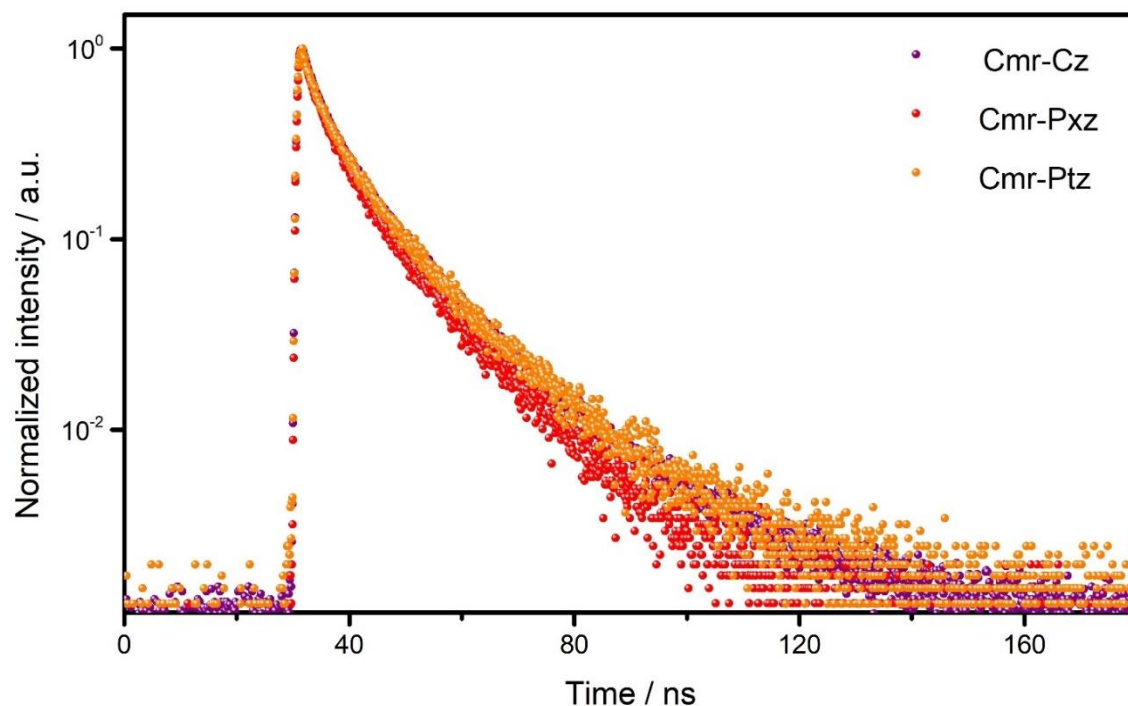
Figure 36. PL decays of **Cmr-Cz, Cmr-Pxz** and **Cmr-Ptz** excited at 350 nm (10 wt% in PMMA films).

Furthermore, lifetimes measurements and PLQY for the coumarin dyes were performed and the result summarized in table 7.

Table 7. Cmr-Cz, **Cmr-Pxz** and **Cmr-Ptz** maximum emission, lifetimes and PLQY (10 wt% in PMMA films under air).

	λ_{PL} (nm)	τ (ns)	PLQY (%)
Cmr-Cz	520	15	8.8
Cmr-Pxz	610	14	0.3
Cmr-Ptz	580	16	0.2

Since coumarin **Cmr-Cz** was the only derivative showering relevant PLQY, further in-vestigations were conducted to in order to value its TADF properties. For this reason

time-resolved measurements under vacuum were run with the aim to highlight delayed fluorescence (DF). Time-resolved temperature-dependent measurements were conducted at low temperatures to identify the phosphorescence peak.

The comparisons of the analyzes carried out in neat film at 10^{-4} atm are depicted in figure 37.
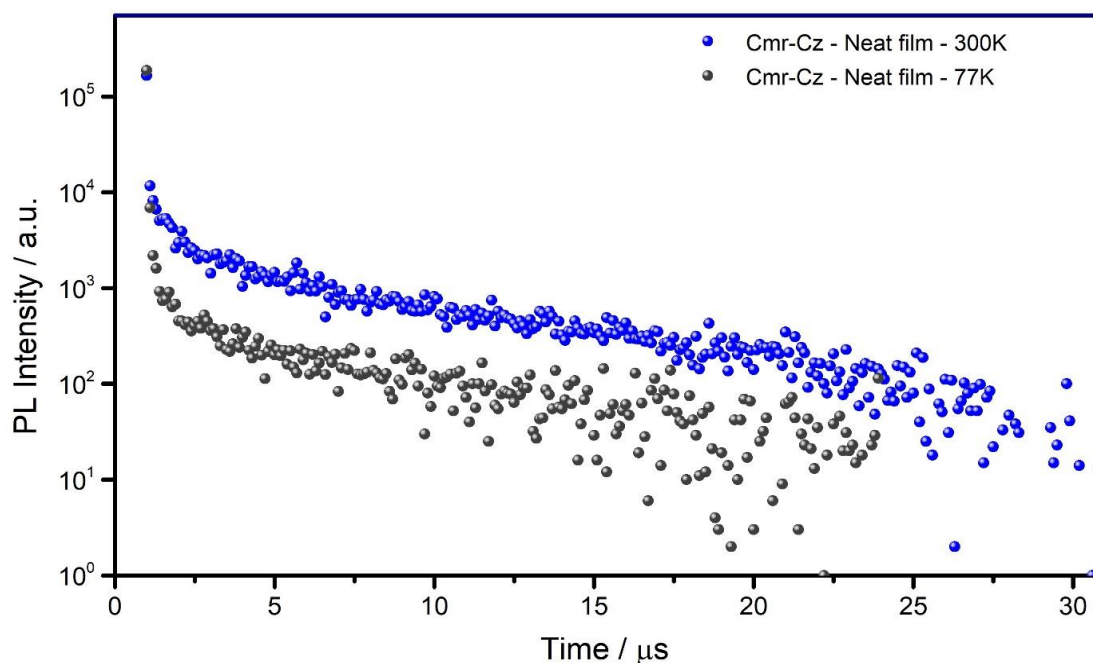
Figure 37. Comparison of **Cmr-Cz** DF intensity at different temperatures (300K and 77K) on neat film.

However, the measurement carried out at 300K allowed as to highlight a delayed fluorescence with a lifetime of about 7 µs. These temperature-dependent decays confirm the assignment of the emission as thermally activated retarded fluorescence. At 300 K the molecule has sufficient thermal energy to bridge the energy gap, ΔE_{ST}, between S_1 and T_1. rISC proceeds and repopulates the S_1 state giving rise to delayed fluorescence and the depopulation of the T_1 state suppresses the phosphorescence. When the sample is cooled to 77 K, this situation is reversed, the molecule no longer has sufficient

thermal energy to overcome ΔE_{ST} and rISC is turned off, which results in suppressed delayed fluorescence and increased phosphorescence. Signals recorded at lower temperatures showed lower intensities than those recorded at high temperatures by about an order of magnitude. This behavior confirms our calculations which indicated **Cmr-Cz** as a new TADF dye.

In figure 38 there is a comparison of different bands, emitted with an excitation delay of 5 ns and with a delay of 20 ms from excitation at 77K. These two signals represent fluorescence and phosphorescence emissions, respectively. The phosphorescence band is shifted towards the red of about 80 nm with respect to the fluorescence band, this is because the T_1 state has a slightly lower energy than the S_1 state, so the energy gap with the ground state is smaller and therefore the emission gives a radiation with a lower frequency and greater wavelength.

In Table 8 we reported the calculated values of S_1, T_1 and the lifetime of prompt and delayed fluorescence. These data are in agreement with our calculations which indicated **Cmr-Cz** as a new TADF.

Table 8. Experimental values of S_1, T_1 and the lifetime of prompt and delayed fluorescence.

Emitter	S_1 (eV)	T_1 (eV)	ΔE_{ST} (eV)	τ_p (ns)	τ_d (µs)
Cmr-Cz	2,50	2,32	0.18	12	7
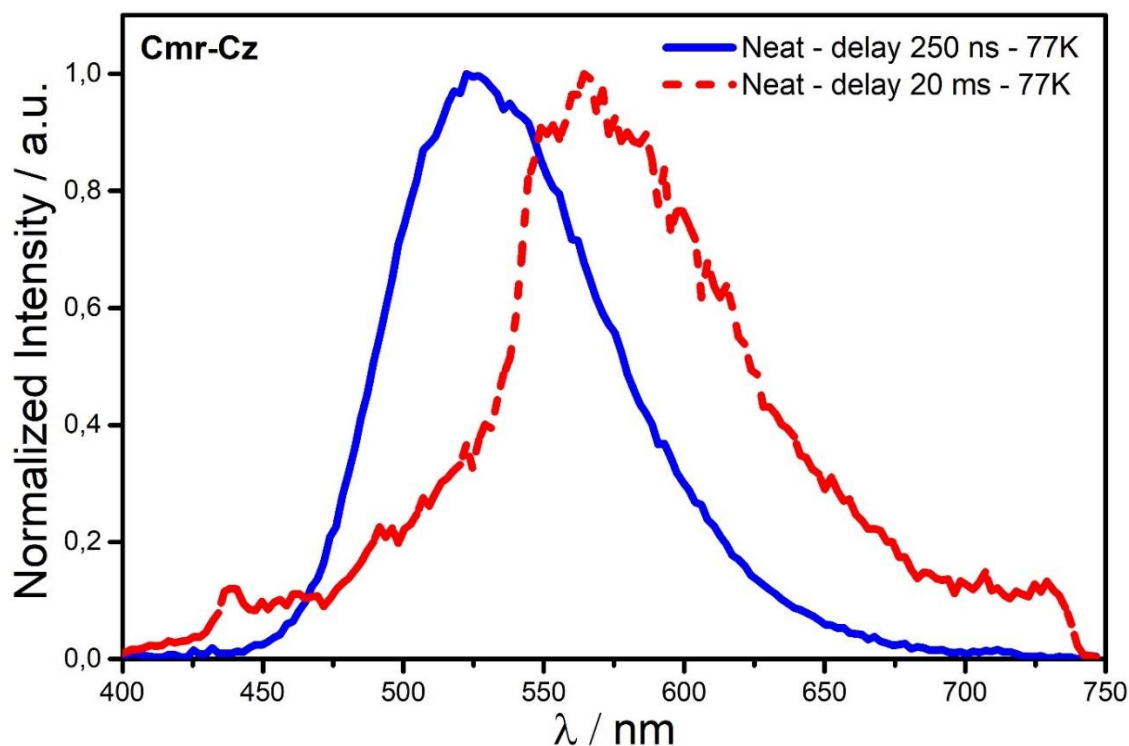
Figure 38. **Cmr-Cz** emission signals (5 ns and 20 ms) after excitation on neat film.

3.6 Cytotoxicity and bioimaging application

To evaluate the photophysical behavior of coumarin **Cmr-Cz**, as a potential biomarker for imaging applications, we evaluated their potential cytotoxicity in a cellular test. The antiproliferative activity of Coumarin **Cmr-Cz** was evaluated against a series of human cell lines derived from haematological tumors (CCRF-CEM, acute lymphoblastic leukemia, T cells; WIL2-NS, lymphoblastoid splenic leukemia, B cells) and solid (SK-MES-1, lung carcinoma; Vero-76, "normal" monkey kidney epithelial cells). Antitumor agents such as Vincristine and Etoposide were used as reference compounds. Preliminary data show an interesting activity of **Cmr-Cz** against haematological tumors with CC_{50} values equal to 0.8 µM and 1 µM (respectively on CCRF-CEM and WIL2-NS). This good activity against lymphoblastoid cell lines is also maintained against lung cancer SK-MES-1 (CC50 = 3 µM). **Cmr-Cz** was found to be non-cytotoxic (CC50 = 100 µM), also showing

a certain selectivity (SI ≥100) towards the normal Vero-76 line. Further studies are underway to verify whether this selectivity is also confirmed against "normal" human cell lines such as CRL-7065 and MRC-5. The results are shown in table 9.

Table 9. Antiproliferative activity *in vitro* of **Cmr-Cz** against normal Monkey kidney-derived cell line, against solid tumour-derived (SK-MES-1) and human leukaemia-/lymphoma-derived cell lines. [a]Compound concentration (µM) required to reduce cell proliferation by 50 %, as determined by the MTT method, under conditions allowing untreated controls to undergo at least three consecutive rounds of multiplication. [b]Normal Monkey kidney; [c]Human lung carcinoma; [d]CD4+ human acute T-lymphoblastic leukaemia. [e]Human splenic B-lymphoblastoid cells; VP16 = Etoposide.

Compds	[b]Vero-76	[c]SK-MES-1	[d]CCRF-CEM	[e]WIL-2NS
	[a]CC_{50} [µM]			
Cmr-Cz	100	3 *	<0.8	1
Reference Compounds				
Vincristine	-	0.08	>20	0.01
VP-16	-	1.0±0.3	0.09±0.01	0.2±0.005

Finally, the Nthy-ori3-1 cells were incubated with **Cmr-Cz** (1.0 µM), for bioimaging studies and then analyzed with an epifluorescence microscope using blue filters (excitation 470-495 nm; emission 510-550 nm) and orange (excitation 530-550 nm; emission 575 nm). As illustrated by Figure 39, no fluorescence was detected in the external buffer or

nucleus, while the collected images showed that **Cmr-Cz** coumarin is emissive in the cytoplasmic compartments.
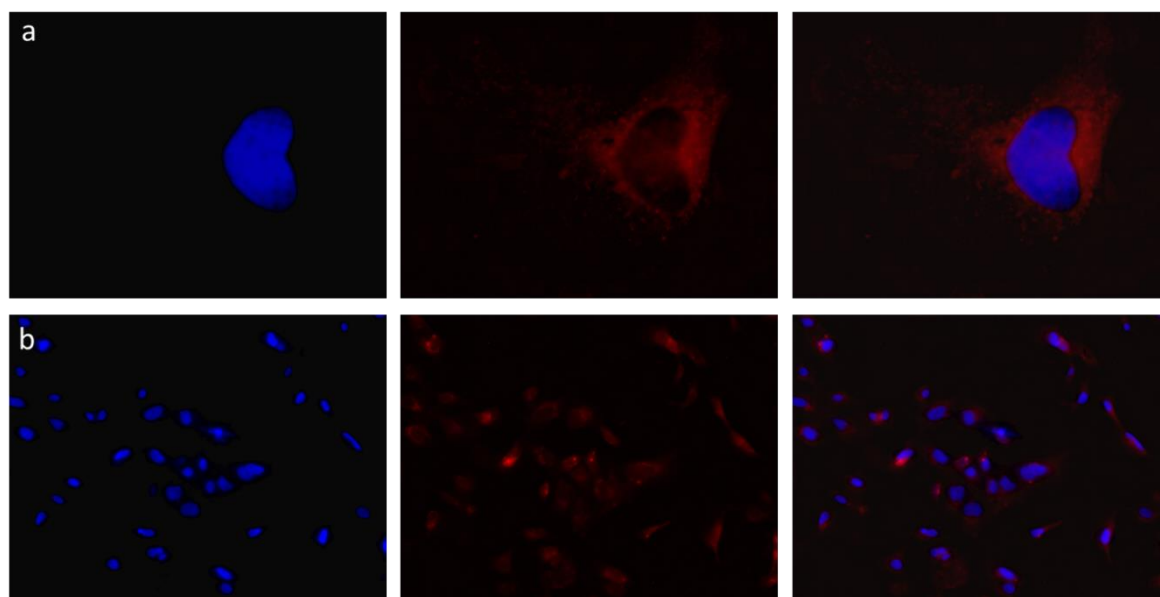
Figure 39. Bioimaging of Nthy-ori3-1 cells treated with **Cmr-Cz** (1µM) coumarin. a) (20X) and b) (100X) fluorescent images of Nthy-ori3-1 cells stained with DAPI (blue), **Cmr-Cz** (1µM) orange (excitation 530-550 nm; emission 575), overlap between **Cmr-Cz** images and DAPI.

3.7 conclusions

The synthesis of new coumarins **Cmr-Cz**, **Cmr-Pxz** and **Cmr-Ptz** was successfully performed using a two-step strategy affording these derivatives in satisfactory yields. The photophysical characterization showed that only the **Cmr-Cz** coumarin has TADF properties and presents a good quantum efficiency (in chloroform solution it has a PLQY of about 37%) while the other two **Cmr-Pox** and **Cmr-Pxz** showed a poor quantum efficiency and emission in the orange-red range. Furthermore, preliminary in vitro biological studies for the **Cmr-Cz** molecule showed low toxicity and it was therefore investigated

as a potential use as high-resolution bio-imaging intracellular TADF dye. These investigations are ongoing in order to identify specific affinity with cytoplasmic subunits by using time dependent high-resolution confocal microscopy.

3.8 references

57.	Yan, L. Q., Kong, Z. N., Xia, Y. & Qi, Z. J. A novel coumarin-based red fluoro-gen with AIE, self-assembly, and TADF properties. *New J. Chem.* **40**, 7061–7067 (2016).

58.	Chen, J.-X. *et al.* Coumarin-Based Thermally Activated Delayed Fluores-cence Emitters with High External Quantum Efficiency and Low Efficiency Roll-off in the Devices. *ACS Appl. Mater. Interfaces* **9**, 8848–8854 (2017).

59.	Ke, K. *et al.* Improving performance of thermally activated delayed fluores-cence emitter by extending its LUMO distribution. *Sci. China Mater.* **62**, 719–728 (2019).

60.	Moral, M., Muccioli, L., Son, W.-J., Olivier, Y. & Sancho-García, J. C. Theo-retical Rationalization of the Singlet–Triplet Gap in OLEDs Materials: Impact of Charge-Transfer Character. *J. Chem. Theory Comput.* **11**, 168–177 (2015).

61.	Kumar, S., Puttaraju, B. & Patil, S. A Deep-Blue Electroluminescent Device Based on a Coumarin Derivative. *ChemPlusChem* **81**, 384–390 (2016).

Chapter 4: Synthesis of deep blue emitting new spiro [fluorene-9,9′-xanthene]

4.1 Introduction

OLEDs are considered the most competitive candidates for next-generation color flat panel displays and future energy-saving lighting sources due to their unique characteristics.[62-63] For the manufacture of both flat panel and light sources, multicolored luminescent materials are generally needed to ensure the quality of devices, because a flat panel display should possess the ability to produce nearly all real-world colors, and white light generated by solid-state light sources should show an index high enough color rendering (CRI) (≥80) to reproduce the vivid color of illuminated objects.[64-65] So, to fulfil these purposes, three types of luminescent materials that emit primary colors Red (R), Green (G) and Blue (B) are generally employed according to the theoretical primary color. However, luminescent materials with different emission colors can affect the quality of displays. Among primary color luminescent materials, both fluorescent (singlet) and phosphorescent (triplet) type blue emitters generally exhibit significantly lower electroluminescence (EL) performance in terms of efficiency, durability, color quality and injection / transport.[66-67] Therefore, the speed with which OLEDs are introduced to the market has been slow. Getting a good compromise between the necessary properties required by the OLED field is indeed a great challenge for researchers. According to industry standards for color displays, materials that emit blue should emit a saturated blue or deep blue color to meet the demand for high-quality displays. This indicates that the blue emitters should have a very wide band gap (E_g), making it difficult to design their molecular structure. The chemical characteristics required to meet the deep blue emission can induce stability and charge carrier injection / transport problems in the devices. The blue phosphorescent emitters showed high EL efficiency; however, they

still have similar disadvantages with their fluorescent counterparts. In addition, they show more serious problems related to color purity. To date, there are few blue phosphorescent emitters and most of them emit only sky-blue phosphorescence, which cannot meet the requirements of the display standard, and deep blue phosphorescent emitters are rare.[68-69]

To date, several studies have examined blue emitters as polymers,[70] small fluorescent emitters,[71] and small phosphorescent organometallic complexes.[,72] The luminescent materials introduced by these reviews usually show sky blue or blue emissions with the y component of the Commission Internationale de l'Eclairage (CIE) coordinates greater than 0.1. However, considering the application of OLEDs in color displays, the CIE coordinates of the blue EL should be (0.14, 0.08) as specified in the National Television System Committee (NTSC) standard or (0.15, 0,06) by the European Broadcast Union (EBU) television viewing criterion. As a result, blue luminescent materials showing CIE coordinates with a y component of less than 0.1 are highly desired.
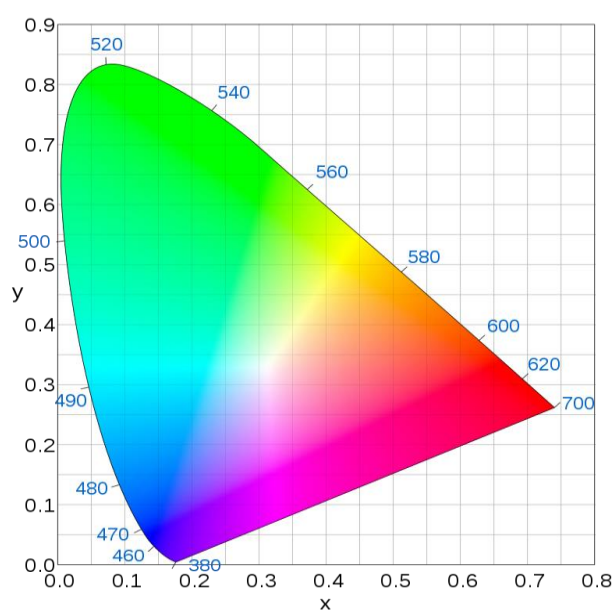
Figure 40. The CIE (Commission Internationale de l'Eclairage) 1931 chromaticity diagram.

In a sense, the development of blue emitters can largely determine the progress of organic EL, considering the practical applications of OLEDs.

In view of the impending global energy crisis and inefficient use of energy, the energy-saving function associated with OLEDs could show their most attractive feature as one of the most competitive candidates for next-generation displays and especially future ones, energy-saving lighting sources. Therefore, being the most fundamental component in OLEDs, light-emitting materials are absolutely necessary to show high EL efficiencies, i.e. convert electricity into light more efficiently. Unfortunately, deep blue emitting materials still exhibit relatively low EL efficiencies compared to other analogs such as green emitting ones.[73-74] Hence, the development of highly efficient blue emitting materials is still a great challenge, especially to obtain efficient deep-blue emitters, which are very critical for making high quality displays.

Another challenge in finding materials that emit deep blue is stability. To obtain a deep blue emission, the emitters should have a sufficiently large band-gap. Therefore, the excited states of the deep blue emitters possess very high energy levels, which increase the susceptibility to deterioration of the deep blue emitters upon excitation. In another aspect, the blue phosphorescent emitters also suffer from stability problems. In order to obtain high triplet energy and induce blue phosphorescence, strong electron attracting groups, such as fluoride and cyanide, are introduced into the blue phosphorescent emitters. However, C − F bonds in blue phosphorescent emitters have been shown to be prone to decompose during operation of their corresponding OLEDs.[75] As a result, blue OLEDs generally exhibit a shorter lifespan than their green and red analogs. Therefore, improving the stability of materials that emit deep blue is a very important issue in the field of OLEDs.

While aiming at designing deep blue TADF emitters, several parameters should be taken under consideration, such as the π-conjugation length, the redox potential of both the electron-releasing and electron-withdrawing moieties, as well as the degree of conjugation, which is allowed between the two moieties. In practice, the photophysical characteristics as well as the geometry of the molecules are now classically examined by theoretical calculations prior to their synthesis, optimizing the probability to get materials with the desired properties. However, the design and synthesis of a light-emitting material with TADF properties is not enough to be sure that OLEDs that will be fabricated will furnish a deep blue OLED. Indeed, choice of an adapted host, selection of the right device stacking, the dopant concentration is another crucial parameter governing the performance of OLEDs.[76]

The following are the best performing TADF molecules used in the literature for the production of OLEDs that place in the deep blue region (figure 41).[77-87]

3,6-DtBuCz-AD
λ_{EL} = 450 nm
EQE$_{max}$ = 14,7%

tPBisICz
λ_{EL} = 452 nm
EQE$_{max}$ = 23,1%

4PCz-DPS
λ_{EL} = 430 nm
EQE$_{max}$ = 23,3%

(S)-NPE-AcDPS
λ_{EL} = 458 nm
EQE$_{max}$ = 18,5%

3tPAB
λ_{EL} = 460 nm
EQE$_{max}$ = 19,3%

OBOtSAc
λ_{EL} = 471 nm
EQE$_{max}$ = 20,7%

OBOtSAc
λ_{EL} = 452 nm
EQE$_{max}$ = 31,2%

tCz-ND
λ_{EL} = 459 nm
EQE$_{max}$ = 17,0%

DCzBN4
λ_{EL} = 468 nm
EQE$_{max}$ = 18,0%

Cz-TRZ3
λ_{EL} = 450 nm
EQE$_{max}$ = 19,2%

DBA-SAB
λ_{EL} = 472 nm
EQE$_{max}$ = 25,7%

34TCzPN
λ_{EL} = 475 nm
EQE$_{max}$ = 21,8%

DABNA-2
λ_{EL} = 467 nm
EQE$_{max}$ = 20,2%

TTAZ
λ_{EL} = 464 nm
EQE$_{max}$ = 23,7%

Figure 41. Molecular structure, maximum electroluminescence and EQE$_{max}$ of some TADF emitters known in literature.

4.1.1 Spiro compounds

Aromatic spiro compounds represent a class of molecules characterized by high PLQY, non-dispersive hole transport capacity and ambipolar carrier transporting properties. Due to these properties, a variety of spiro-derivatives have been investigated in different fields, finding applications in molecular tectonics,[88] enantioselective molecular recognition,[89] molecular electronics,[90] and optoelectronic devices preparation.[91-92] Spiro compounds also possess other interesting properties which are of great importance for the fabrication of optoelectronic devices such as high solubility and thermal stability. In this scenario, the spirobifluorene (SBF) which, being rigid, bulky and three-dimensional, lends itself perfectly as a component for the construction of deep blue emitting materials.[93-95] SBF and its derivatives have also been reported in literature as functional materials for large optical band gap.[96]

In 2006 Huang and co-workers developed a new synthetic one-pot route for the preparation of spiro [fluorene-9,9′-xanthene] (SFX).[97] Due to its interesting optoelectronic and physical properties, SFX and its synthetic strategy has been used to study a series of luminescent materials with high thermal stability, solubility in various solvents steric hindrance etc.

This strategy was also employed by Yam and co-workers which synthesized a number of spiro fluorene-xanthene scaffolds which were investigated as hole transporters.[98]

Moreover, the Liang group synthesized and applied two SFX-substituted tetracarbazole-based hole transport materials (SFX-Cr1 and SFX-Cr2) for the preparation of OLEDs. It has been shown that controlling the substituted positions of carbazole in SFX it is possible to modulate changes on their photophysical and electrochemical properties, while improving the hole mobility (figure 42).[99]

Berlinguette and co-workers, reported the synthesis, the characterization and the application of new fluorine-xanthene spiro derivatives as hole-transport materials (HTM) and their application in the design of solar cells (Figure 42). It was determined that the introduction of TPA groups in the fluorene skeleton increased the free energy variation for hole extraction from the perovskite layer, while the TPAs on the xanthene unit govern the glass transition temperature (Tg) values.[100]

Huang synthesized a new spiro, 2,30,60,7-tetracarbonitrile-SFX (TCNSFX) which was used as an electron acceptor upon the combination with tris (4-carbazoyl-9-ylphenyl) amine (TCTA) that acts as an electron donor to form an exciplex emitter. This TADF Exciplex showed a photoluminescence quantum yield of 29% and high electroluminescence efficiency (figure 42).[101]

The same research group, in 2021 synthesized two new acceptors based on spiro [fluorene-9,9′-xanthene] (SFX), 2-(4,6-diphenyl-1,3,5-triazin-2-yl)-SFX (TRZSFX) and 2,7-bis(4,6-diphenyl-1,3,5-triazin-2-yl)-SFX (DTRZSFX) obtaining exciplex emitters by using tris (4-carbazoyl-9-ylphenyl) amine (TCTA) as a donor. The results of these investigations showed that two TCTA-based devices: TRZSFX and TCTA: DTRZSFX hare characterized by high electroluminescence efficiency with an external quantum efficiency (EQE) value of 22%.[102]

Zhao and collaborators successfully synthesized two SFX coumarin derivatives, named SFX-CS and SFX-CD, their optoelectronic properties were studied and an OLED prototype was also fabricated. However, devices based on these two derivatives have been found to exhibit low efficiencies.[103]
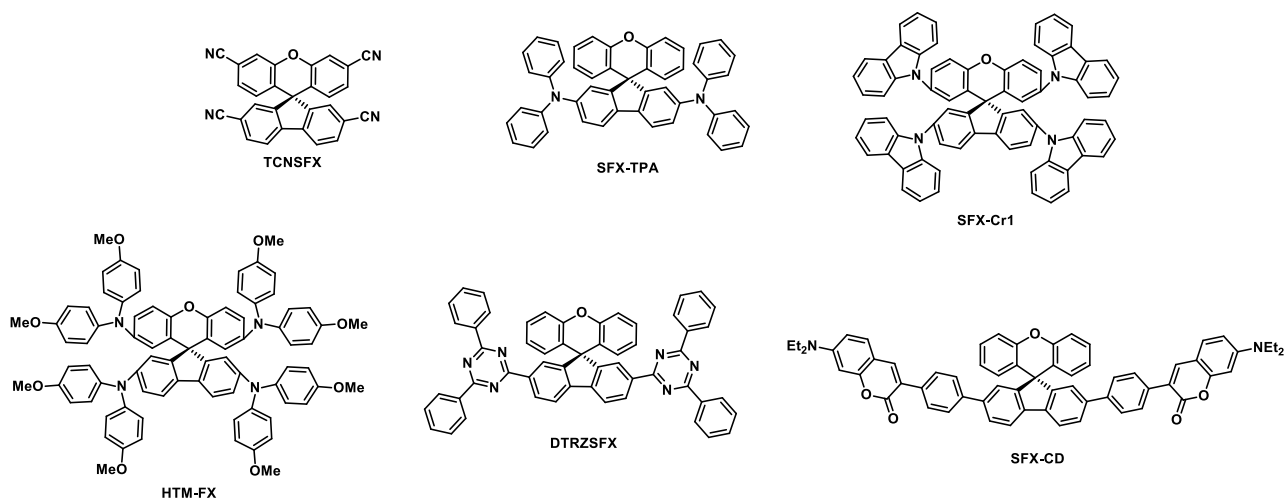
Figure 42. Representative molecular structures of synthetized Spiro (fluorene-xanthene).

Finally in 2021, Zysman-Colman and co-workers successfully synthesized the first examples of spiro fluorene-xanthene-based TADF emitters, called SFX-PO-DPA, SFX-PO-DPA-Me and SFX-PO-DPA-OMe. These compounds showed extremely interesting photophysical properties and the resulting OLED prototypes showed EQE values up to 23%, and modest efficiency roll-off.[104]
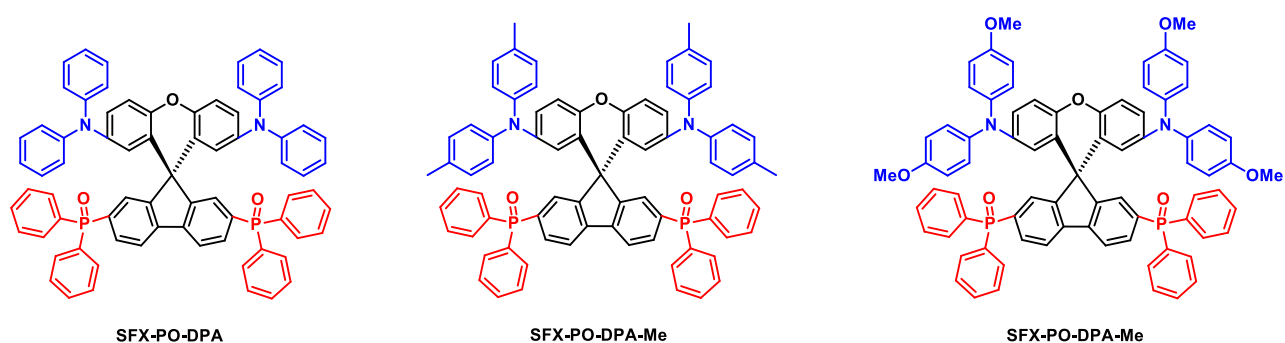
Figure 43. Chemical structures of TADF spiro fluorene-xanthene based compounds.

As a continuation of this study, we investigated some spiro (fluorene-9.9 '-xanthene) **SFX-CN-Cz** and **SFX-CN-tBuCz** systems with the aim to develop a series of performing deep blue emitters.

In this project, cyanobenzene decorated fluorene was introduced in these structures as the acceptor unit and two different substituted carbazoles, were introduced as donors (Figure 44).
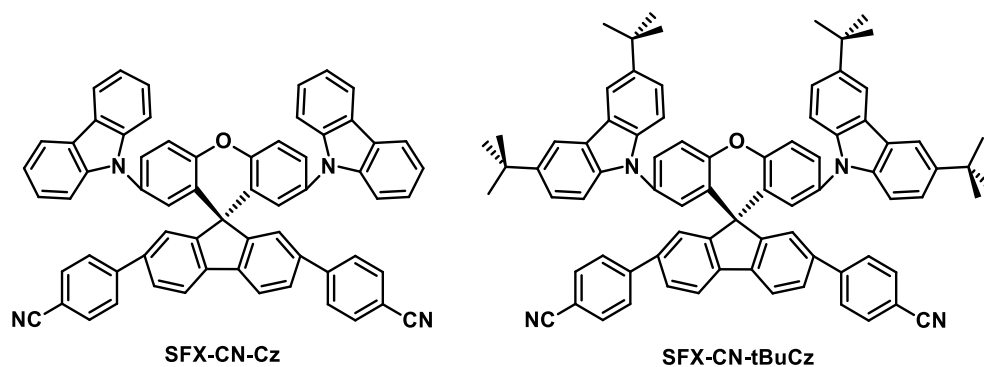
Figure 44. Chemical structures of **SFX-CN-Cz** and **SFX-CN-tBuCz**.

4.2 Results and Discussion

4.2.1 Synthesis

These compounds were prepared starting from 2,7-dibromospiro[fluorene-9,9'-xanthene] **SFX-Br** which was prepared following the corresponding literature.[95] Then the compound 4,4'-(spiro[fluorene-9,9'-xanthene]-2,7-diyl)dibenzonitrile **SFX-CN** was synthesized through a Suzuki cross-coupling reaction catalyzed by Pd(PPh$_3$)$_4$. The so obtained molecular structure **SFX-CN** was selectively diiodinated by using a *N*-iodosuccinimide (NIS) in Chloroform and Trifluoroacetic acid at 50 °C affording the corresponding diiodo adduct in a good yield (80%). Finally, Pd(0)-catalyzed Buchwald-Hartwig coupling (Pd2(dba)3, [(t-Bu)3PH]BF4, NaOt-Bu, toluene at 110 °C, 48 hours)

with different carbazole derivatives afforded the desired compound with moderate yields

for **SFX-CN-Cz** 35% and **SFX-CN-tBuCz** 38% respectively.
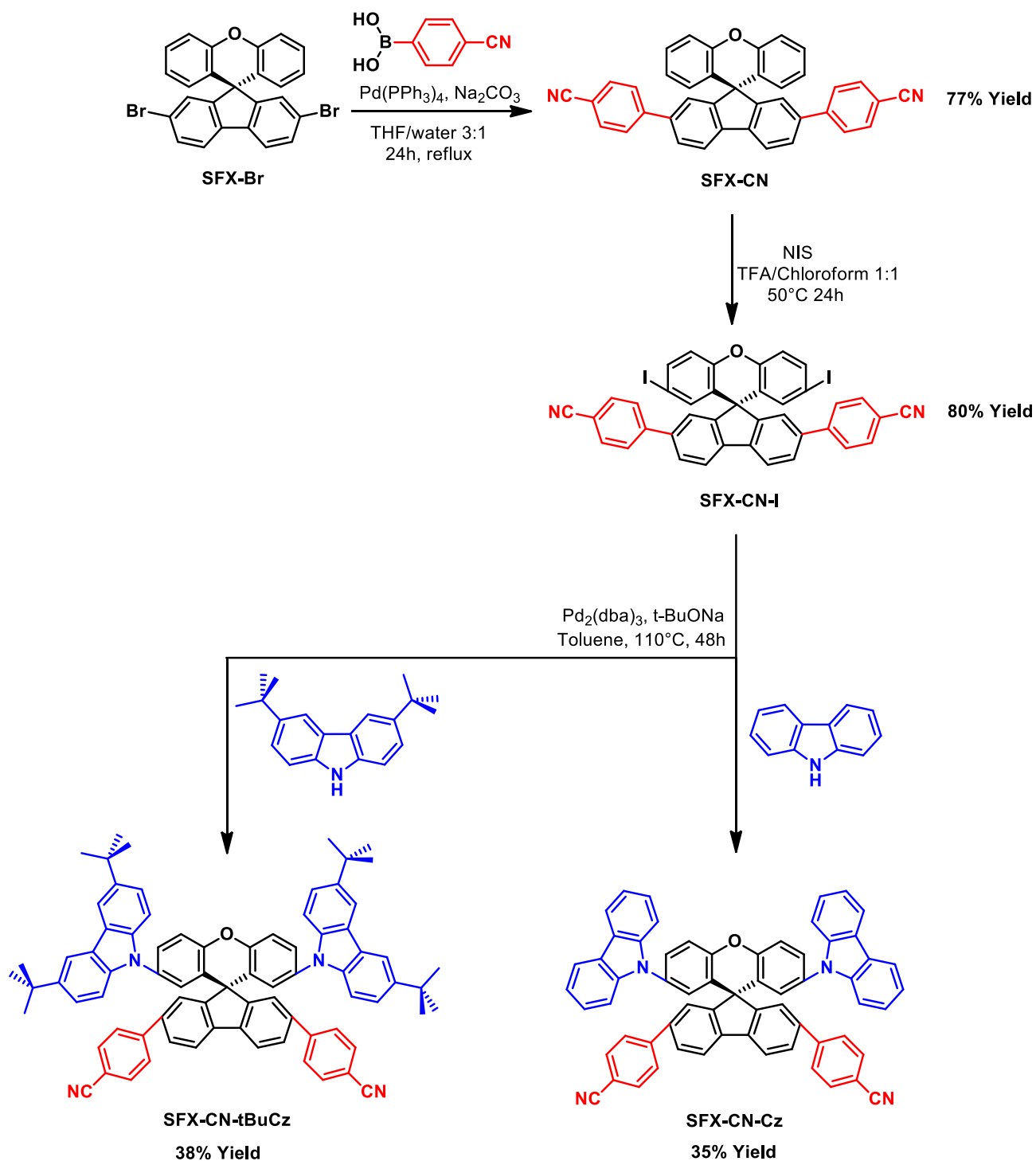
Scheme 6. Synthetic routes for **SFX-CN-Cz** and **SFX-CN-tBuCz**.

4.2.2 Crystal Structures

The structures of **SFX-CN-Cz** and **SFX-CN-tBuCz** were studied by single crystal X-ray diffraction (Figures 45 and 46). The data obtained from the X-ray diffraction analysis are summarized in Table 10. **SFX-CN-Cz** formed colorless crystals and was found to crystallize in the triclinic space group P-1 when recrystallized from a mixture of tetrahydrofuran and hexane by slow evaporation of the solvent. **SFX-CN-tBuCz** formed colorless crystals in the monoclinic space group P2$_1$/n when recrystallized from a mixture of tetrahydrofuran and hexane by slow evaporation of the solvent. The **SFX-CN-Cz** molecule has a dihedral angle of approximately 154°. While the molecule **SFX-CN-tBuCz** has a dihedral angle of about 146°. Both molecules **SFX-CN-Cz** and **SFX-CN-tBuCz** exhibit no intermolecular π-π stacking.
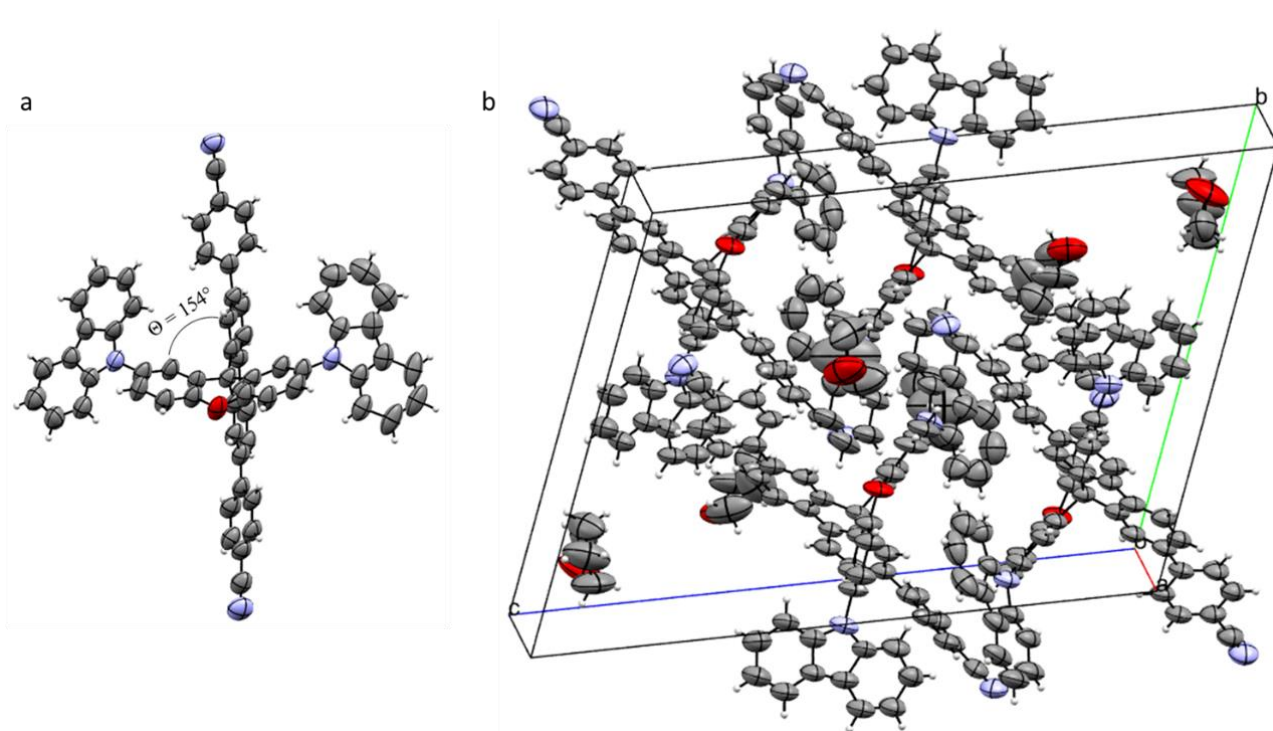
Figure 45. a) ORTEP diagram with 50% probability. b) Solid-state packing of **SFX-CN-Cz**. Heteroatoms: O, red; N, blue.
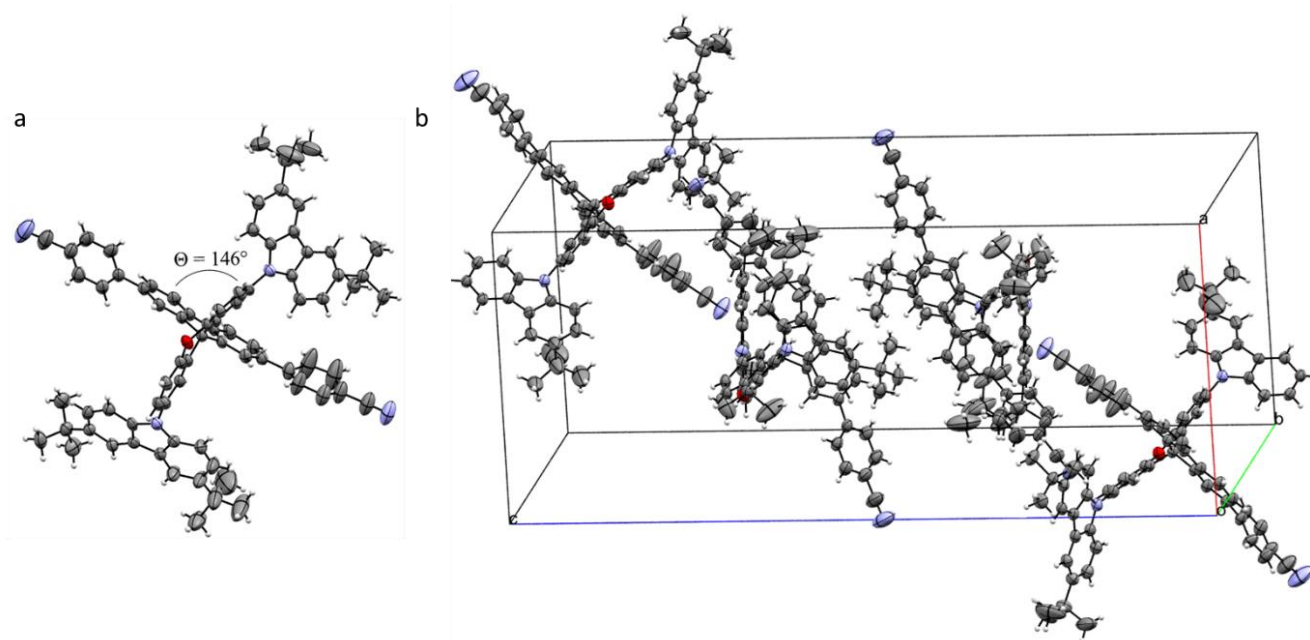
Figure 46. a) ORTEP diagram with 50% probability. b) Solid-state packing of **SFX-CN-tBuCz**. Heteroatoms: O, red; N, blue.

Table 10. Summary of X-ray crystallographic data for **SFX-CN-Cz** and **SFX-CN-tBuCz**.

	SFX-CN-Cz	SFX-CN-tBuCz
Chemical formula	$2(C_{63}H_{36}N_4 O),3(C_4H_8O)$	$C_{79} H_{68} N_4 O$
Formula weight	864,99	1089,41
Space group	P -1	P 2_1/n
a (Å)	14.4666(12)	17.8649(6)
b (Å)	18.3081(9)	10.0645(2)
c (Å)	25.0266(14)	40.3468(12)
α (°)	111.129(5)	90
β (°)	95.752(7)	97.801(3)
γ (°)	98.538(6)	90
V (Å³)	6028.78	7187.27
Z	2	4
R-Factor (%)	9.02	14.43

4.2.3 Computational Calculations

The characterization of the electronic structure and optoelectronic properties of the two spiro compounds was carried out with the aid of DFT calculations. In particular, the methodology described in chapter 5 which describes the experimental part was used. From the results obtained (shown in scheme 7) the HOMO level is lower when passing from **SFX-CN-Cz** to **SFX-CN-tBuCz**, this is consistent with the growing strength of the donor. As for the LUMO, this is localized on the whole part of the acceptor including benzonitrile and fluorene. The energies of S_1 decrease from 3.00 eV for **SFX-CN-Cz** to 2.81 eV for **SFX-CN-tBuCz**. The ΔE_{ST} values turn out to be quite small going from 0.14 eV for **SFX-CN-Cz** to 0.003 eV for **SFX-CN-tBuCz** reflect the almost orthogonal arrangement of the donor and acceptor groups, this could indicate that the two spiro could be TADF. The calculated oscillator strength is very small and range from 0 to 10^{-4} so a low fluorescence efficiency of these two emitters should be expected.
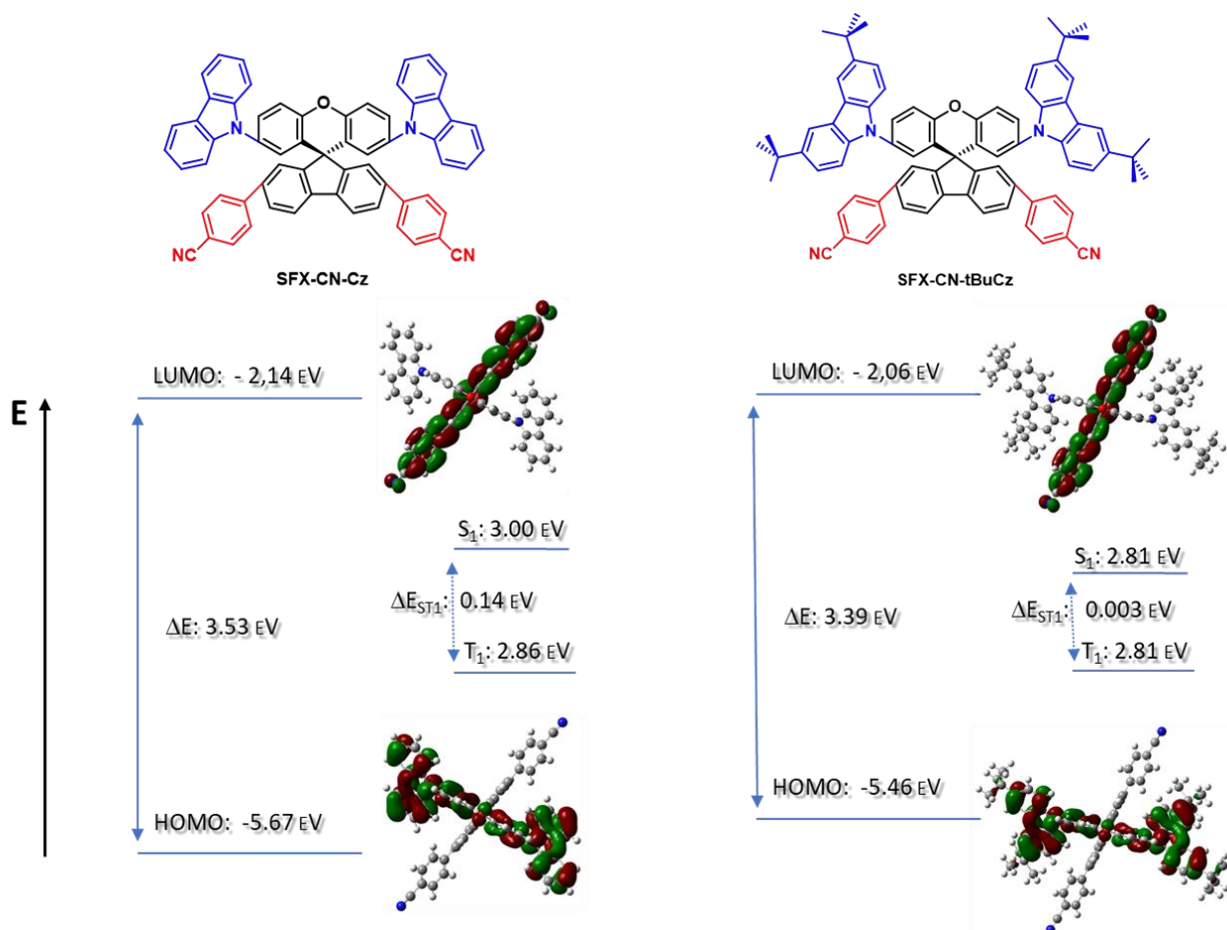
Scheme 7. Calculated HOMO and LUMO (as obtained at DFT PBE0 6-31G(d,p) level), S_1 and T_1 energies (as obtained at TDA-DFT PBE0 6-31G(d,p) level), of **SFX-CN-Cz** and **SFX-CN-tBuCz**.

4.2.4 Photophysical characterization

Figure 47 shows the absorption and photoluminescence (PL) spectra of the two emitters in different solvents. Both compounds exhibit similar optical absorption and possess a series of highly absorptive bands from 290 nm to 370 nm. The photoluminescence spectra show a red shift in the emission from **SFX-CN-Cz** (in toluene λ_{PL} = 423 nm) to **SFX-CN-tBuCz** (in toluene λ_{PL} = 445 nm) consistent with the decrease in the HOMO-

LUMO gap. This achievement was also corroborated by theoretical calculations. The Φ_{PL} values of 8% for **SFX-CN-Cz** and 6% for **SFX-CN-tBuCz** in aerated toluene solution are quite low but in degassed toluene solution the Φ_{PL} values increases about five times for both compounds (Φ_{PL} = 32% for **SFX-CN-Cz** and Φ_{PL} = 20% for **SFX-CN-tBuCz**). The absorption and emission properties of compounds **SFX-CN-Cz** and **SFX-CN-tBuCz** are also reported in the table 11.
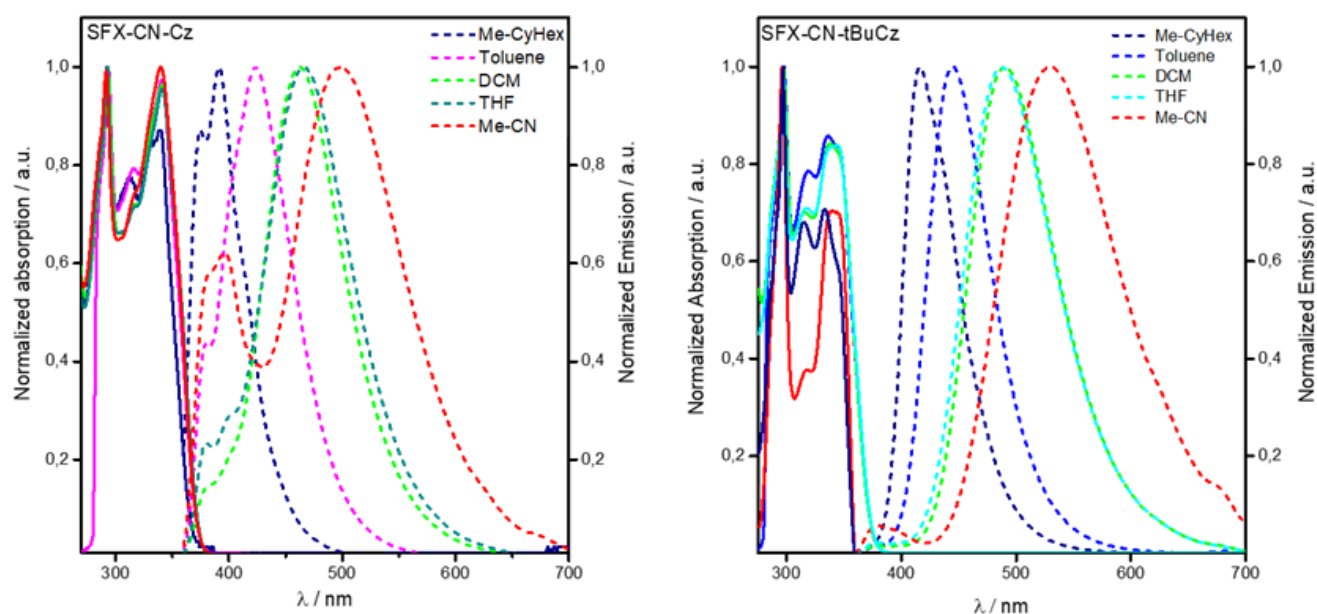
Figure **47**. Absorption and emission spectra in different solvent of **SFX-CN-Cz** and **SFX-CN-tBuCz**. λ_{exc} = 350 nm.

Table **11**. Emission maxima of **SFX-CN-Cz** and **SFX-CN-tBuCz** in methylcyclohexane, toluene, dichloromethane, tetrahydrofuran and acetonitrile. λ_{exc} = 350 nm.

Sample	λ_{PL} Me-CyHex (nm)	λ_{PL} Toluene (nm)	λ_{PL} DCM (nm)	λ_{PL} THF (nm)	λ_{PL} Me-CN (nm)
SFX-CN-Cz	390	423	462	466	498
SFX-CN-tBuCz	415	445	486	490	530

The photoluminescence behavior of the two solid-state spiro as doped films in different hosts was subsequently investigated.

With the idea to use these compounds for the development of deep blue OLEDs, it was essential to study their behavior physical properties once dispersed in solid host matrix.

A fundamental host requirement is the ability to generate complete confinement of singlet and triplet excitons created by charge recombination, thus avoiding the extinction of the triplet states due to the triplet-triplet energy transfer to the host and triplet-triplet annihilation. This requirement imposes a severe limitation on the choice of host materials for most blue emitters, for which the hosts must have triplet energies around 3.0 eV or higher. Another important aspect in the choice of a host is related to the strong CT character of the excited state in molecules of this type, which induces local interactions between the dipole moment of the excited state of the emitter and the dipole moment of the host. In solution, such interactions lead to the observation of the usual bathochromic spectral shift observed in CT molecules with increasing solvent polarity. However, a similar effect also occurs in the solid state when the emitters (in hosts matrix) are doped with relatively high polarity compounds, because these materials also stabilize the excited state CT due to local dipolar interactions, and therefore they tend to shift the emission peak to longer lengths. While in non-polar host molecules the emission peak is not strongly influenced.

For this reason, a hosts screening was done in order to measure the PLQY of the scattered emitters (figure 48). These results are summarized in table 12. For both the spiro-compounds **SFX-CN-tBuCz** and **SFX-CN-Cz,** the highest PLQY values were obtained by using mCP as host, reaching values from 31% to 42% respectively.
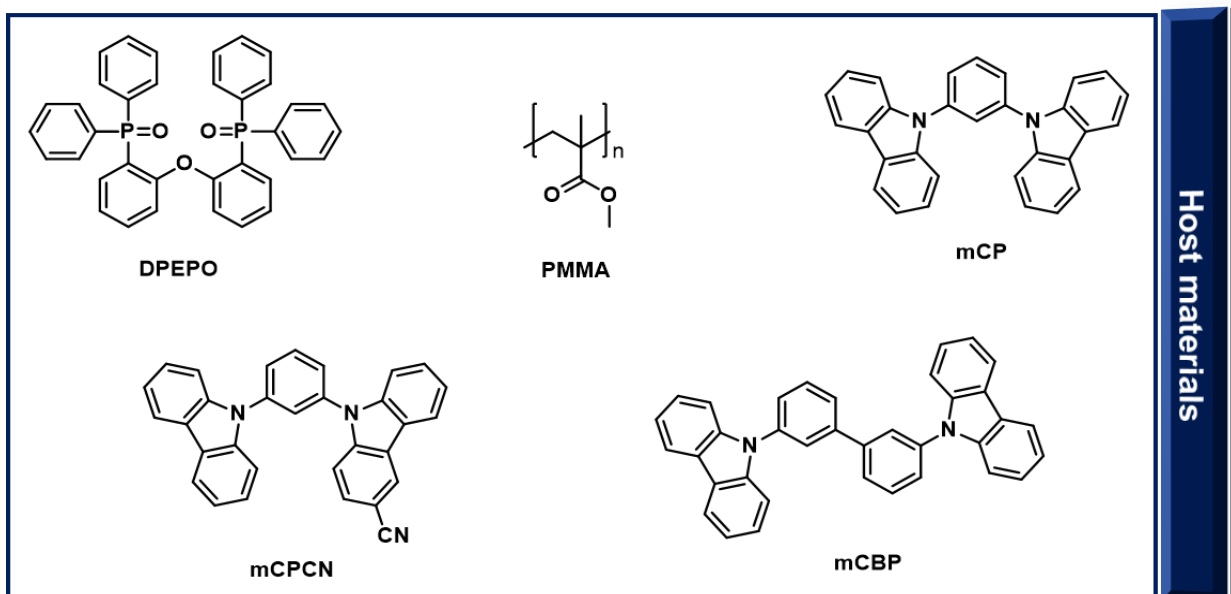
Figure 48. Molecular structures of screened organic host materials.

	SFX-CN-Cz			SFX-CN-tBuCz	

Conditions	Φ_{PL} % in O_2	Φ_{PL} % in N_2	Conditions	Φ_{PL} % in O_2	Φ_{PL} % in N_2
15 wt% in DPEPO	15.2	16.9	15 wt% in DPEPO	8.6	12.4
10 wt% in mCPCN	32.8	33.3	3 wt% in mCPCN	22.2	23.2
20 wt% in mCP	**41.7**	**42.3**	**15 wt% in mCP**	**31.1**	**30.2**
20 wt% in mCBP	24.1	25.4	15 wt% in mCBP	19.8	21.2
10 wt% in PMMA	23.8	24.6	10 wt% in PMMA	11.6	12.4
Neat Film	17.7	23.9	Neat Film	13.2	16.5

Table 12. PLQY values measured under air or under nitrogen for **SFX-CN-tBuCz** and **SFX-CN-Cz** emitters.

Neat and mCP films were further investigated through photoluminescence and lifetime measurements. As reported in figure 49, the emission profiles of **SFX-CN-tBuCz** and **SFX-CN-Cz** emitters remained broad and unstructured. On the other hand, analyses conducted in mCP films, showed a deep blue emission with λ_{PL} of 415 nm for **SFX-CN-**

Cz and 428 nm for **SFX-CN-tBuCz**, which are quite similar to those observed in solution (toluene).
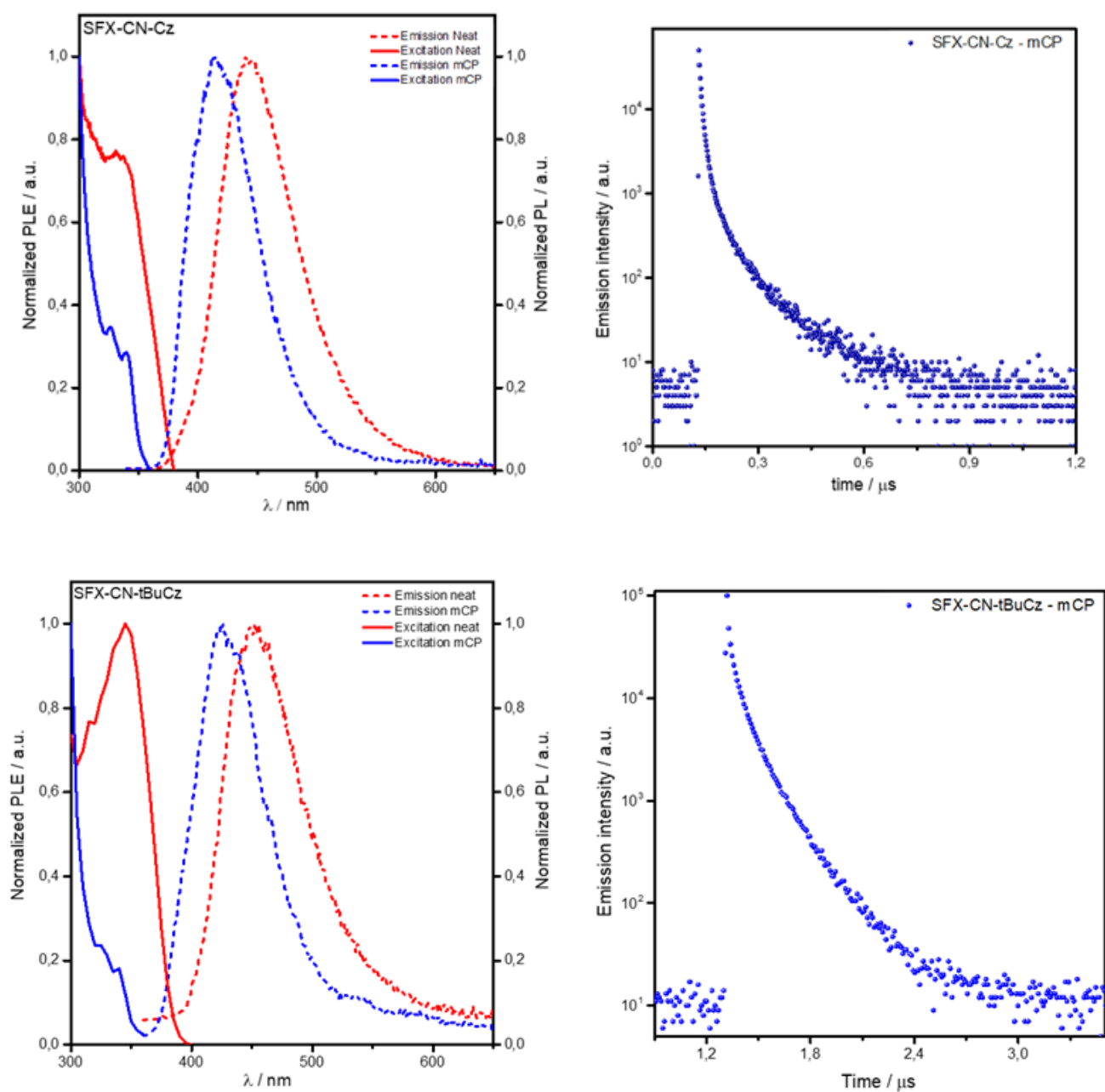
Figure 49. Excitation and photoluminescence spectra neat and mCP film (left). Decay time plot of **SFX-CN-tBuCz** and **SFX-CN-Cz** emitters in mCP film (right).

Nevertheless, time-resolved photoluminescence measurements in mCP revealed tri-exponential decay profiles for both emitters. **SFX-CN-Cz**, **SFX-CN-tBuCz** had prompt lifetimes and no delayed lifetimes were detected. These data are sumarized in Table 13.

Table 13. Values of the maximum emission and lifetimes of the two spiro in mCP film.

SFX-CN-Cz			SFX-CN-tBuCz		
Conditions	λ_{PL} (nm)	τ_{PL}	Conditions	λ_{PL} (nm)	τ_{PL}
20 wt% in mCP	415	τ_{p1} = 7 ns (57%) τ_{p2} = 28 ns (30%) τ_{p3} = 117 ns (12%)	15 wt% in mCP	428	τ_{p1} = 23 ns (21%) τ_{p2} = 92 ns (58%) τ_{p3} = 218 ns (21%)

4.2.5 Electrochemical Properties

The HOMO and LUMO energy levels of the two spiro molecules were deduced from an analysis of the measurements of cyclic voltammetry (CV) and differential pulse voltammetry (DPV) obtained in dichloromethane. The CVs and DPVs are shown in Figure 50 and the data are summarized in Table 14.
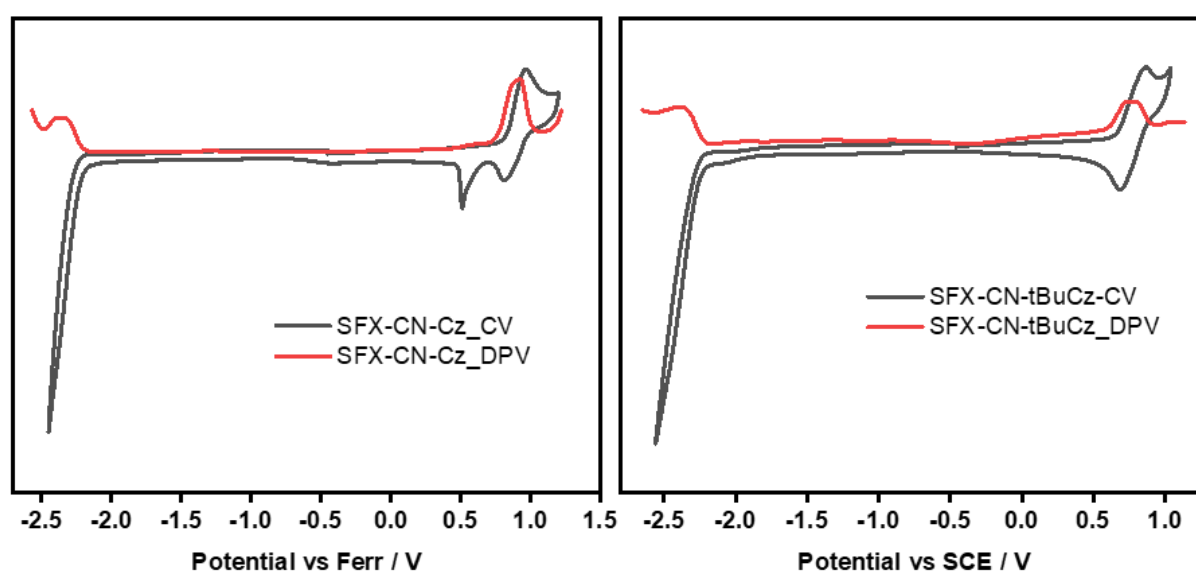
Figure 50. CV and DPV in degassed CH_2Cl_2 with 0.1 m [$^nBu_4N$]PF_6 as the supporting electrolyte and Fc/Fc⁺ as the internal reference (calibrated vs the Fc/Fc⁺ redox couple).

Compound	1rst $E_{1/2\,ox}$ (V)[e]	$E_{1/2\,red}$ (V)[e]	HOMO (eV)[f]	LUMO (eV)[g]	E_{gap} (eV)[h]
SFX-CN-Cz	0.90	-2.36	-5.70	-2.44	3.26
SFX-CN-tBuCz	0.76	-2.36	-5.56	-2.44	3.12

[e] Measured in dichloromethane and calibrated versus the ferrocene/ferrocenium (Fc/Fc⁺) redox couple.
[f] Calculated using the formula $HOMO = -[Eox + 4.8]\ eV$.
[g] Calculated using the formula $LUMO = -[Ered + 4.8]\ eV$.
[h] Calculated using the formula $Egap = |HOMO - LUMO|\ eV$.

Table 14. Electrochemical properties of **SFX-CN-Cz** and **SFX-CN-tBuCz**.

A redox wave was observed for the **SFX-CN-Cz** emitter only after the first oxidation event occurred. We attributed this result to the formation of polymeric structures involving the positions 3 and 6 of the carbazole moiety upon oxidation. This polymer is formed immediately after the first oxidation event. This process is quite common for unsubstituted carbazoles and the phenomenon has been sufficiently reported in the literature.[105] After the first oxidation step, this peak gets bigger and bigger after each oxidation cycle, indicating that the amount of polymeric form is increasing on the electrode surface. This process is also depicted in figure 51. On the other hand, **SFX-CN-tBuCz** compound did not show this peak since the 3 and 6 positions are protected with tertbutyl groups.

.
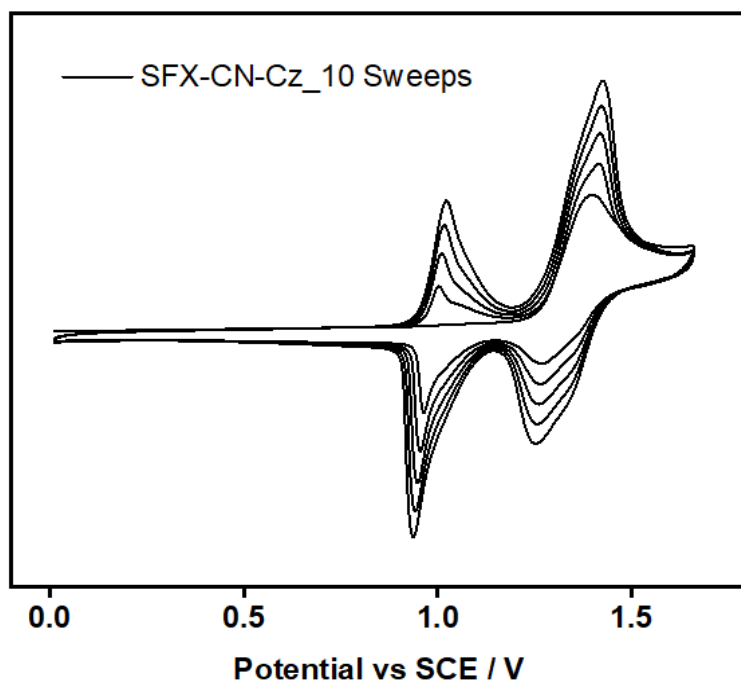
Figure 51. 10 sweeps of cyclic voltammetry of **SFX-CN-Cz**.

4.2.6 Thermal properties

Decomposition temperature (T_d) is defined as the temperature at which 5% weight loss occurs during heating. Spiro compounds are generally characterized by a high T_d, several spiro compounds have been reported in literature having Td higher than 500°C. Figures 52 and 53 show the thermogravimetric curves of the two synthesized spiro, they have a high thermal stability. These two emitters in fact have a T_d ranging from 506 to 510°C for **SFX-CN-Cz** and **SFX-CN-tBuCz** respectively, similar results were also found in other spiro derivatives known in the literature.[106]
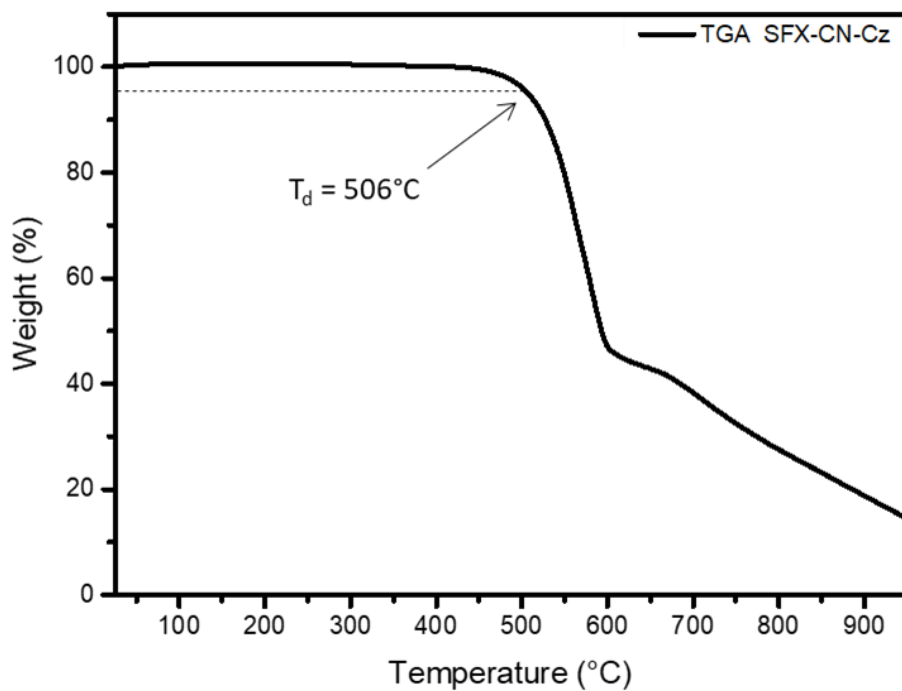
Figure 52. SFX-CN-Cz thermogram.
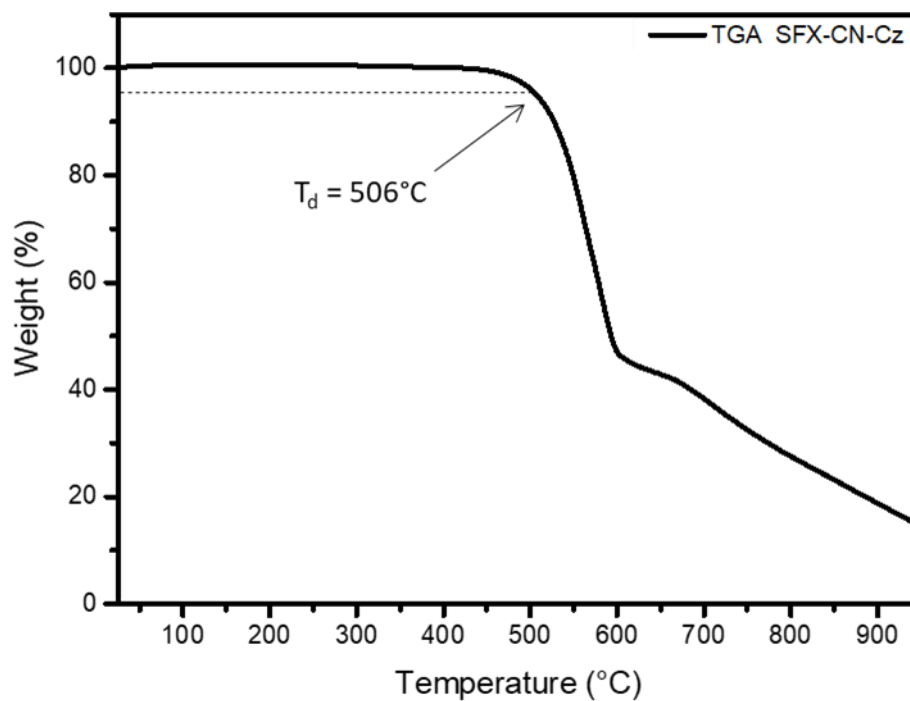
Figura 53. SFX-CN-tBuCz thermogram.

4.3 Conclusions

We successfully synthesized two fluorene-xanthene (SFX)-based spiro-derivatives in four steps with a final yield of approximately 22%. These two spiro derivatives exhibit several desirable photophysical properties. In fact, both **SFX-CN-Cz** and **SFX-CN-tBuCz** emit in the deep-blue region and have PLQY values of 42 and 31% respectively (in mCP films). Furthermore, both molecules have a high thermal stability showing high decomposition temperature > 500°C.

Further studies are undergoing in order to understand their TADF properties and finally, test these molecular structures in OLED-prototypes to value their electroluminescence performance.

4.4 References

62. Schwartz, G., Reineke, S., Rosenow, T. C., Walzer, K. & Leo, K. Triplet Harvesting in Hybrid White Organic Light-Emitting Diodes. *Adv. Funct. Mater.* **19**, 1319–1333 (2009).

63. Kim, S. *et al.* Low-Power Flexible Organic Light-Emitting Diode Display Device. *Adv. Mater.* **23**, 3511–3516 (2011).

64. Farinola, G. M. & Ragni, R. Electroluminescent materials for white organic light emitting diodes. *Chem. Soc. Rev.* **40**, 3467 (2011).

65. Sasabe, H. & Kido, J. Multifunctional Materials in High-Performance OLEDs: Challenges for Solid-State Lighting. *Chem. Mater.* **23**, 621–630 (2011).

66. Lin, M.-S. *et al.* Incorporation of a CN group into mCP: a new bipolar host material for highly efficient blue and white electrophosphorescent devices. *J. Mater. Chem.* **22**, 16114 (2012).

67. Altinolcek, N. *et al.* Synthesis of novel multifunctional carbazole-based molecules and their thermal, electrochemical and optical properties. *Beilstein J. Org. Chem.* **16**, 1066–1074 (2020).

68. Yang, X., Zhou, G. & Wong, W.-Y. Functionalization of phosphorescent emitters and their host materials by main-group elements for phosphorescent organic light-emitting devices. *Chem. Soc. Rev.* **44**, 8484–8575 (2015).

69. Hung, W.-Y., Tu, G.-M., Chen, S.-W. & Chi, Y. Phenylcarbazole-dipyridyl triazole hybrid as bipolar host material for phosphorescent OLEDs. 9 (2012).

70. Yook, K. S. & Lee, J. Y. Organic Materials for Deep Blue Phosphorescent Organic Light-Emitting Diodes. *Adv. Mater.* **24**, 3169–3190 (2012).

71. Ho, C.-L. & Wong, W.-Y. Small-molecular blue phosphorescent dyes for organic light-emitting devices. *New J. Chem.* **37**, 1665 (2013).

72. Zhao, Q., Liu, S.-J. & Huang, W. Polyfluorene-Based Blue-Emitting Materials. *Macromol. Chem. Phys.* **210**, 1580–1590 (2009).

73. Ho, C.-L. & Wong, W.-Y. Small-molecular blue phosphorescent dyes for organic light-emitting devices. *New J. Chem.* **37**, 1665 (2013).

74. Bui, T.-T., Goubard, F., Ibrahim-Ouali, M., Gigmes, D. & Dumur, F. Thermally Activated Delayed Fluorescence Emitters for Deep Blue Organic Light Emitting Diodes: A Review of Recent Advances. *Applied Sciences* **8**, 494 (2018).

75. Bui, T.-T., Goubard, F., Ibrahim-Ouali, M., Gigmes, D. & Dumur, F. Recent advances on organic blue thermally activated delayed fluorescence (TADF) emitters for organic light-emitting diodes (OLEDs). *Beilstein J. Org. Chem.* **14**, 282–308 (2018).

76. Wu, S. *et al.* High-efficiency deep-blue organic light-emitting diodes based on a thermally activated delayed fluorescence emitter. *J. Mater. Chem. C* **2**, 421–424 (2014).

77. Woo, S.-J., Kim, Y., Kwon, S.-K., Kim, Y.-H. & Kim, J.-J. Phenazasiline/Spiroacridine Donor Combined with Methyl-Substituted Linkers for Efficient Deep Blue Thermally Activated Delayed Fluorescence Emitters. *ACS Appl. Mater. Interfaces* **11**, 7199–7207 (2019).

78. Chan, C., Cui, L., Kim, J. U., Nakanotani, H. & Adachi, C. Rational Molecular Design for Deep-Blue Thermally Activated Delayed Fluorescence Emitters. *Adv. Funct. Mater.* **28**, 1706023 (2018).

79. Hatakeyama, T. et al. Ultrapure Blue Thermally Activated Delayed Fluorescence Molecules: Efficient HOMO-LUMO Separation by the Multiple Resonance Effect. *Adv. Mater.* **28**, 2777–2781 (2016).

80. Lee, Y. & Hong, J. High-Efficiency Thermally Activated Delayed Fluorescence Emitters with High Horizontal Orientation and Narrow Deep-Blue Emission. *Adv.*

Optical Mater. **9**, 2100406 (2021).

81. Patil, V. V. et al. Purely Spin-Vibronic Coupling Assisted Triplet to Singlet Up-Conversion for Real Deep Blue Organic Light-Emitting Diodes with Over 20% Efficiency and y Color Coordinate of 0.05. *Adv. Sci.* **8**, 2101137 (2021).

82. Cui, L. et al. Controlling Singlet–Triplet Energy Splitting for Deep-Blue Thermally Activated Delayed Fluorescence Emitters. *Angew. Chem. Int. Ed.* **56**, 1571–1575 (2017).

83. Gudeika, D. et al. Tetraphenyl ornamented carbazolyl disubstituted diphenyl sulfone as bipolar TADF host for highly efficient OLEDs with low efficiency roll-offs. *Dyes and Pigments* **194**, 109573 (2021).

84. Huang, Z. et al. Chiral thermally activated delayed fluorescence emitters for circularly polarized luminescence and efficient deep blue OLEDs. *Dyes and Pigments* **197**, 109860 (2022).

85. Wang, Y. et al. A periphery cladding strategy to improve the performance of narrowband emitters, achieving deep-blue OLEDs with CIEy < 0.08 and external quantum efficiency approaching 20%. *Organic Electronics* **97**, 106275 (2021).

86. Mei, Y. et al. Acridin-9(10H)-one-based blue thermally activated delayed fluorescence materials: improvement of color purity and efficiency stability. *Materials Today Chemistry* **23**, 100645 (2022).

87. Kim, J. U. et al. Nanosecond-time-scale delayed fluorescence molecule for deep-blue OLEDs with small efficiency rolloff. *Nat Commun* **11**, 1765 (2020).

88. Ou, Q.-D. *et al.* Light outcoupling enhanced flexible organic light-emitting diodes. *Opt. Express* **24**, A674 (2016).

89. Schmidbauer, S., Hohenleutner, A. & König, B. Chemical Degradation in Organic

Light-Emitting Devices: Mechanisms and Implications for the Design of New Materials. *Adv. Mater.* **25**, 2114–2129 (2013).

90. Gather, M. C., Köhnen, A. & Meerholz, K. White Organic Light-Emitting Diodes. *Adv. Mater.* **23**, 233–248 (2011).

91. Chiang, C.-L., Shu, C.-F. & Chen, C.-T. Improved Synthesis of 2,2'-Dibromo-9,9'-spirobifluorene and Its 2,2'-Bisdonor-7,7'-bisacceptor-Substituted Fluorescent Derivatives. *Org. Lett.* **7**, 3717–3720 (2005).

92. Sauriat-Dorizon, H., Maris, T., Wuest, J. D. & Enright, G. D. Molecular Tectonics. Construction of Porous Hydrogen-Bonded Networks from Bisketals of Pentaerythritol. *J. Org. Chem.* **68**, 240–246 (2003).

93. Du, Y., Lu, X. & Yu, Y. Highly Regioselective Construction of Spirocycles via Phosphine-Catalyzed [3 + 2]-Cycloaddition. *J. Org. Chem.* **67**, 8901–8905 (2002).

94. Yu, W.-L., Pei, J., Huang, W. & Heeger, A. J. Spiro-Functionalized Polyfluorene Derivatives as Blue Light-Emitting Materials. 4.

95. Xie, L.-H. *et al.* Unexpected One-Pot Method to Synthesize Spiro[fluorene-9,9'-xanthene] Building Blocks for Blue-Light-Emitting Materials. *Org. Lett.* **8**, 2787–2790 (2006).

95. Wong, K.-T. *et al.* Ter(9,9-diarylfluorene)s: Highly Efficient Blue Emitter with Promising Electrochemical and Thermal Stability. *J. Am. Chem. Soc.* **124**, 11576–11577 (2002).

96. Saragi, T. P. I., Spehr, T., Siebert, A., Fuhrmann-Lieker, T. & Salbeck, J. Spiro Compounds for Organic Optoelectronics. *Chem. Rev.* **107**, 1011–1065 (2007).

97. Luo, J. *et al.* Three-Dimensional Architectures for Highly Stable Pure Blue Emission. *J. Am. Chem. Soc.* **129**, 11314–11315 (2007).

98. Chiang, C.-L. *et al.* Red-Emitting Fluorenes as Efficient Emitting Hosts for Non-Doped, Organic Red-Light-Emitting Diodes. *Adv. Funct. Mater.* **15**, 231–238

(2005).

99. Liang, X. *et al.* Tetra-carbazole substituted spiro[fluorene-9,9′-xanthene]-based hole-transporting materials with high thermal stability and mobility for efficient OLEDs. *Dyes and Pigments* **139**, 764–771 (2017).

100. Chiykowski, V. A. *et al.* Precise Control of Thermal and Redox Properties of Organic Hole-Transport Materials. *Angew. Chem. Int. Ed.* **57**, 15529–15533 (2018).

101. Cao, H.-T. *et al.* Tetracyano-substituted spiro[fluorene-9,9′-xanthene] as electron acceptor for exciplex thermally activated delayed fluorescence. *Journal of Molecular Structure* **1196**, 132–138 (2019).

102. Cao, H.-T. *et al.* Highly efficient exciplex-emission from spiro[fluorene-9,9′-xanthene] derivatives. *Dyes and Pigments* **185**, 108894 (2021).

103. Zhang, H., Liu, X., Gong, Y., Yu, T. & Zhao, Y. Synthesis and characterization of SFX-based coumarin derivatives for OLEDs. *Dyes and Pigments* **185**, 108969 (2021).

104. Sharma, N. *et al. Spiro-based thermally activated delayed fluorescence emitters with reduced non-radiative decay for high quantum efficiency, low roll-off, light-emitting diodes.* https://chemrxiv.org/engage/chemrxiv/article-details/60d5cefb461f56c2f248c02e (2021) doi:10.33774/chemrxiv-2021-b2m52.

105. Connelly, N. G. & Geiger, W. E. Chemical Redox Agents for Organometallic Chemistry. *Chem. Rev.* **96**, 877–910 (1996).

106. Saragi, T. P. I., Spehr, T., Siebert, A., Fuhrmann-Lieker, T. & Salbeck, J. Spiro Compounds for Organic Optoelectronics. *Chem. Rev.* **107**, 1011–1065 (2007).

Chapter 5: Experimental Section

5.1 General remarks

Commercially available reagents were purchased from Acros, Aldrich, Alfa-Aesar, TCI Europe and used as received. All reactions were monitored by thin-layer chromatography (TLC) performed on glass-backed silica gel 60 F254, 0.2 mm plates (Merck), and compounds were visualized under UV light (254 nm). ^1H and ^{13}C NMR spectra were recorded on a Varian 500 MHz and Bruker Avance III HD 600 MHz NMR spectrometer at 298 K and were calibrated using trimethylsylane (TMS). Proton chemical shifts are expressed in parts per million (ppm, δ scale) and are referred to the residual hydrogen in the solvent (CDCl$_3$, 7.27 ppm or DMSO-d$_6$ 2.54 ppm). Data are represented as follows: chemical shift, multiplicity (s = singlet, d = doublet, t = triplet, q = quartet, m = multiplet and/or multiple resonances, coupling constant (J) in Hertz (Hz). Carbon chemical shifts are expressed in parts per million (ppm, δ scale) and are referenced to the carbon resonances of the NMR solvent (CDCl$_3$, δ 77.0 ppm or δ DMSO-d6 δ 39.5 ppm). Deuterated NMR solvents were from Aldrich. High resolution mass spectra were recorded on a Thermofisher ESI-MS/MSORBITRAP-ELITE and Velos PRO. The sample solutions were infused directly into the ESI source using a programmable syringe pump at a flow rate of 5 μL/min. A PerkinElmer STA6000 instrument was used to carry out simultaneous TGA under a nitrogen flow of 60 mL min^{-1}. A total of 5 mg of each compound was placed in an alumina crucible, and measurements were performed in the temperature range of 30–800 °C (heating rate of 10 °C min^{-1}). Standard samples were used to calibrate the instrument (temperature accuracy of ±1 °C). Melting points were determined in an open capillary on a Büchi melting point apparatus and are uncorrected. All the experiments were carried out in duplicate to ensure reproducibility of the experimental data. Yields refer to pure isolated materials.

5.2 Computational methodology

All of the calculations were carried out using Gaussian 16 code. The energy calculations of the optimized structures were performed within density functional theory (DFT) with Becke's three parameters and the Lee–Yang–Parr's nonlocal correlation functional (B3LYP). The basis sets for C, N, O, and H were 6-311++G(d,p). Analysis of frequencies confirms that optimized structures are at a minimum of potential surface, and no imaginary frequencies were obtained. Excited singlet and triplet states were calculated by performing time dependent DFT (TD-DFT) calculations within the Tamm-Dancoff approximation based on the same functional and basis set in vacuum. The molecular orbitals were visualized using GaussView 6.0 software.[107-110]

5.3 Photophysical Characterization

Diluted optical solutions (10^{-5} or 10^{-6} M) were prepared in HPLC grade solvents for absorption and emission analysis. The absorption spectra of the molecules show the probability of absorption of a photon by a molecule and its variation with wavelength. The light intensity, which is a measure of the photon flux of photons in the optical beam, decreases through the sample as the photons are absorbed. There is a uniform probability of absorption throughout the sample, and the intensity reaching any distance *x* into the sample is given by the Beer-Lambert law. Absorption spectra were recorded at room temperature on a Varian Cary 60 spectrophotometer. After photoexcitation, molecules can emit light through a transition to the ground state (PL). By PL measurements, we radiative emission after the absorption of photons. The choice of the wavelength used to excite the sample is based on the analysis of the absorption spectrum. Steady-state emission spectra were recorded at 298 K using a Horiba Jobin Yvon Fluoromax 3.0 spectrofluorimeter. Samples were excited at 350 nm for steady-

state measurements. The quantum yield of photoluminescence (PLQY) is defined as the ratio of absorbed photons to emitted photons. PLQY in solutions were determined using optically dilute method previously reported in the litterature.[111] Their emission intensities were compared with appropriate references, Rhodamine 6G, whose quantum yield (Φ_r) in ethanol was determined to be 97% using the absolute method.[112] The quantum yield, Φ_{PL}, were determined by the equation $\Phi_{PL} = \Phi_r(A_r/A_s)((I_s/I_r)(n_s/n_r)^2$, where A stands for the absorbance at the excitation wavelength (λ_{exc} = 350 nm), I is the integrated area under the corrected emission curve and n is the refractive index of the solvent with the subscripts "s" and "r" representing sample and reference respectively. An integrating sphere was employed for quantum yield measurements for thin film samples.[113] Two types of solid-state samples were studied: a) spin coated films, b) drop casted films. For the fabrication of spin-coated films, solutions with different concentrations were dropped onto sapphire or quartz substrates. The substrate and solution were then keept at a controlled speed for a fixed time, with controlled acceleration up to the required spinning speed. Typical parameters are: Spinning Time = 60 seconds and speed = 500 rpm. This method results in uniform films. For drop-cast films, solutions with different concentrations were dropped onto substrates and left for a few hours under vacuum to dry. The Φ_{PL} of the films were then measured in air and by purging the integrating sphere with N_2 gas flow. Time-resolved PL measurements of the thin films were carried out using the time-correlated single-photon counting technique. The samples were excited at 370 nm by a pulsed laser diode (Picoquant, model PLS 370) and were kept in a vacuum of $< 10^{-4}$ mbar.

5.4 Electrochemical measurements

Cyclic voltammetry (CV) was used to identify the HOMO and LUMO energy levels of organic compounds. The energy of the LUMO can be approximated by the electron affinity, which is the energy required to add an electron to an atom or molecule in the gas phase. On the other hand, the energy of the HOMO is approximated by the minimum energy required to remove an electron from an atom or molecule. CV and differential pulse voltammetry (DPV) analyses were performed on an Electrochemical Analyzer potentiostat model 620D from CH Instruments. Samples were prepared as DCM solutions. Degassing was done by sparging with DCM-saturated nitrogen gas for 10 minutes prior to oxidation measurements and bubbling with nitrogen gas for 10 minutes prior to reduction measurements. All measurements were performed using 0.1 M tetra-n-butylammonium hexafluorophosphate, $[n\text{Bu}_4\text{N}]\text{PF}_6$, in DCM. An Ag/Ag$^+$ electrode was used as the reference electrode; a glassy carbon electrode was used as the working electrode and a platinum electrode was used as the counter electrode.

5.5 X-Ray crystallography

Single Crystal X-Ray Diffraction data for **Cmr-Cz** and **Cmr-Pxz** were collected at room temperature on a Bruker D8 Venture diffractometer equipped with a PHOTON II detector using APEX3[114] for data collection and processing. The structures were solved with ShelXT[115] 2018/2 and refined with ShelXL[116] 2018/3 using full matrix least squares min-imisation on F^2. Olex2[117] 1.3 was used as the graphical interface.

5.6 General Synthetic Procedures

The starting materials, Ethyl 6-bromo-2-oxo-2H-chromene-3-carboxylate, ethyl 6,8-di-bromo-2-oxo-2H-chromene-3-carboxylate and 6-bromo-2-oxo-2H-chromene-3-carbonitrile were prepared from the corresponding 2-hydroxybenzaldehydes and diethyl malonate (or malonitrile) in the presence of piperidone and acetic acid as described in the literature.[53-54]

Ethyl 7-bromo-2-oxo-2H-chromene-3-carboxylate 1l:
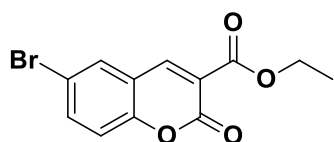
5-bromo-2-hydroxybenzaldehyde (0.049 mol), diethyl malonate (0.049 mol), piperidine (10 mol %) and acetic acid (4 drops) were dissolved in ethanol (200 mL) and stirred at 50°C for 16h. The reaction mixture was concentrated under vacuum and the obtained crude solid was crystallized in methanol yielding **1l** in 90% (13.0 g). Pale yellow crystals. Yield 90%. IR (KBr): v = 3006, 1734 cm-¹; M.p = 184-186°C; **¹H NMR** (500 MHz, CDCl₃) δ: 1.41 (t, 3H, J = 7.5 Hz), 4.42 (q, 2H, J = 7.5Hz), 7.27 (d, 1H, J = 9.0Hz), 7.73-7.78 (m, 2H), 8.42 (s, 1H); **¹³C NMR** (125 MHz, DMSO-d_6) δ: 20.2, 34.3, 109.4, 116.1, 118.3, 119.7, 131.8, 136.2, 146.6, 153.3, 163.6. **HRMS-ESI**: calcd for $C_{12}H_9BrNaO_4$ (318.9582), found (M-Na⁺), 318.9581).

Synthesis of 6-bromo-3-(methylsulfonyl)-2H-chromen-2-one 2l:
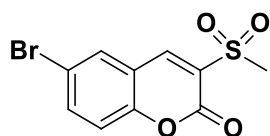
Piperidine (10 mol%) and CH₃COOH (4 drops) were added to a solution of 5-bromo-2-hydroxybenzaldehyde (4.0 g, 0.02 mol) and ethyl 2-(methylsulfonyl) acetate (3.32g, 0.02 mol) in EtOH (100mL). The mixture was stirred at 50°C for 16h and then concentrated under vacuum. The resulting crude solid was crystallized in hot MeOH yielding **2l** as a crystalline white solid. Yield 75% (4.50g). M.p. = 164-169°C. **¹H NMR** (600 MHz, CDCl₃) δ: 8.56 (s, 1H), 7.85 – 7.79 (m, 2H), 7.33

(d, J = 8.7 Hz, 1H), 3.34 (s, 3H); **13C NMR** (151 MHz, CDCl₃): δ = 155.38, 154.07, 146.21, 138.19, 132.36, 128.80, 118.88, 118.54, 118.28, 41.76. **HRMS-ESI**: calcd for $C_{10}H_7Br_1O_4S$ (324.9146), found (M-Na⁺, 324.9147).

6-bromo-2-oxo-2H-chromene-3-carbonitrile 3l:
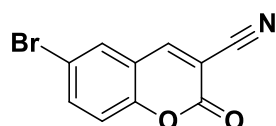
5-bromo-2-hydroxybenzaldehyde (0.040 mol), malononitrile (0.040 mol) and Na_2CO_3 (0.05 M in H_2O, 1.0 mL) were stirred at room temperature for 16h. HCl (1M, 100 mL) was added and the resulting yellow suspension was stirred at 80°C for 5 hours. Once cooled to room temperature, a yellow solid was isolated by filtration and washed twice with distilled H_2O (2x30 mL) and diethyl ether (2x30 mL) yielding **3l** in 75% (7.47 g). Yellow solid. M.p. = 167-172°C. **1H NMR** (600 MHz, CDCl₃) δ: 8.19 (s, 1H), 7.80 (dd, J = 8.9, 2.3 Hz, 1H), 7.75 (d, J = 2.3 Hz, 1H), 7.31 (d, J = 8.9 Hz, 1H); **13C NMR** (151 MHz, CDCl₃) δ: 155.78, 153.53, 150.49, 138.29, 131.45, 119.28, 118.61, 118.54, 113.20, 104.78.

Ethyl 6,7-dibromo-2-oxo-2H-chromene-3-carboxylate 4l:
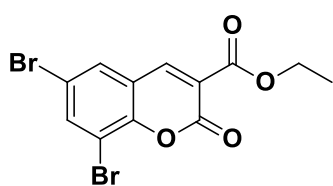
3,5-dibromo-2-hydroxybenzaldehyde (0.049 mol), diethyl malonate (0.049 mol), piperidine (10 mol %) and acetic acid (4 drops) were dissolved in ethanol (200 mL) and stirred at 50°C for 16h. The reaction mixture was concentrated under vacuum and the obtained crude solid was crystallized in methanol yielding **4l** in 87% (15.9 g). Pale yellow crystals. IR (KBr): ν = 3030, 1776 cm⁻¹. M.p. 231-233°C. **1H NMR** (500 MHz, CDCl₃) δ: 1.41 (t, 3H, J = 9.0Hz), 4.42 (q, 2H, J = 9.0Hz), 7.69 (d, 1H, J = 3.0Hz), 7.98 (d, 1H, J = 2.0Hz), 8.37 (s, 1H); **13C NMR** (125 MHz, CDCl₃) δ: 14.2, 61.4, 113.9, 122.7, 123.5, 125.6, 125.6,

127.0, 132.6, 151.4, 159.5, 165.0. **HRMS-ESI**: calcd for $C_{12}H_8Br_2O_4$ (396.8687), found (M-Na, 396.8688).

General procedure for synthesis of mono-arylcumarinic derivatives:
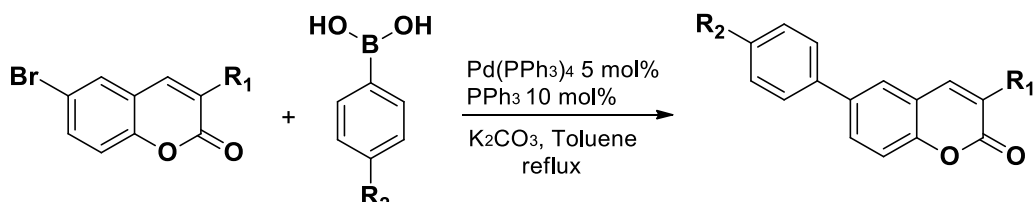
In a Schlenk, Pd(PPh₃)₄, (5 mol%) K_2CO_3 (1.85 mmol, 2.2 equiv) and mono-bromocumarin (250 mg, 0.84 mmol) were subsequently added under árgon atmosphere. The mixture was stirred for twenty minutes under vacuum and then degassed toluene (20 mL) was added. Boronic acid (1.1 equiv.) was added in one portion. The new solution was further degassed and stirred at 120°C for 12-16h. The reaction mixture was then brought to room temperature and filtered on silica (solvent: CH_2Cl_2 or MeOH). The solution was concentrated under vacuum obtaining the desired coumarin derivative. If necessary, the solid was recrystallized using EtOAc/n-hexane.

.

Ethyl 2-oxo-7-phenyl-2H-chromene-3-carboxylate P1:
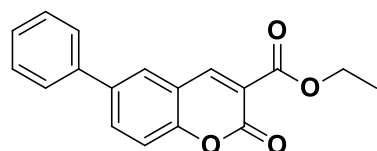
Pd(PPh₃)₄ (48.5 mg, 5 mol%), K_2CO_3 (255 mg, 1.85 mmol) and **1l** (250 mg, 0.84 mmol), phenylboronic acid (112 mg, 0.92 mmol), toluene (20 mL). Yellow powder, 55% yield (136 mg). M.p. 162-167°C. **¹H NMR** (500 MHz, CDCl₃) δ: 8.59 (s, 1H), 7.86 (dt, J = 13.4, 6.8 Hz, 1H), 7.80 (d, J = 1.6 Hz, 1H), 7.59 (d, J = 7.4 Hz, 2H), 7.50 (t, J = 7.6 Hz, 2H), 7.42 (t, J = 8.7 Hz, 2H), 4.44 (q, J = 7.1 Hz, 2H), 1.44 (t, J = 7.1 Hz, 3H); **¹³C NMR** (126 MHz, CDCl₃) δ: 165.7, 159.3, 157.1, 151.2, 141.5, 140.9, 135.9, 131.7, 130.7, 130.1, 129.6, 121.3, 120.7, 119.8, 64.6, 16.9. **HRMS-ESI**: calcd for $C_{18}H_{14}O_4$ (317.0789), found (M-Na⁺, 317.0773).

Ethyl 7-(4-methoxyphenyl)-2-oxo-2H-chromene-3-carboxylate P2:
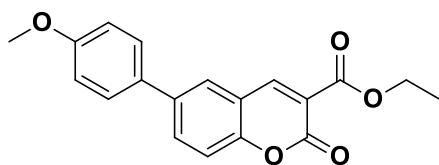
Pd(PPh$_3$)$_4$ (48.5 mg, 5 mol%), K$_2$CO$_3$ (255 mg, 1.85 mmol) and **1l** (250 mg, 0.84 mmol), 4-methoxyphenyl-boronic acid (131 mg, 0.92 mmol), toluene (20 mL).

Yellow solid, 66% yield (179 mg). M.p. = 179-184°C. IR (KBr): v = 3037, 1775 cm^{-1}. **^{1}H NMR** (500 MHz, CDCl$_3$) δ: 1.41 (t, 3H, J = 7.0Hz), 3.87 (s, 3H), 4.42 (q, 2H, J = 7.0Hz), 7.01 (d, 2H, J = 9.0Hz), 7.41 (d, 1H, J = 9.0Hz), 7.51 (d, 1H, J = 9.0Hz), 7.72 (d, 1H, J = 2Hz), 8.57 (s, 1H); ^{13}**C NMR** (126 MHz, CDCl$_3$) δ: 163.27, 159.89, 154.27, 148.81, 138.12, 133.07, 131.55, 128.25, 126.98, 118.76, 118.26, 117.25, 114.72, 107.49, 62.16, 55.57, 14.40. **HRMS-ESI**: calcd for C$_{19}$H$_{16}$O$_5$ (324.0998), found (M-H$^+$, 325.1076).

7-(4-methoxyphenyl)-2-oxo-2H-chromene-3-carbonitrile P6:
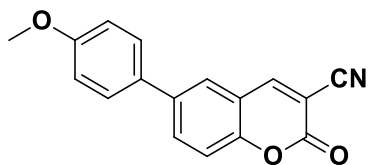
Pd(PPh$_3$)$_4$ (48.5 mg, 5 mol%), K$_2$CO$_3$ (255 mg, 1.85 mmol) and **3l** (209 mg, 0.84 mmol), 4-methoxyphenylboronic acid (131 mg, 0.92 mmol), toluene (20 mL). Yellow solid, 47% yield (109 mg). M.p. = 173-178°C. **^{1}H NMR** (500 MHz, CDCl$_3$) δ: 8.30 (s, 1H), 7.88 (dd, J = 8.7, 2.2 Hz, 1H), 7.70 (d, J = 2.1 Hz, 1H), 7.53 – 7.47 (m, 2H), 7.45 (d, J = 8.7 Hz, 1H), 3.87 (s, 3H); ^{13}**C NMR** (126 MHz, CDCl3) δ: 162.6, 159.0, 156.1, 154.4, 141.5, 136.6, 133.3, 130.7, 129.1, 120.3, 119.9, 117.3, 116.1, 106.2, 58.0. **HRMS-ESI**: calcd for C$_{17}$H$_{11}$NO$_3$ (277.0738), found (M-H$^+$, 278.0807).

7-(4-methoxyphenyl)-3-(methylsulfonyl)-2H-chromen-2-one P5:
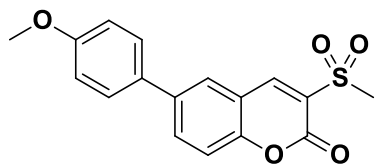
$Pd(PPh_3)_4$ (48.5 mg, 5 mol%), K_2CO_3 (255 mg, 1.85 mmol) and **2l** (253 mg, 0.84 mmol), 4-methoxyphenylboronic acid (131 mg, 0.92 mmol), toluene (20 mL). Yellow solid, 54% yield (150 mg). M.p. = 183-188°C. **^{1}H NMR** (600 MHz, CDCl3) δ: 8.69 (s, 1H), 7.91 (dd, J = 8.7, 2.2 Hz, 1H), 7.80 (d, J = 2.1 Hz, 1H), 7.52 (d, J = 8.7 Hz, 2H), 7.48 (d, J = 8.7 Hz, 1H), 7.03 (d, J = 8.7 Hz, 2H), 3.87 (s, 3H), 3.36 (s, 3H); **^{13}C NMR** (151 MHz, CDCl$_3$) δ: 160.12, 156.22, 154.29, 147.88, 139.01, 135.32, 134.24, 130.98, 128.32, 127.72, 117.61, 117.48, 114.84, 55.59, 41.93. **HRMS-ESI**: calcd for $C_{17}H_{14}O_5S$ (330.0561), found (M-H$^+$, 331.0630).

Ethyl 6-(6-methoxynaphthalen-2-yl)-2-oxo-2H-chromene-3-carboxylate P4:
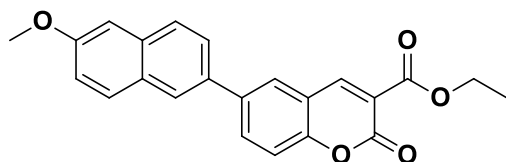
$Pd(PPh_3)_4$ (48.5 mg, 5 mol%), K_2CO_3 (255 mg, 1.85 mmol) and **1l** (209 mg, 0.84 mmol), 6-meth-oxynaphthalen-2-yl)boronic acid (186 mg, 0.92 mmol), toluene (20 mL). Yellow solid, 54% yield (169 mg). M.p. = 197-203°C. **^{1}H NMR** (600 MHz, CDCl$_3$) δ: 8.62 (s, 1H), 7.99 – 7.94 (m, 2H), 7.89 (d, J = 1.8 Hz, 1H), 7.85 (d, J = 8.5 Hz, 1H), 7.81 (d, J = 8.9 Hz, 1H), 7.67 (d, J = 8.4 Hz, 1H), 7.46 (d, J = 8.6 Hz, 1H), 7.21 (dd, J = 8.9, 2.3 Hz, 1H), 7.18 (d, J = 1.9 Hz, 1H), 4.44 (q, J = 7.1 Hz, 2H), 3.96 (s, 3H), 1.43 (t, J = 7.1 Hz, 3H); **^{13}C NMR** (151 MHz, CDCl$_3$) δ: 163.25, 158.34, 156.88, 154.54, 148.84, 138.49, 134.25, 134,13, 133.49, 129.86, 129.23, 127.90, 127.57, 125.96, 125.56, 119.81, 118.81, 118.36, 117.38, 105.77, 62.19, 55.54, 14.40. **HRMS-ESI**: calcd for $C_{23}H_{18}O_5$ (374.1154), found (M-H$^+$, 375.1216).

General procedure for synthesis of bis-arylcumarinic derivatives:
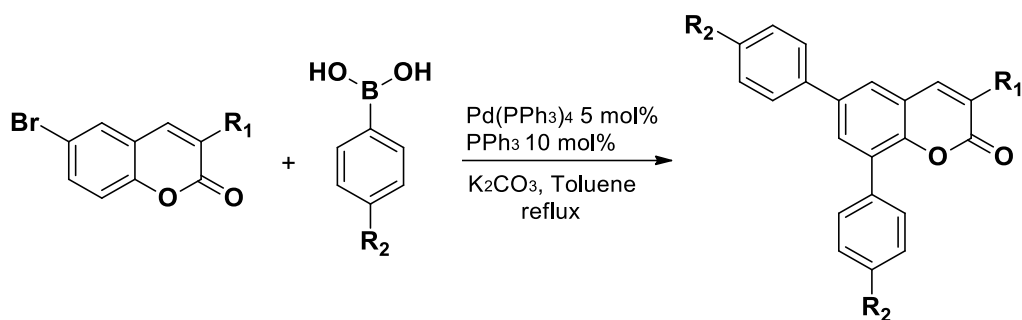
In a Schlenk, Pd(PPh₃)₄, (5 mol%) K₂CO₃ (3.70 mmol, 4.4 equiv) and bis-bromocumarin (250 mg, 0.66 mmol) were added under argon atmosphere. The mixture was stirred for twenty minutes under vacuum and then degassed toluene (20 mL) was added. Boronic acid (2.2 equiv) was added to this stirring solution in one portion. The new solution was further degassed and stirred at 120 ° C for 12-16 hours. The reaction mixture was then brought to room temperature and filtered on silica (solvent: CH_2Cl_2 or MeOH). The solution was concentrated under vacuum obtaining the desired coumarin derivative. If necessary, the solid was recrystallized using EtOAc/n-hexane.

Ethyl 2-oxo-6,7-diphenyl-2H-chromene-3-carboxylate P7:
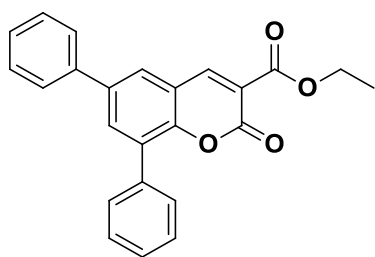
Pd(PPh₃)₄ (38.1 mg, 5 mol%), K₂CO₃ (510 mg, 3.70 mmol) and **4l** (250 mg, 0.66 mmol), phenylboronic acid (163 mg, 1.45 mmol), toluene (20 mL). Yellow solid, yield, 46% (142 mg). M.p. = 199-204°C. **¹H NMR** (500 MHz, CDCl₃) δ: 8.61 (s, 1H), 7.91 (d, J = 2.2 Hz, 1H), 7.77 (d, J = 2.2 Hz, 1H), 7.64 (dd, J = 14.0, 7.4 Hz, 4H), 7.50 (q, J = 7.4 Hz, 4H), 7.43 (dt, J = 10.9, 7.4 Hz, 2H), 4.43 (q, J = 7.1 Hz, 2H), 1.42 (t, J = 7.1 Hz, 3H); **¹³C NMR** (126 MHz, CDCl₃) δ: 165.7, 158.9, 154.0, 151.4, 141.5, 140.7,

137.7, 137.0, 133.3, 132.1, 131.7, 131.3, 131.0, 130.7, 129.7, 129.2, 121.3, 109.9, 64.6, 16.8. **HRMS-ESI**: calcd for $C_{24}H_{18}O_4$ (370.1205), found (M-H⁺, 371.1289).

Ethyl 6,7-bis(4-methoxyphenyl)-2-oxo-2H-chromene-3-carboxylate P8:
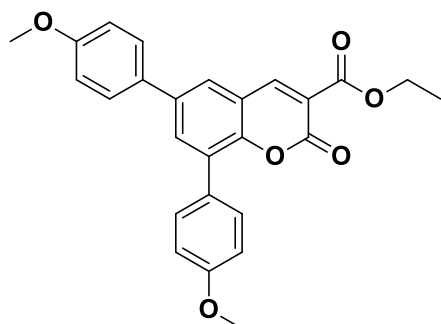
Pd(PPh₃)₄ (38.1 mg, 5 mol%), K₂CO₃ (510 mg, 3.70 mmol) and **4l** (250 mg, 0.66 mmol), 4-methoxyphenyl-boronic acid (206 mg, 1.45 mmol), toluene (20 mL). Yellow solid, yield, 58% (165 mg). M.p. = 241-246°C.

IR (KBr): v = 3039, 1777 cm⁻¹. **¹H NMR** (500 MHz, CDCl₃) δ: 8.58 (s, 1H), 7.83 (d, J = 2.2 Hz, 1H), 7.66 (d, J = 2.1 Hz, 1H), 7.59 (d, J = 8.7 Hz, 2H), 7.54 (d, J = 8.7 Hz, 2H), 7.01 (t, J = 8.1 Hz, 4H), 4.42 (q, J = 7.1 Hz, 2H), 3.87 (d, J = 3.3 Hz, 6H), 1.41 (t, J = 7.1 Hz, 3H); **¹³C NMR** (126 MHz, CDCl₃) δ: 163.27, 159.86, 159.85, 156.57, 151.05, 149.13, 137.83, 133.80, 131.54, 130.79, 130.30, 128.23, 127.55, 125.69, 118.76, 118.51, 116.15, 114.91, 114.67, 114.26, 62.06, 55.53, 55.49, 14.34. **HRMS-ESI**: calcd for $C_{19}H_{16}O_5$ (430.1416), found (M-H⁺, 430.1417).

General procedure for synthesis of 6-functionalized cumarin derivatives:
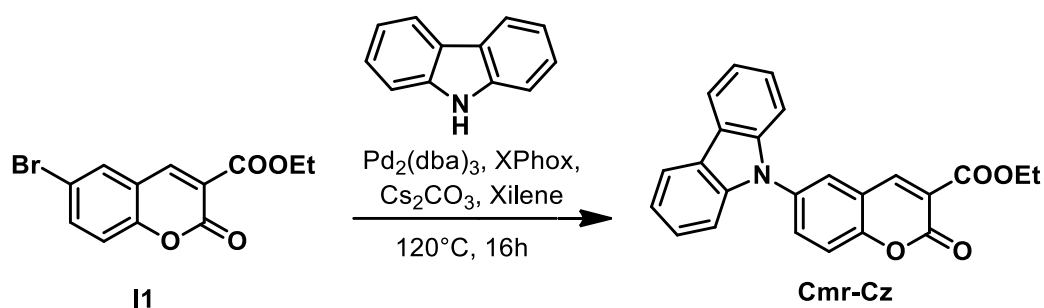
I1 (0.120 g, 0.4 mmol, 1 equiv.), Carbazole (0.066 g, 0.4 mmol, 1 equiv.), $Pd_2(dba)_3$ (0.006 g, 0.01 mmol, 0.06 equiv.), Cs_2CO_3 (0.390 g, 1.2 mmol, 3 equiv.) and XPhox (0.005 g, 0.006 mmol, 0.006 equiv.) has been dried under vacuum for 20 minutes. Then Xylene (6 mL) has been added and the so obtained reaction solution was stirred at 120 °C overnight. The mixture was diluted with chloroform and washed with water. The organic layer was separated and dried over anhydrous Na_2SO_4. After vacuum concentration, the residue was absorbed onto silica gel and purified by flash column chromatography on silica gel using ethyl acetate/petroleum ether (1:9) as eluent to afford the clean product.

Ethyl 6-(9H-carbazol-9-yl)-2-oxo-2H-chromene-3-carboxylate – Cmr-Cz
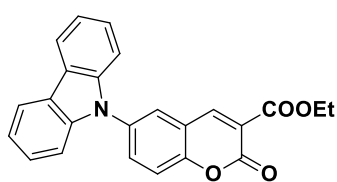
Yield:40%. **^{1}H NMR** (600 MHz, CDCl$_3$): δ = 1H NMR (600 MHz, CDCl3) δ 8.55 (s, 1H), 8.16 (d, *J* = 7.7 Hz, 2H), 7.87 – 7.80 (m, 2H), 7.60 (d, *J* = 8.7 Hz, 1H), 7.46 – 7.40 (m, 2H), 7.38 – 7.29 (m, 4H), 4.44 (q, *J* = 7.1 Hz, 2H), 1.43 (t, *J* = 7.1 Hz, 3H). **^{13}C NMR** (125 MHz, CDCl$_3$): δ = 162.88, 156.38, 153.95, 147.73, 140.82, 134.66, 133.22, 127.49, 126.43, 123.72, 120.74, 119.57, 119.13, 118.72, 109.35, 62.36, 14.36. **HRMS-ESI**: calcd for $C_{24}H_{17}NO_4$ (383.1157), found (M-Na$^+$, 406.1040). **M.p.** 169-172°C.

Ethyl 2-oxo-6-(10H-phenoxazin-10-yl)-2H-chromene-3-carboxylate – Cmr-Pox
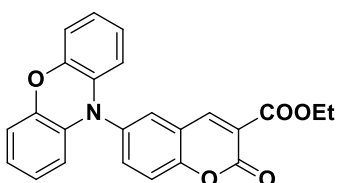
I1 (0.120 g, 0.4 mmol, 1 equiv.), Phenoxazine (0.073 g, 0.4 mmol, 1 equiv.), $Pd_2(dba)_3$ (0.006 g, 0.01 mmol, 0.06 equiv.), Cs_2CO_3 (0.390 g, 1.2 mmol, 3 equiv.) and XPhox (0.005 g, 0.006 mmol, 0.006 equiv.) **Yield**:25%. **^{1}H NMR** (600 MHz, CDCl$_3$): δ = 8.50 (s, 1H), 7.67

– 7.62 (m, 2H), 7.59 (d, J = 8.6 Hz, 1H), 6.71 (dtd, J = 9.2, 7.9, 1.5 Hz, 4H), 6.63 – 6.58 (m, 2H), 5.88 (dd, J = 8.0, 1.3 Hz, 2H), 4.43 (q, J = 7.1 Hz, 2H), 1.41 (t, J = 7.1 Hz, 3H).^{13}**C NMR** (125 MHz, CDCl₃): δ = 162.82, 156.27, 154.68, 147.50, 144.08, 137.41, 135.91, 133.97, 132.27, 123.50, 122.22, 120.14, 119.24, 116.01, 113.25, 62.38, 14.36.

Ethyl 2-oxo-6-(10H-phenothiazin-10-yl)-2H-chromene-3-carboxylate – Cmr-Ptz
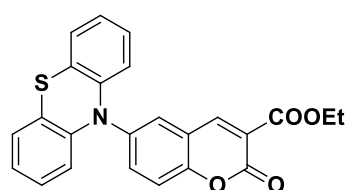
I1 (0.120 g, 0.4 mmol, 1 equiv.), Phenothiazine (0.079 g, 0.4 mmol, 1 equiv.), Pd₂(dba)₃ (0.006 g, 0.01 mmol, 0.06 equiv.), Cs₂CO₃ (0.390 g, 1.2 mmol, 3 equiv.) and XPhox (0.005 g, 0.006 mmol, 0.006 equiv.) **Yield**:30%. ^{1}**H NMR** (600 MHz, CDCl₃): δ = 8.49 (s, 1H), 7.68 – 7.61 (m, 2H), 7.55 (d, J = 8.7 Hz, 1H), 7.11 (dd, J = 7.2, 1.9 Hz, 2H), 6.95 – 6.87 (m, 4H), 6.29 (dd, J = 7.9, 1.5 Hz, 2H), 4.43 (q, J = 7.1 Hz, 2H), 1.41 (t, J = 7.1 Hz, 3H). ^{13}**C NMR** (125 MHz, CDCl₃): δ = 162.90, 156.41, 147.77, 143.72, 138.45, 135.97, 130.05, 127.45, 127.19, 123.60, 122.40, 119.81, 119.24, 117.28, 62.33, 14.36. **HRMS-ESI**: calcd for C₂₄H₁₇NO₄S (415.0878), found (M-H⁺, 415.0868).

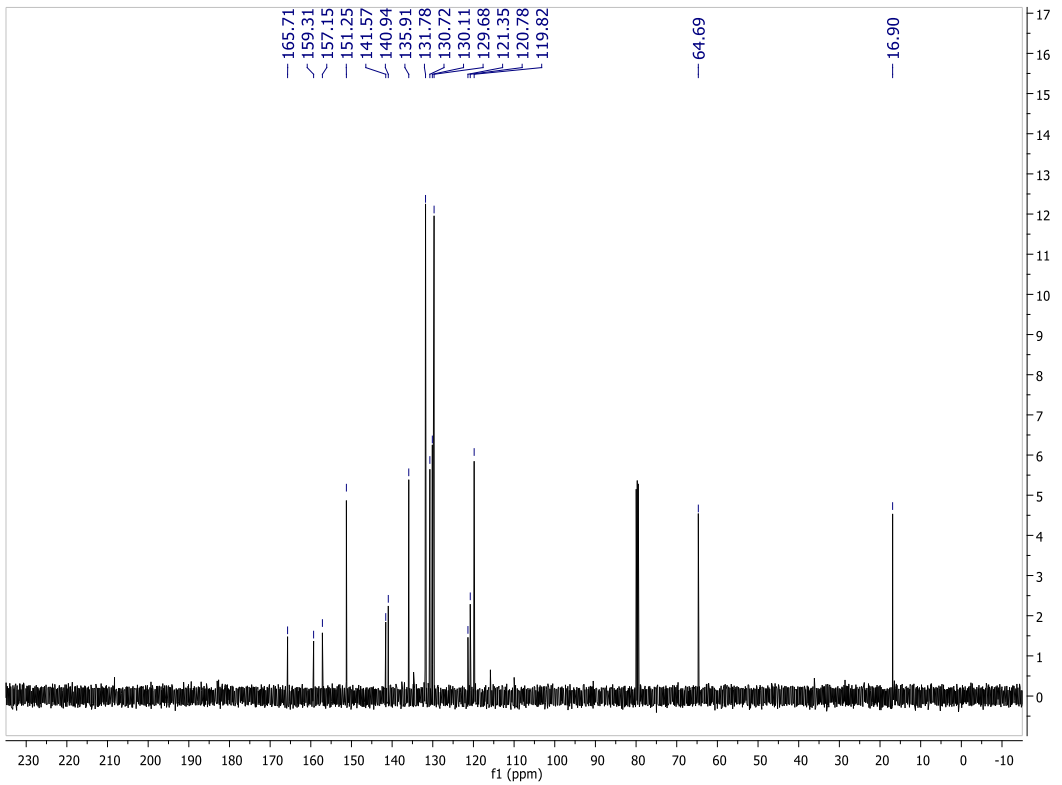## Synthesis of 4,4'-(spiro[fluorene-9,9'-xanthene]-2,7-diyl)dibenzonitrile; SFX-CN:
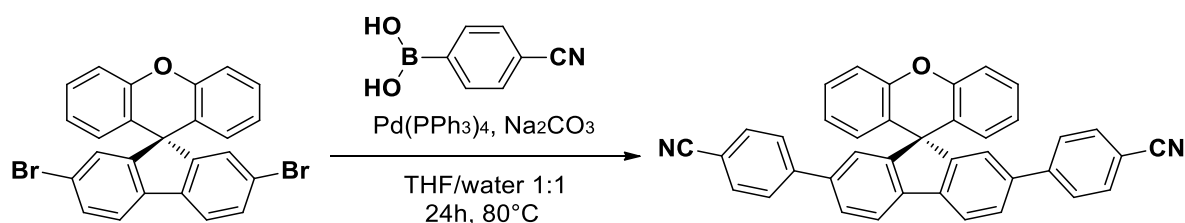
To a mixture of 2,7-dibromo-9,9'-spirobifluorene (500 mg, 1.02 mmol, 1 equiv.) and 4-cyanophenylboronic acid (527 mg, 3.59 mmol, 3.5 equiv.), Pd(PPh₃)₄ (59 mg, 0.05 mol, 0.05 equiv.) was added in nitrogen atmosphere. THF (15 mL) and 5M K₂CO₃ (5 mL)

aqueous solution was added into the mixture and heated to 80 °C with continuous stirring for 24 h under the protection of nitrogen. After cooling to room temperature, the organic layer was separated, and the aqueous layer was extracted with dichloromethane. The combined organic layer was washed three times with 10 mL of water and, brine, and dried over sodium sulfate. The solvent was removed under reduced pressure. The solid was placed on DCVC column and eluted with Hexane first and then Hexane/EtOAc 5/1, starting with pure Hexane. Through the procedure 425 mg of white solid were obtained. The solid was white. **Yield: 77 %.** **^{1}H NMR** (400 MHz, CD_2Cl_2) δ ppm: 8.03 (d, J = 8.0 Hz, 1H), 7.71 (ddd, J = 28.4, 14.0, 5.1 Hz, 5H), 7.46 (d, J = 1.3 Hz, 1H), 7.29 (dtd, J = 9.7, 8.2, 1.4 Hz, 2H), 6.91 – 6.81 (m, 1H), 6.53 (dd, J = 7.9, 1.3 Hz, 1H. **^{13}C NMR** (126 MHz, CD_2Cl_2) δ ppm): 156.46, 151.39, 144.90, 139.73, 139.52, 132.53, 128.55, 127.78, 127.57, 127.40, 124.32, 124.08, 123.45, 121.10, 118.78, 117.02, 110.95, 54.50. **HR-MS** (Xevo G2-XS QTof) [M+H]$^+$Calculated: ($C_{39}H_{22}N_2O$) 534.1732; found (M-Na$^+$, 557.1616).

Synthesis of 4,4'-(2',7'-diiodospiro[fluorene-9,9'-xanthene]-2,7-diyl)dibenzonitrile; SFX-CN-I:
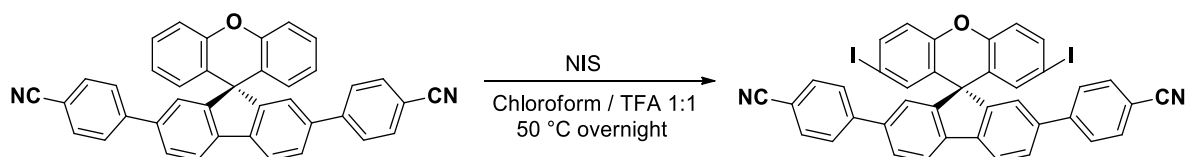
SFX-CN (600 mg, 1.12 mmol, 1 equiv.) and N-Iodosuccinimide (556 mg, 2.47 mmol, 2.2 equiv.) were dissolved in 21 mL of TFA and 20 mL of Chloroform and the reaction stirred at 50°C overnight. After that, TLC analyses indicated the complete consumption of no starting material. The reaction mixture and it was poured into water and extracted with DCM. The organic phase was dried over magnesium sulfate, filtrated and concentrated

on rotavapor under reduced pressure. The solid obtained was washed with ethyl acetate and filtered. The solid was placed on DCVC column and eluted with Hexane first and then Hexane/EtOAc 5/1The solid wasd pPlaced on DCVC column and eluted with Hexane/EtOAc 5/1, starting with pure Hexane. Through the procedure 710 mg of white solid were obtained. The solid was white. **Yield 80%.** [1]**H NMR** (400 MHz, CDCl3) δ ppm: 7.98 (d, J = 8.0 Hz, 1H), 7.70 (ddd, J = 26.5, 15.3, 5.1 Hz, 5H), 7.54 (dd, J = 8.7, 2.1 Hz, 1H), 7.35 (d, J = 1.2 Hz, 1H), 7.04 (d, J = 8.7 Hz, 1H), 6.70 (d, J = 2.1 Hz, 1H. [13]**C NMR** (101 MHz, CDCl3) δ ppm): 155.38, 150.75, 144.87, 140.13, 139.24, 137.77, 136.23, 132.59, 128.06, 127.8, 126.28, 124.31, 121.44, 119.40, 118.86, 111.13, 86.55, 53.69.

General procedure for Buchwald-Hartwig Cross Coupling Reaction:
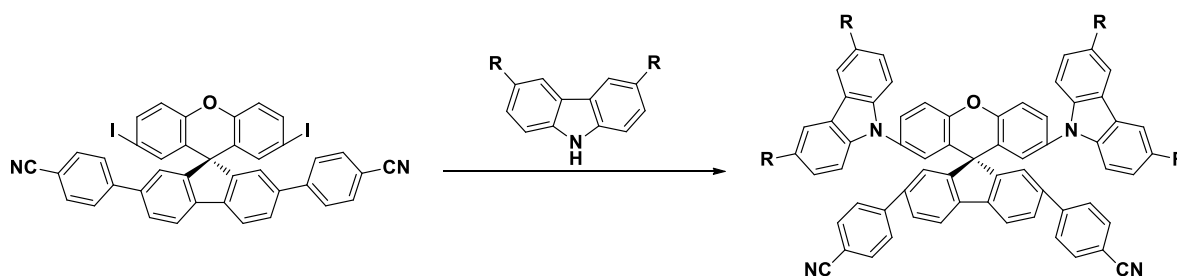
SFX-CN-I (800 mg, 1.02 mmol, 1 equiv.), carbazole derivative (3 equiv.) and t-BuONa (489 mg, 5.09 mmol, 5 equiv.) were added to 42 mL dry toluene in three-necked flask. The system was purged with nitrogen several times, and then $Pd_2(dba)_3$ (90 mg, 0.1 mmol, 0.1 equiv.) and $[(t-Bu)_3PH]BF_4$ (110 mg, 0.4 mmol, 0.4 equiv.) were put into added to the reaction mixture, which was then stirred at solution under 110 °C for 48 h under nitrogen the protection of nitrogen. After that, TLC analyses indicated the complete consumpotion of no starting material. The reaction mixture and it was poured into water and extracted with DCM. The organic phase was dried over magnesium sulfate, filtrated and concentrated on rotavapor under reduced pressure. The solid obtained was washed

with ethyl acetate and filtered. The solid was placed on DCVC column and eluted with pentane and then pentane/DCM 1/1, starting with pure Pentane.

4,4'-(2',7'-di(9H-carbazol-9-yl)spiro[fluorene-9,9'-xanthene]-2,7-diyl)dibenzonitrile; SFX-CN-Cz:
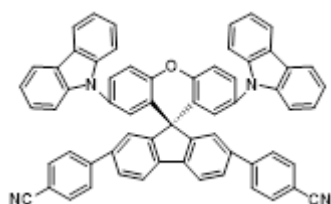
Through the procedure 260 mg of white solid were obtained. White solid. **Yield: 30%. Mp: 379 °C**. **^{1}H NMR** (500 MHz, CDCl3) δ ppm: 8.06 (d, J = 7.5 Hz, 2H), 7.83 (d, J = 8.0 Hz, 1H), 7.80 – 7.58 (m, 7H), 7.55 (dd, J = 8.7, 2.4 Hz, 1H), 7.19 (ddd, J = 15.3, 14.2, 7.1 Hz, 4H), 7.10 (d, J = 7.9 Hz, 2H), 6.78 (d, J = 2.4 Hz, 1H). **^{13}C NMR** (126 MHz, CDCl3) δ ppm): 155.73, 150.07, 145.13, 140.25, 139.33, 133.20, 132.71, 128.02, 127.78, 127.08, 126.32, 125.76, 125.21, 124.14, 123.22, 121.57, 120.38, 120.02, 118.83, 111.25, 109.26, 54.70. **HR-MS** (Xevo G2-XS QTof) [M+H]$^+$Calculated: ($C_{63}H_{36}N_4O$) 865.2967; found (M-H$^+$, 865.2906. Anal. Calcd. ($C_{63}H_{36}N_4O$): C, 87.48; H, 4.19; N, 6.48. Found: C, 87.98; H, 3.79; N, 6.47.

4,4'-(2',7'-bis(3,6-di-tert-butyl-9H-carbazol-9-yl)spiro[fluorene-9,9'-xanthene]-2,7-diyl)dibenzonitrile; SFX-CN-tBuCz:
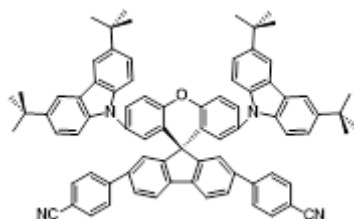
Through the procedure 390 mg of white solid were obtained. White solid. **Yield: 35%. Mp > 400 °C**. **^{1}H NMR** (300 MHz, CDCl3) δ ppm): 7.94 (d, 2H), 7.79 – 7.29 (m, 9H), 7.11 (dd, 2H), 6.91 (d, 2H), 6.66 (d, 1H), 1.31 (s, 17H). **^{13}C NMR** (101 MHz, CDCl3) δ ppm): 155.57, 149.94, 145.24, 142.93, 140.10, 139.37, 138.78, 133.66,

132.65, 127.90, 126.83, 125.85, 125.32, 124.12, 123.28, 121.61, 118.78, 116.33, 111.19, 108.68, 54.82, 34.67, 31.95. **HR-MS** (Xevo G2-XS QTof) [M+H]$^+$ Calculated: (C$_{79}$H$_{68}$N$_4$O) 1089.5393; Found: 1089.5397. Anal. Calcd. (C$_{79}$H$_{68}$N$_4$O): C, 87.10; H, 6.29; N, 5.14. Found: C, 86.25; H, 6.2 0; N, 4.99.

5.7 ^{1}H and ^{13}C NMR spectra

¹H and ¹³C NMR spectra

1H NMR peaks: 8.58, 7.83, 7.83, 7.66, 7.66, 7.59, 7.58, 7.55, 7.53, 7.26 Chloroform-d, 7.03, 7.01, 7.00, 4.44, 4.43, 4.41, 4.40, 3.87, 3.86, 1.43, 1.41, 1.40

Integrations: 0.95, 1.00, 1.04, 2.26, 2.21, 4.15, 2.06, 6.13, 2.99

13C NMR peaks: 163.27, 159.86, 159.85, 156.57, 151.05, 149.13, 137.83, 133.80, 131.54, 130.79, 130.30, 128.23, 127.55, 125.69, 118.76, 118.51, 114.91, 114.67, 114.26, 77.16 Chloroform-d, 62.06, 55.53, 55.49, 14.34
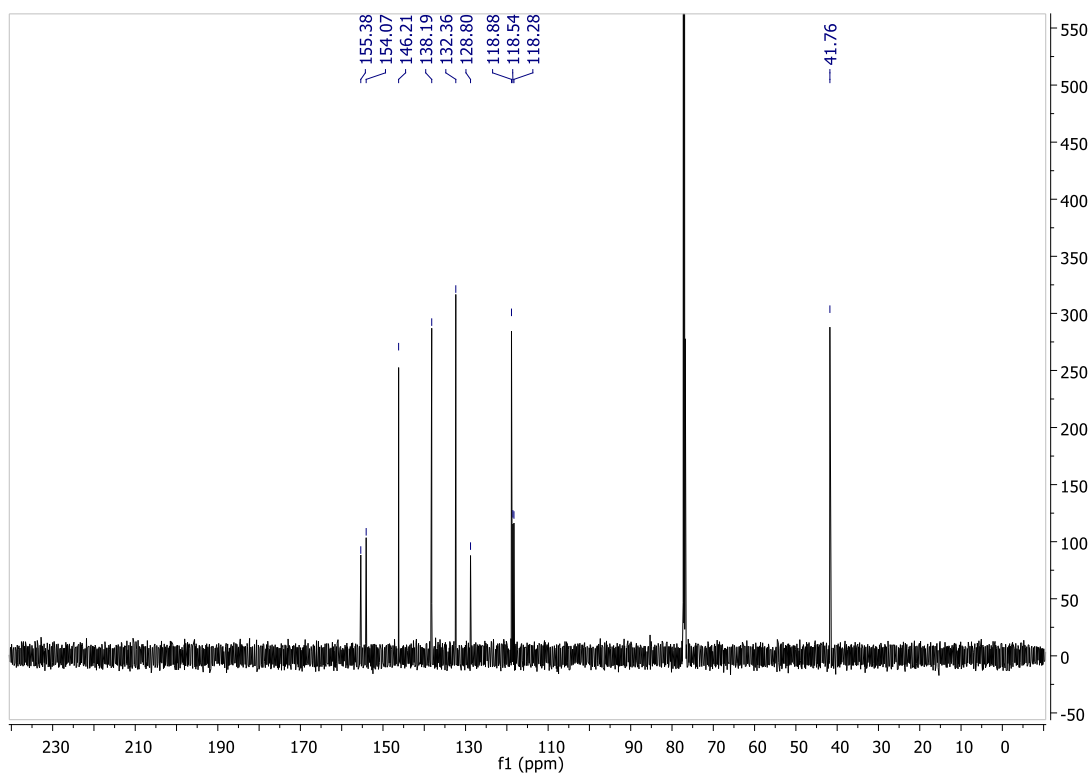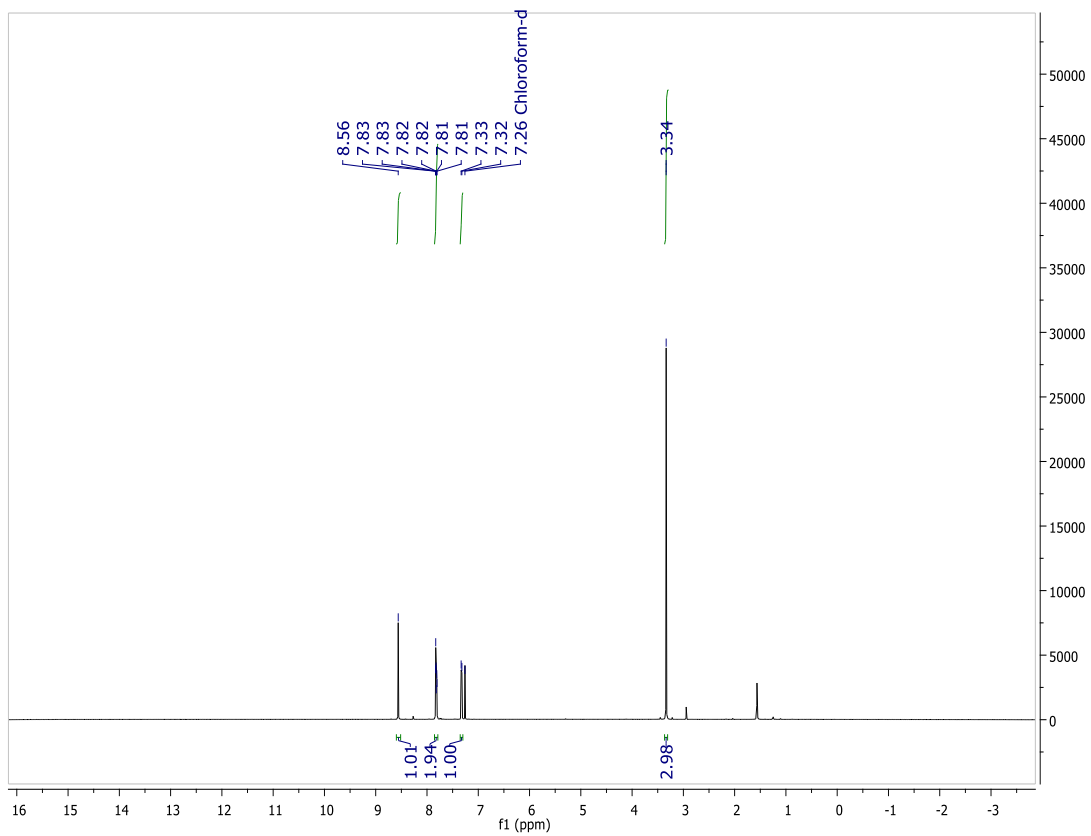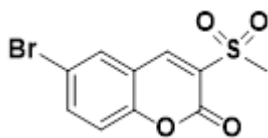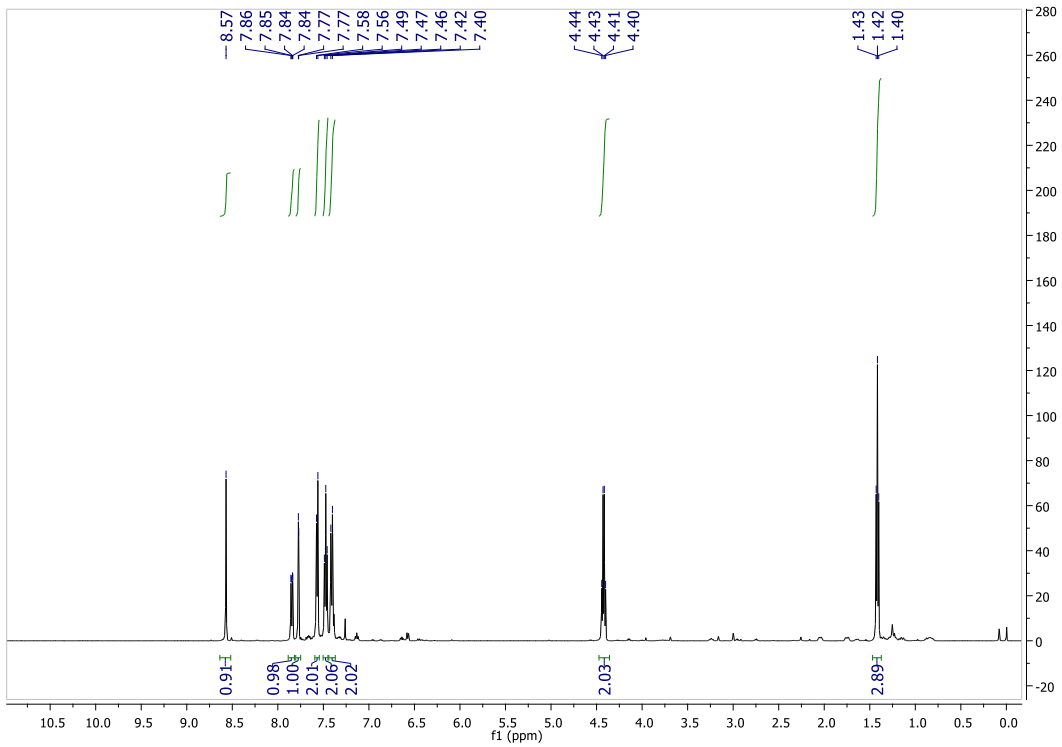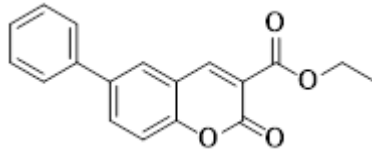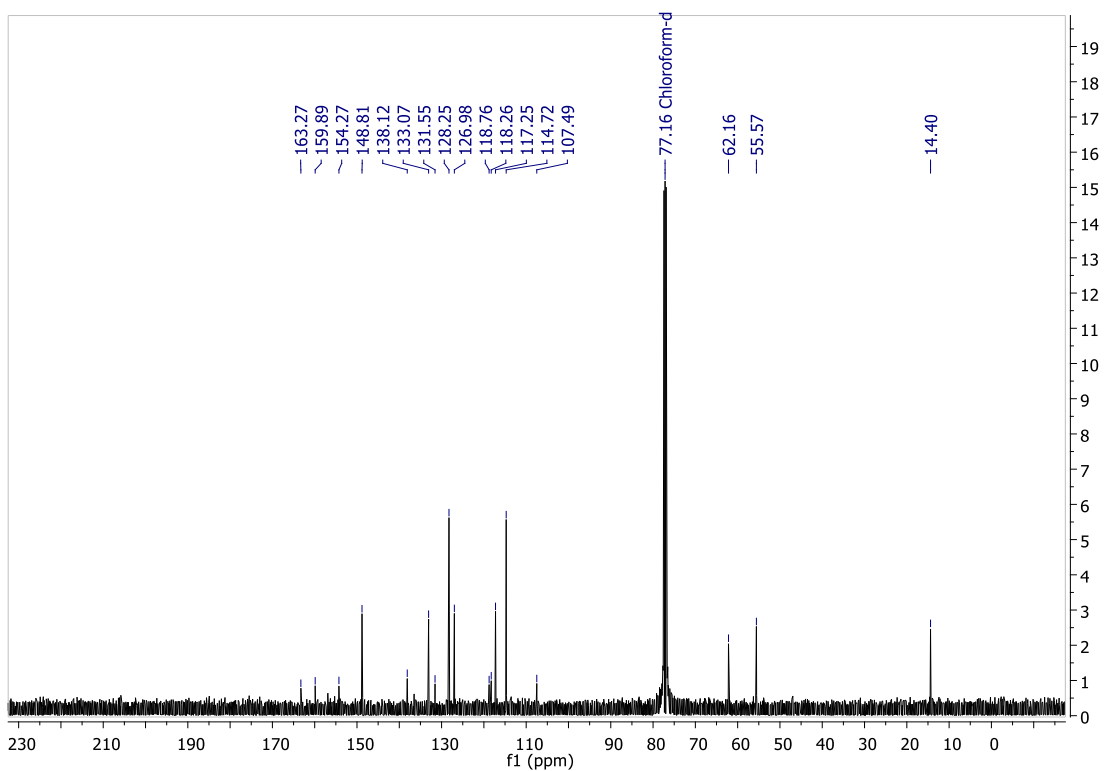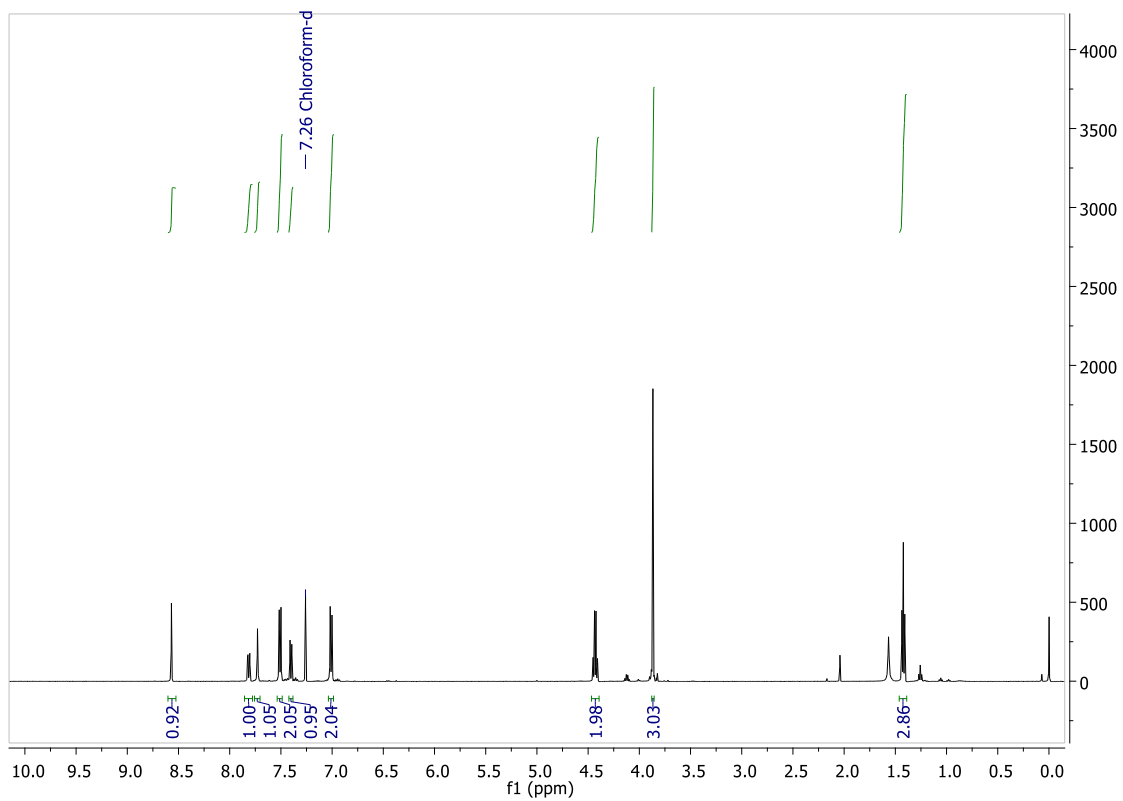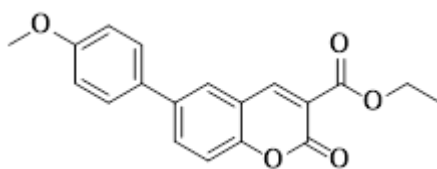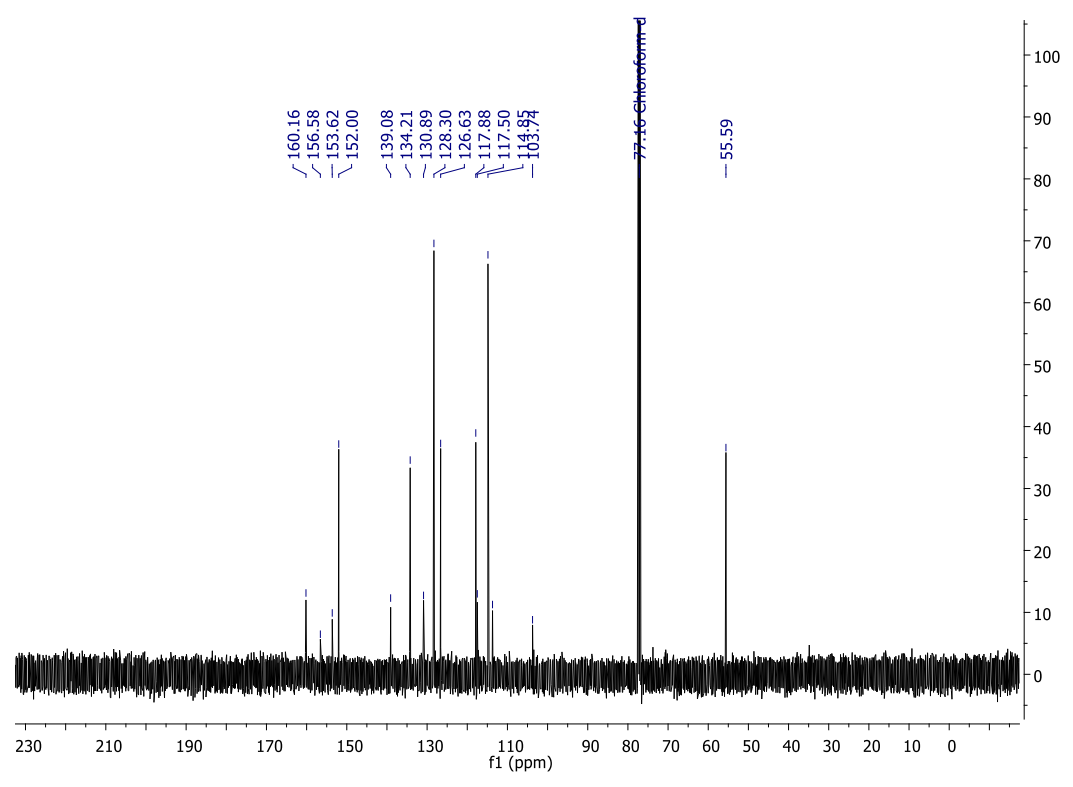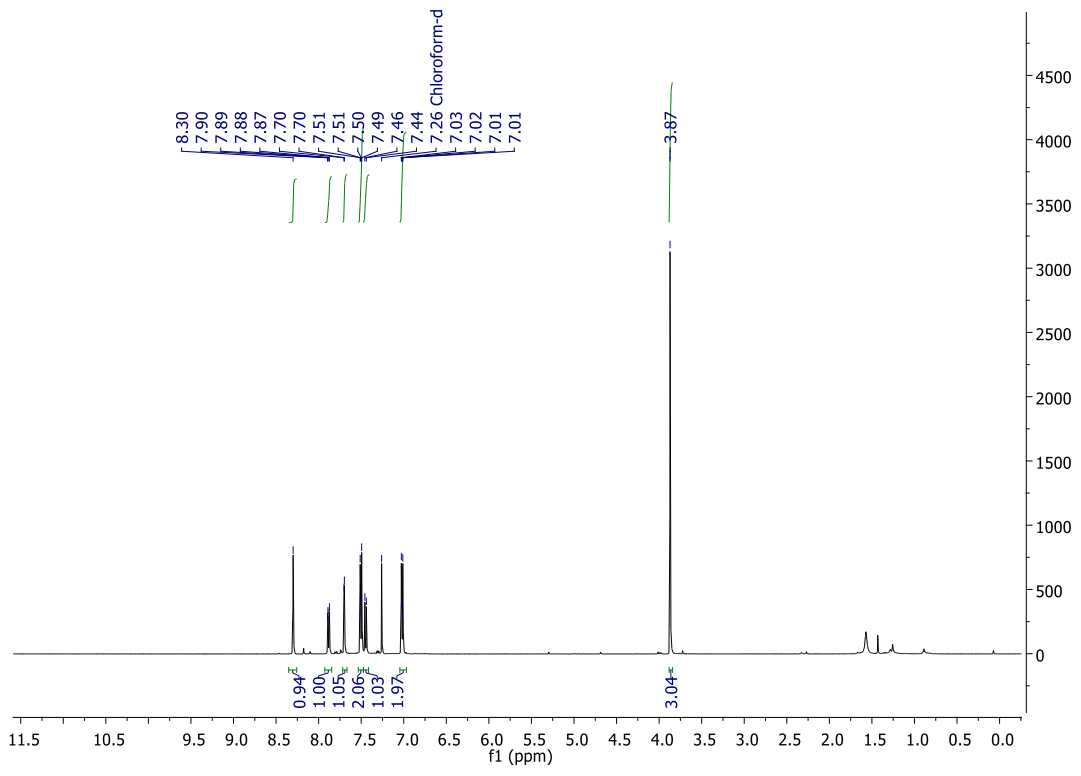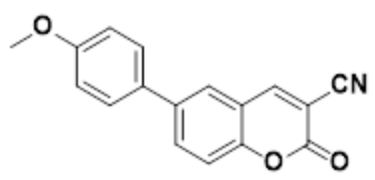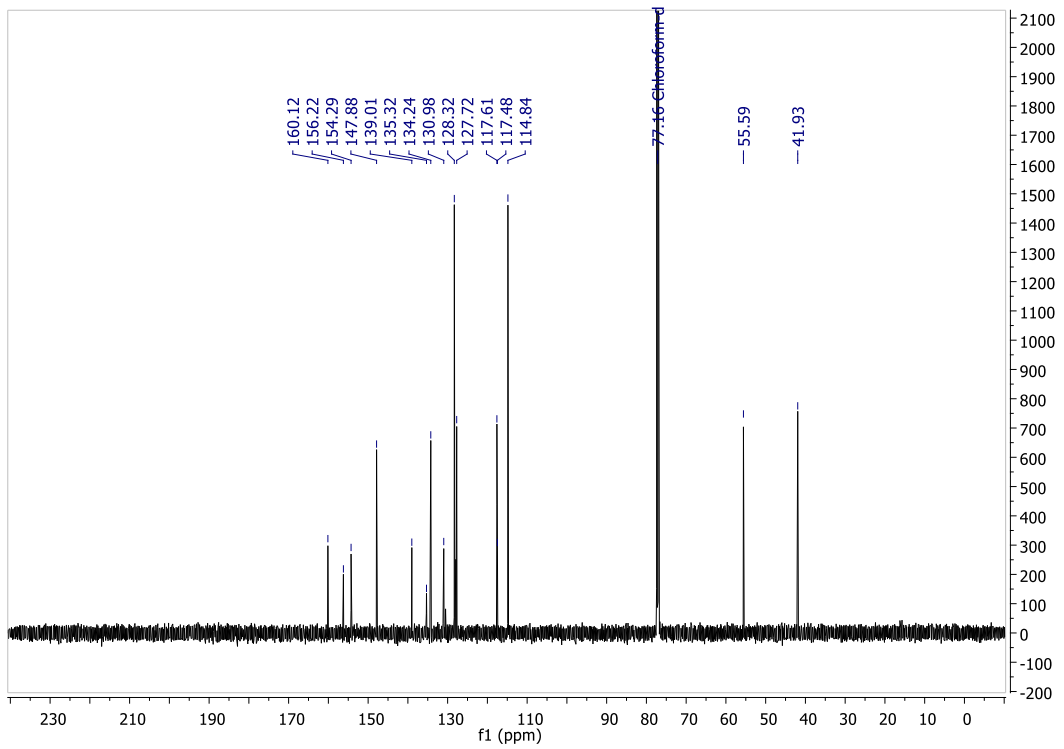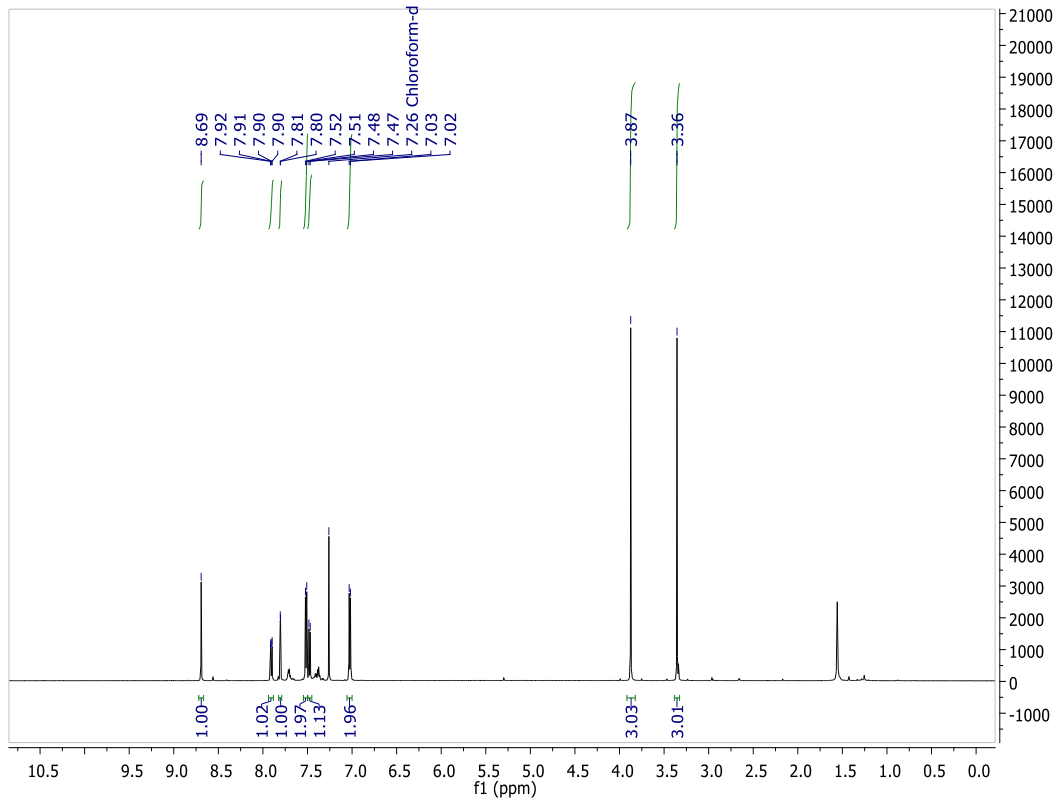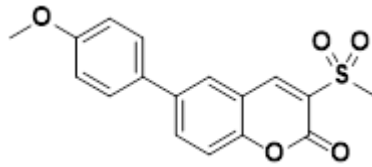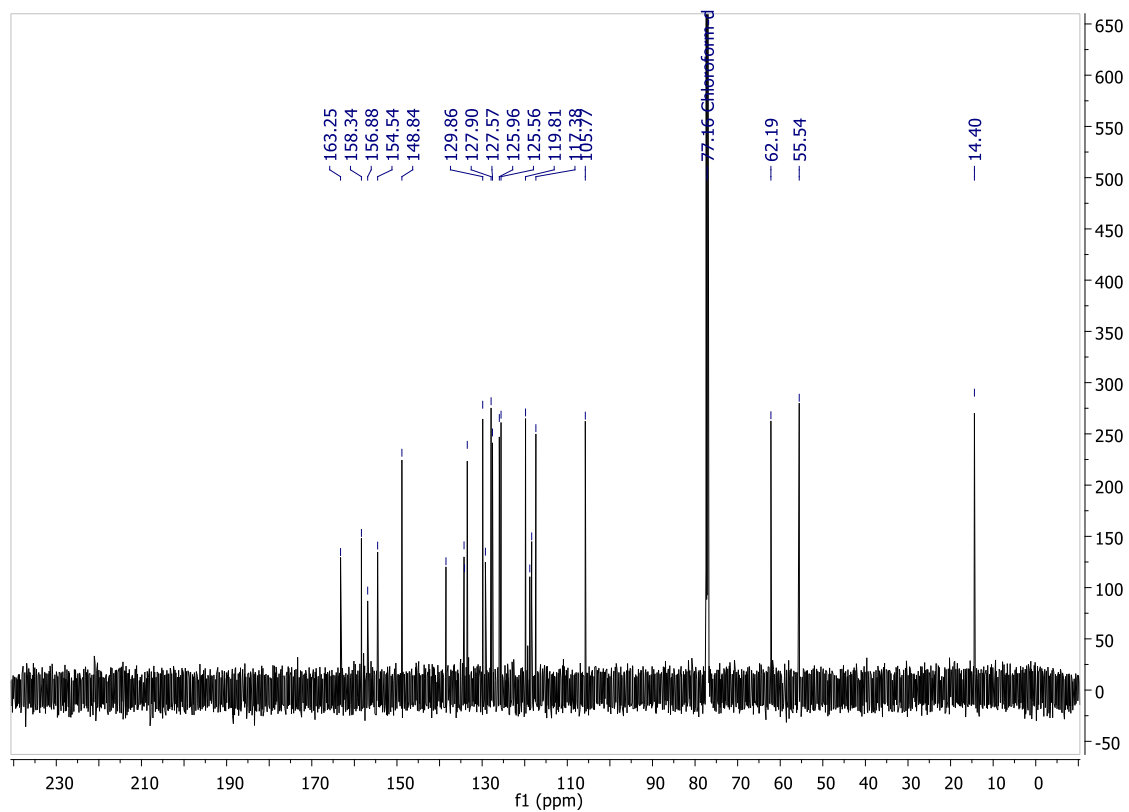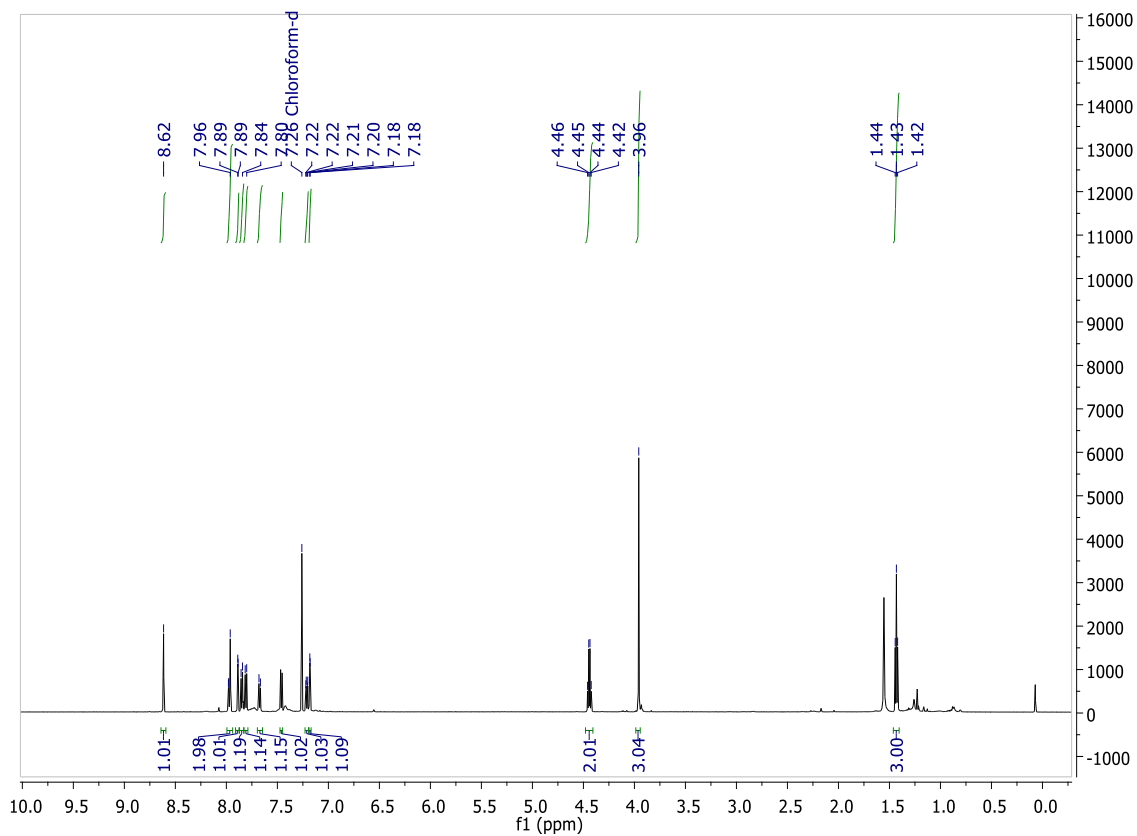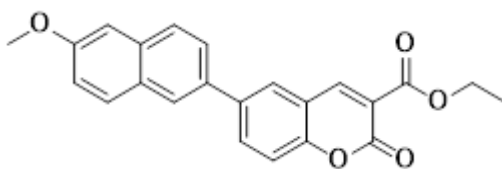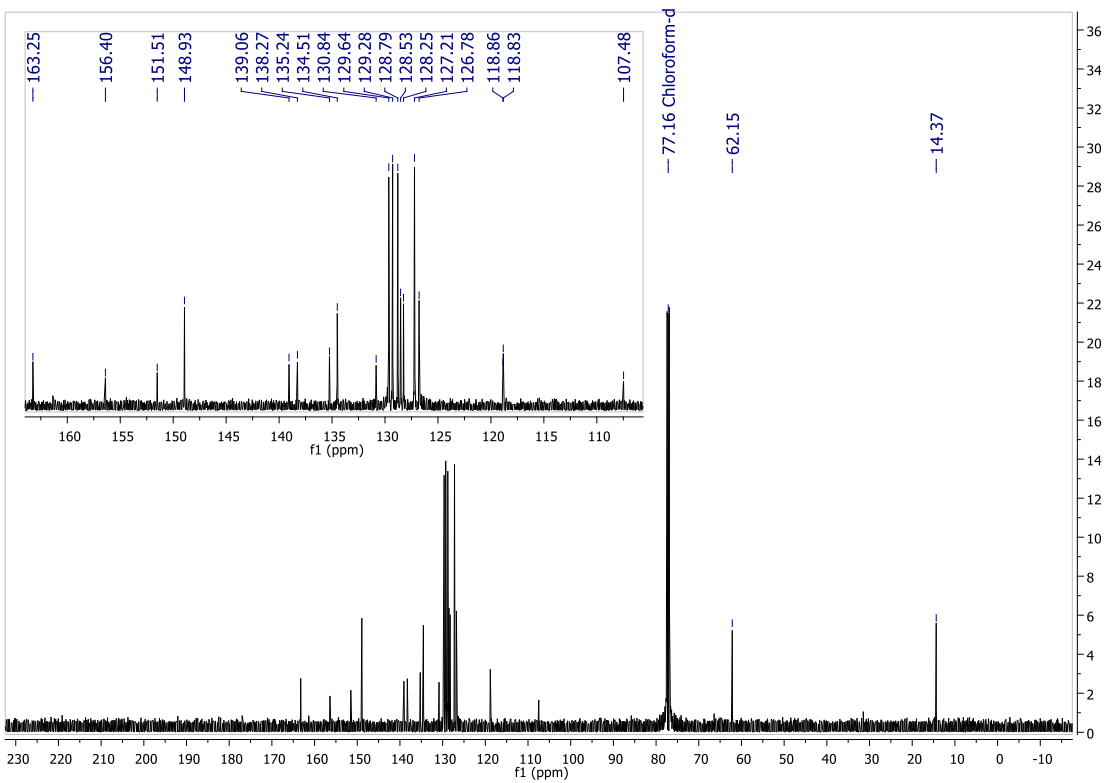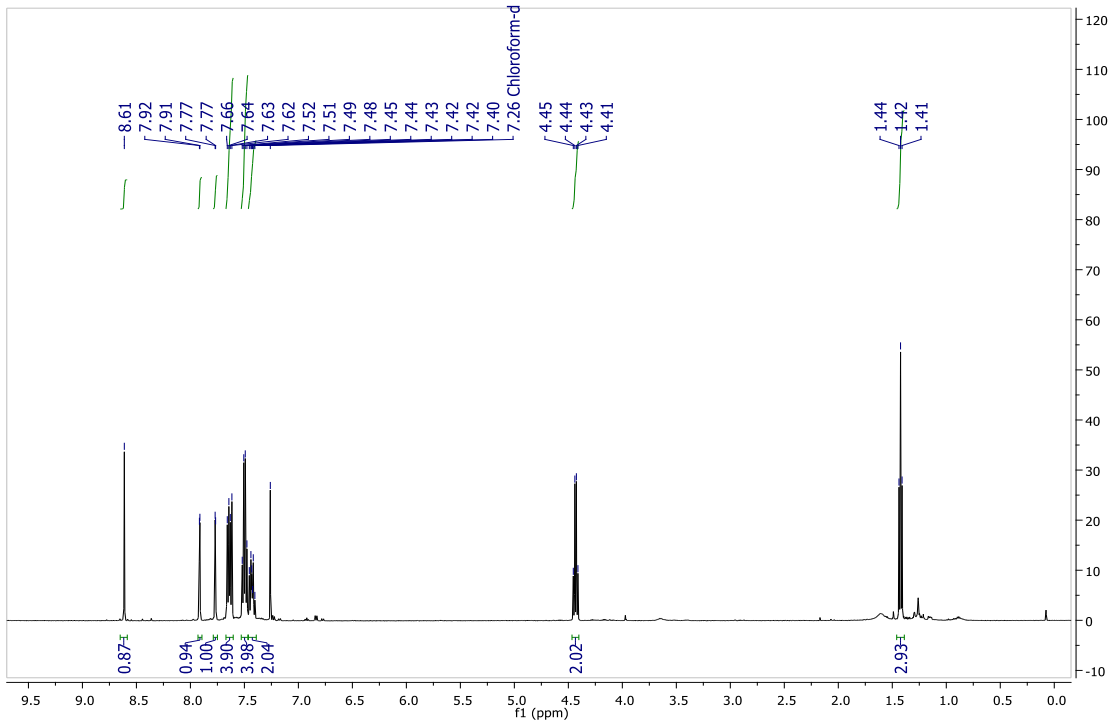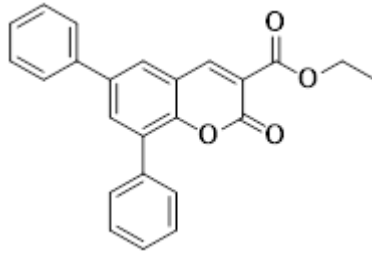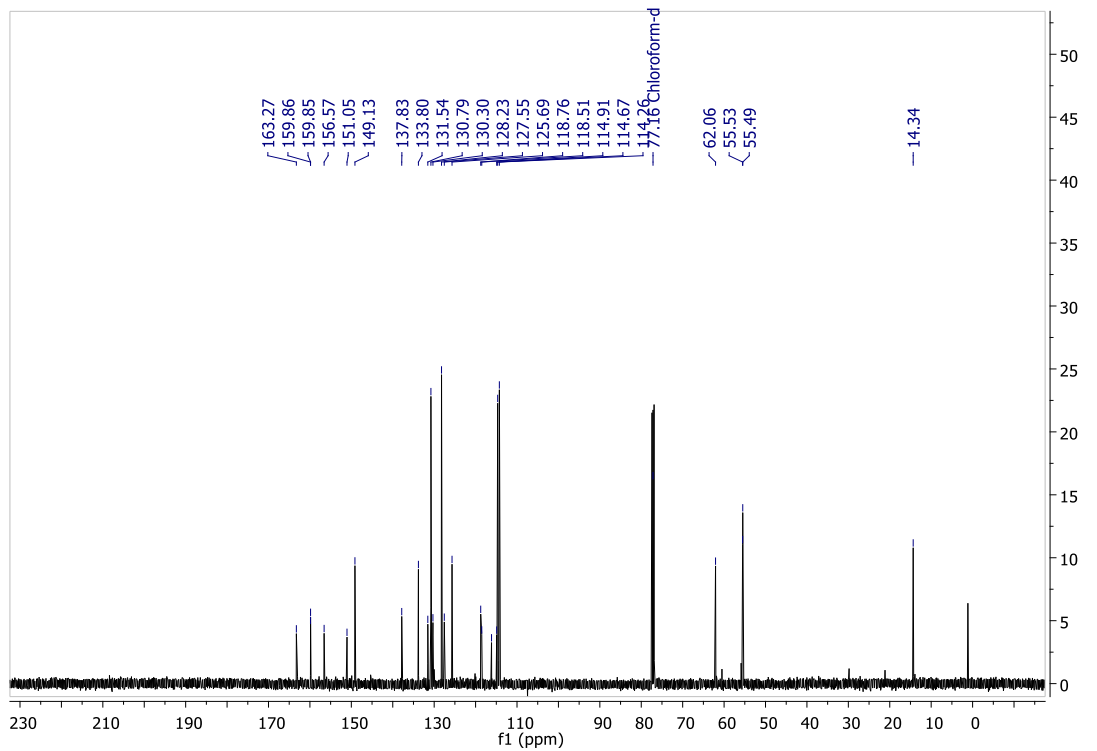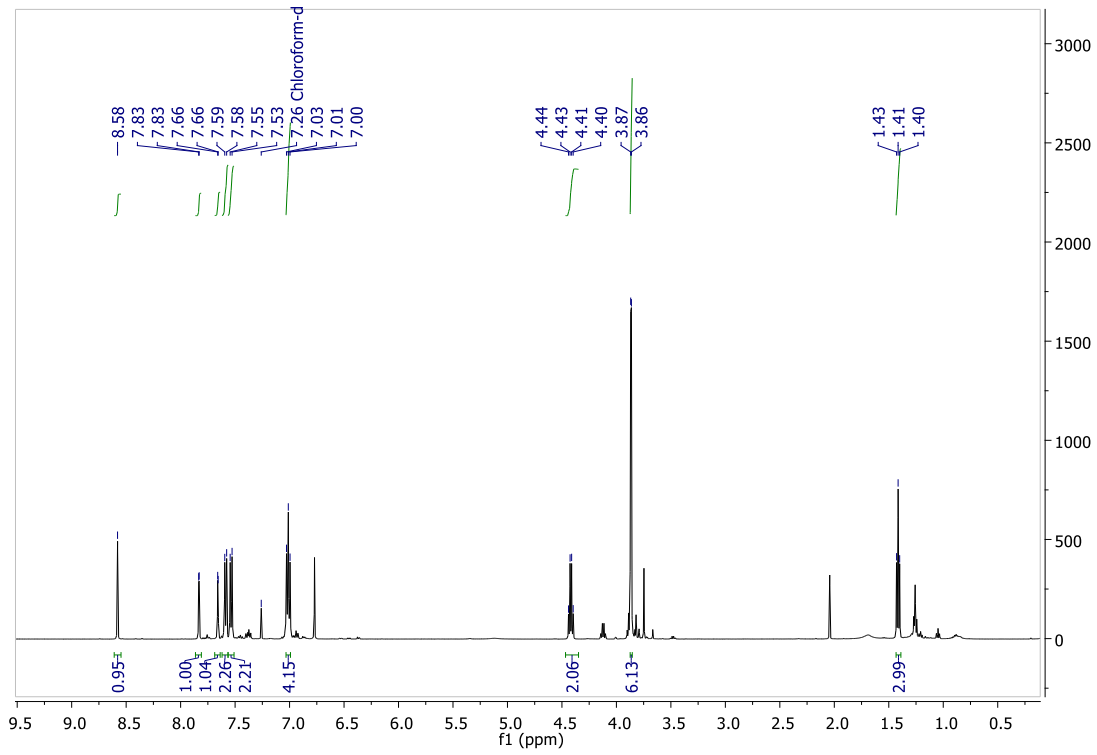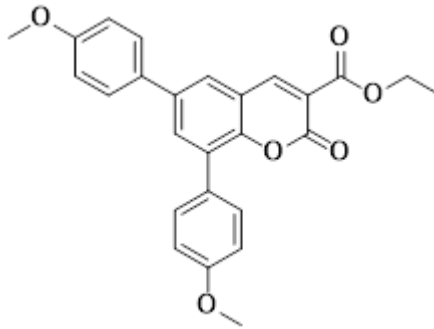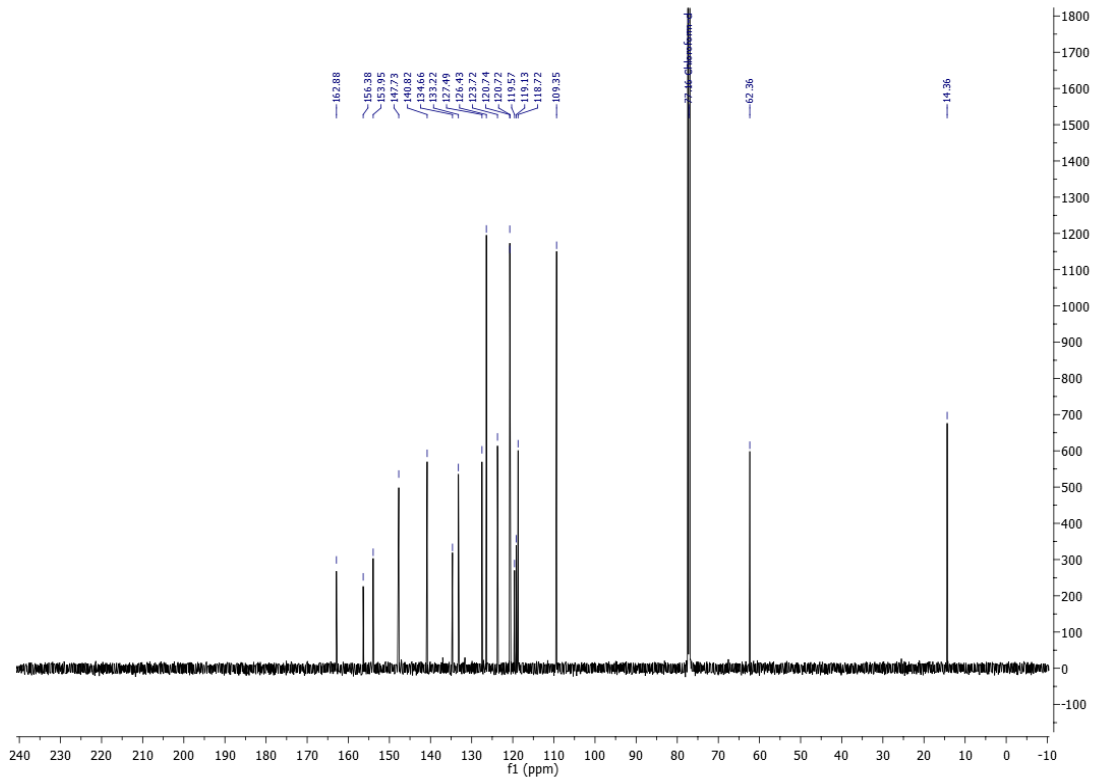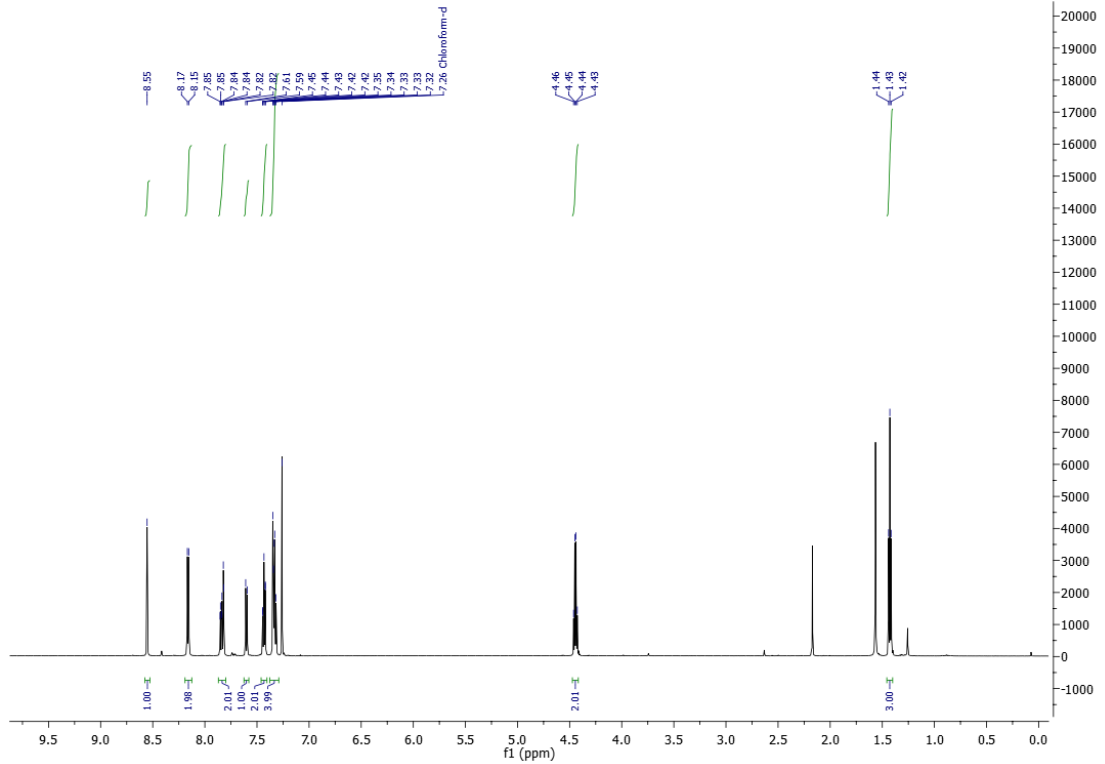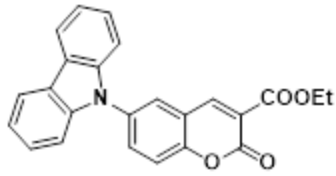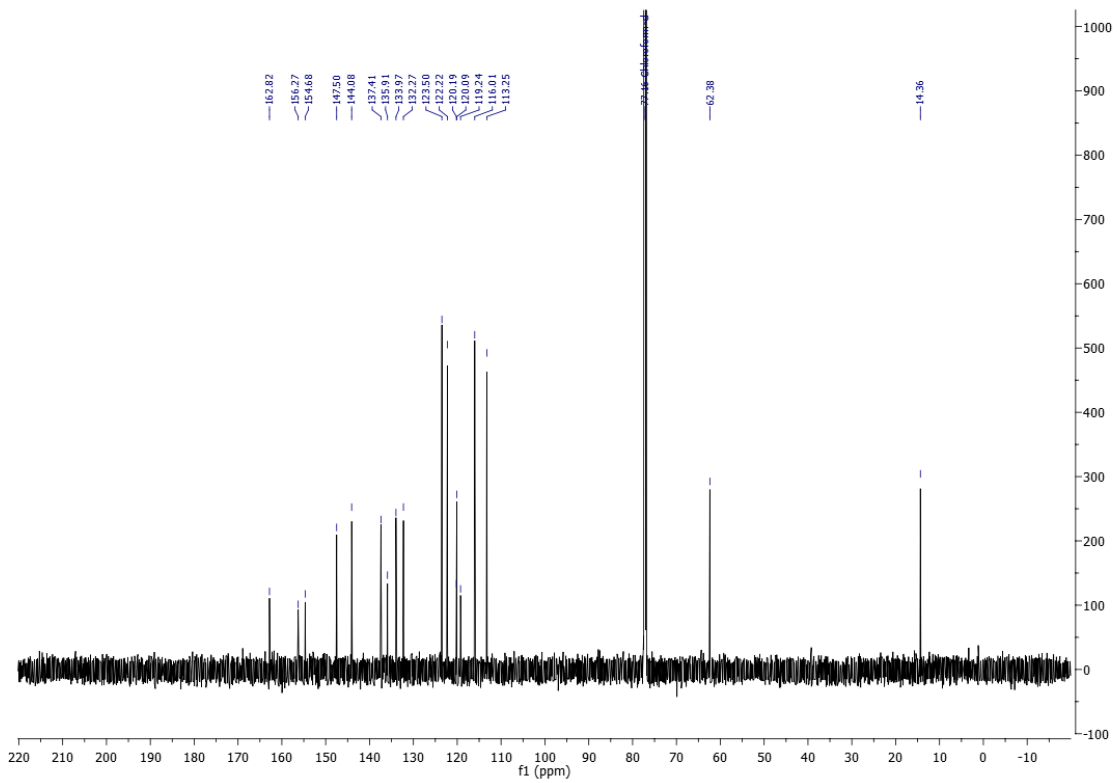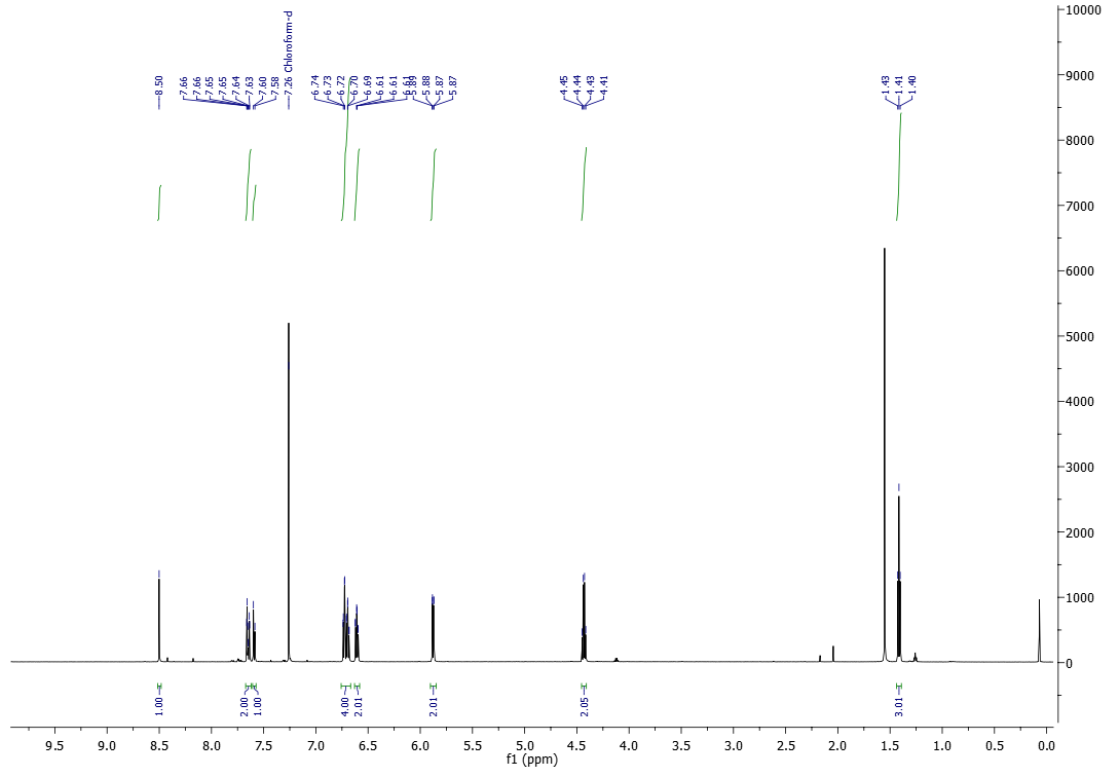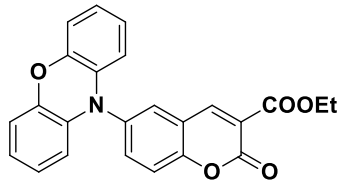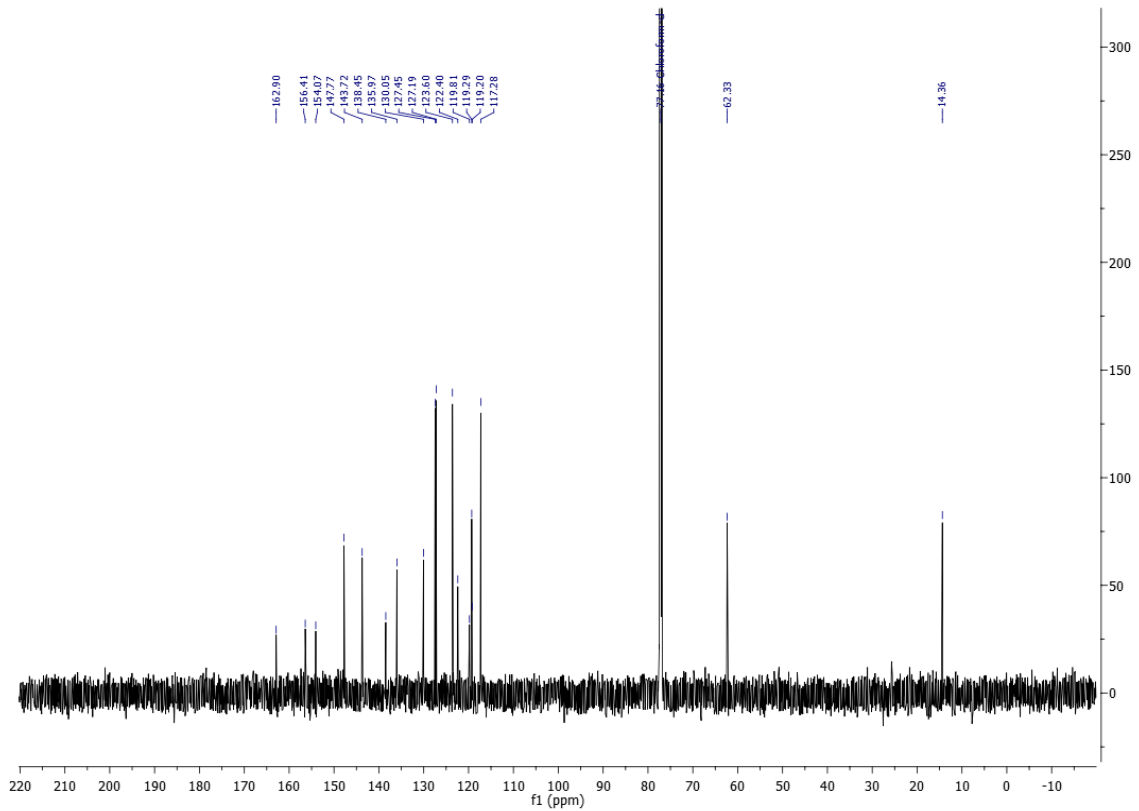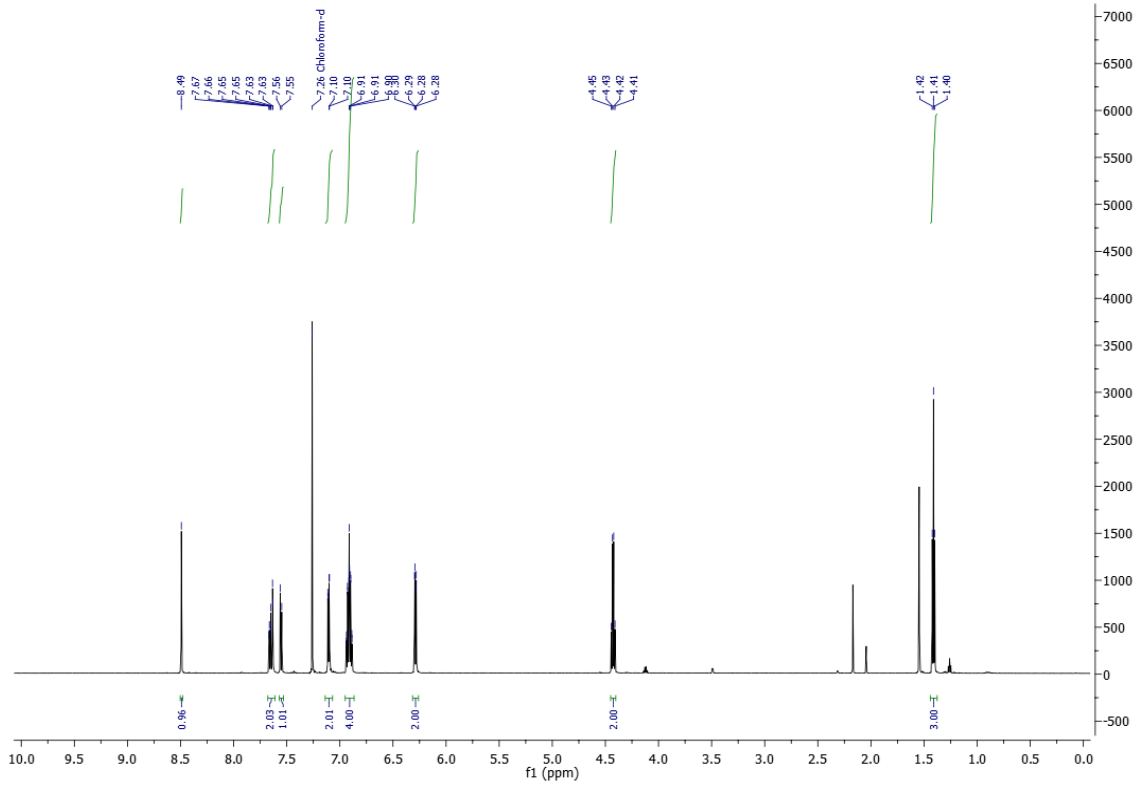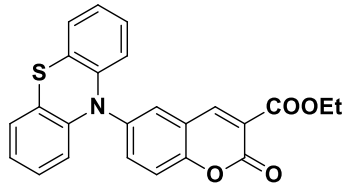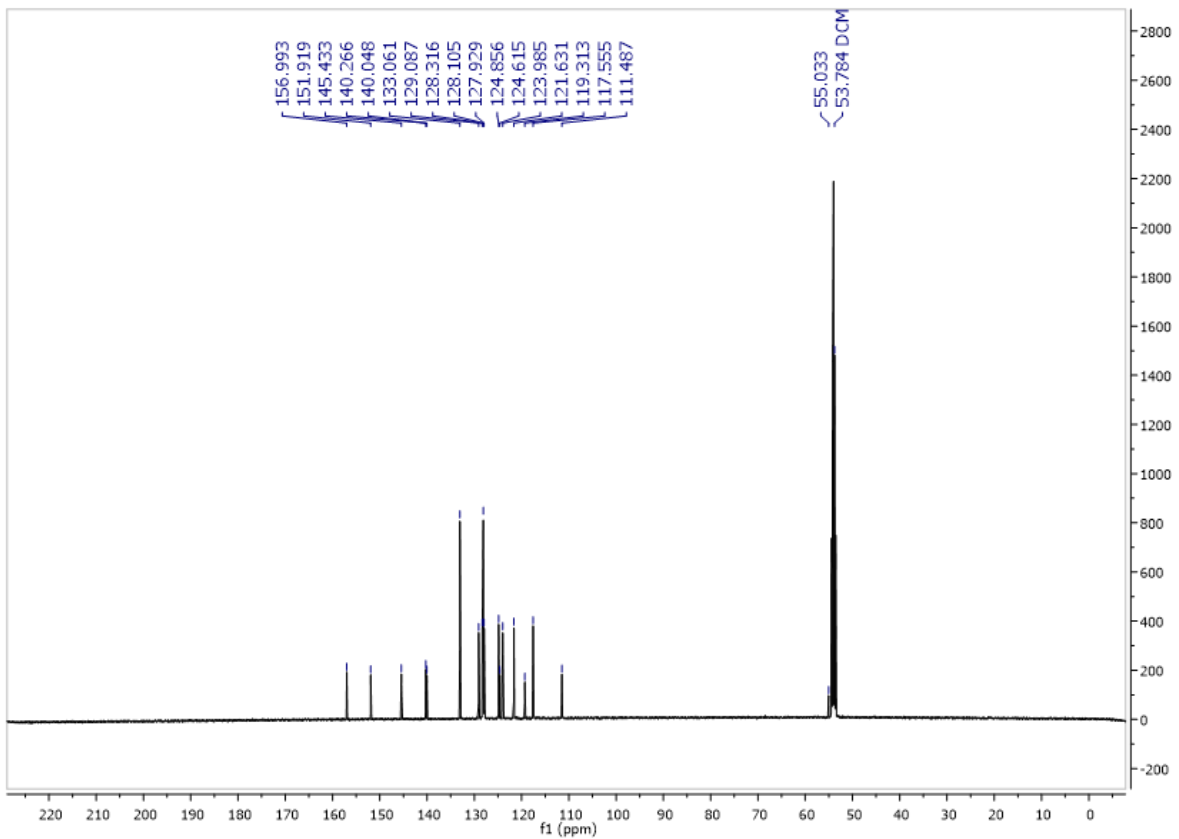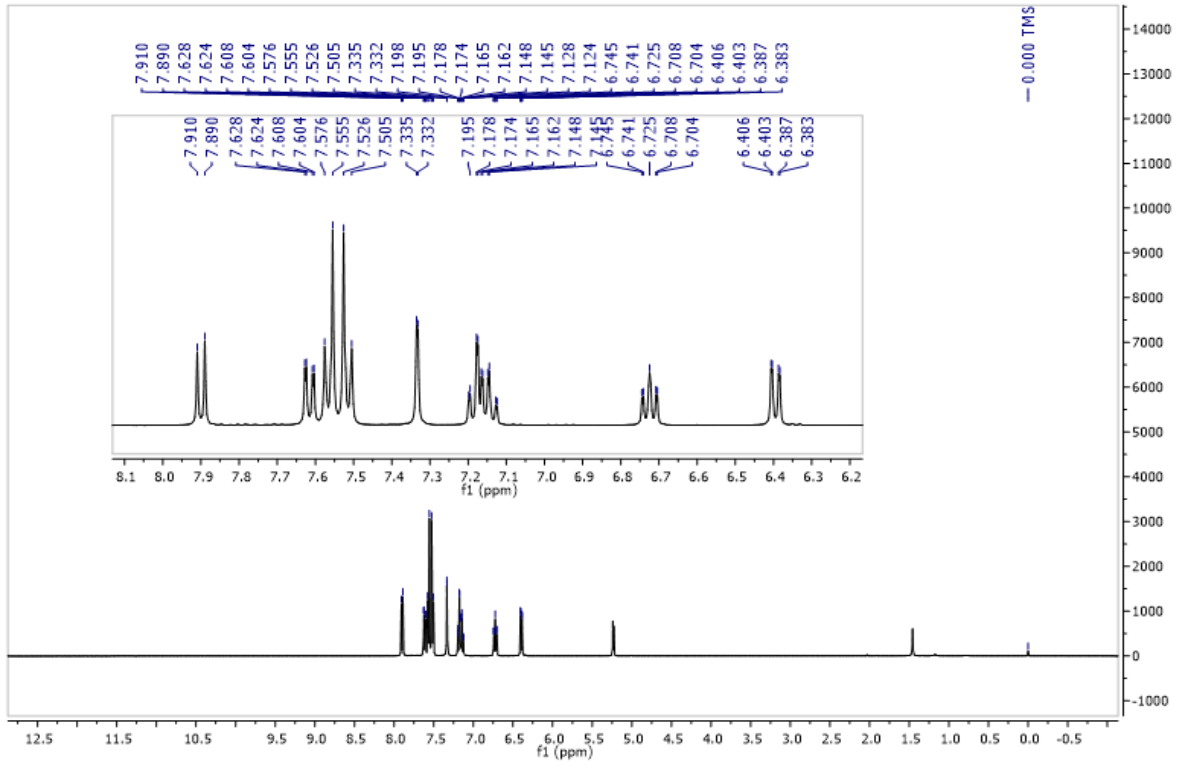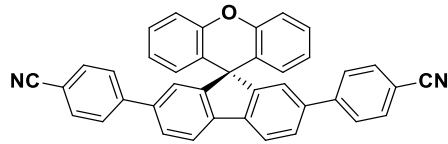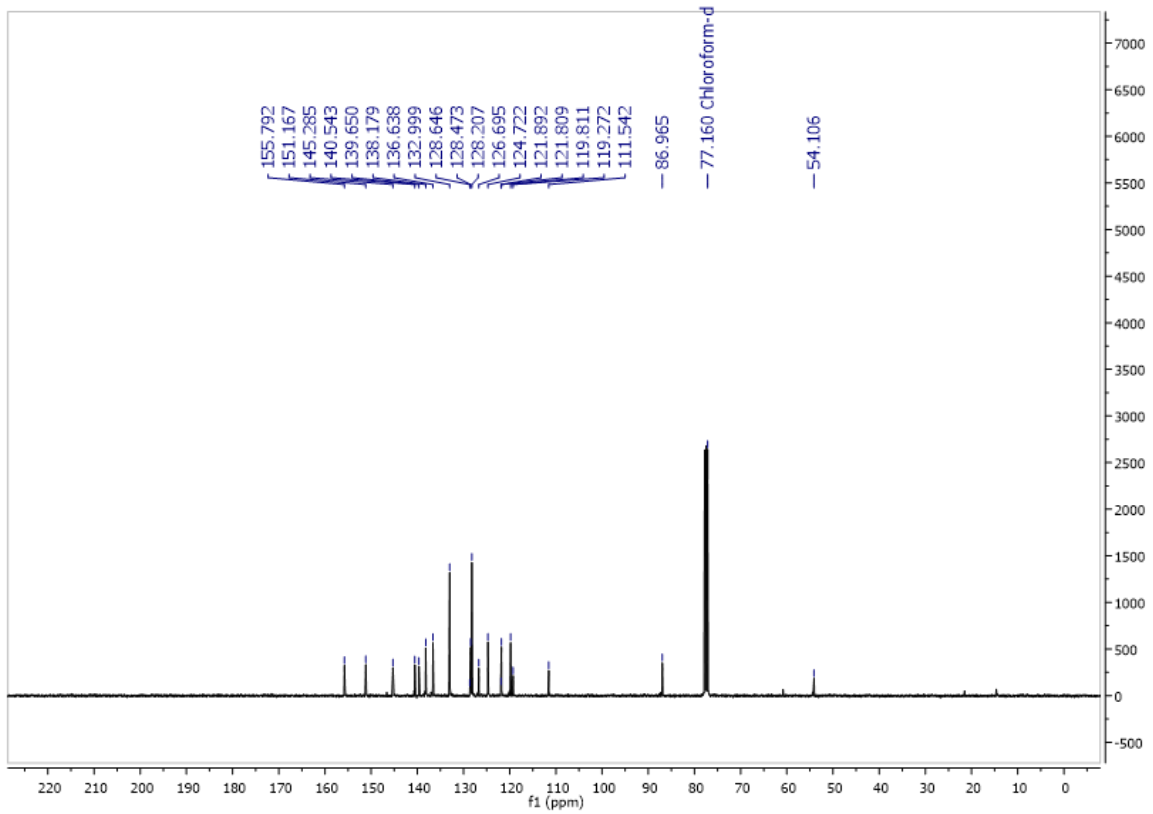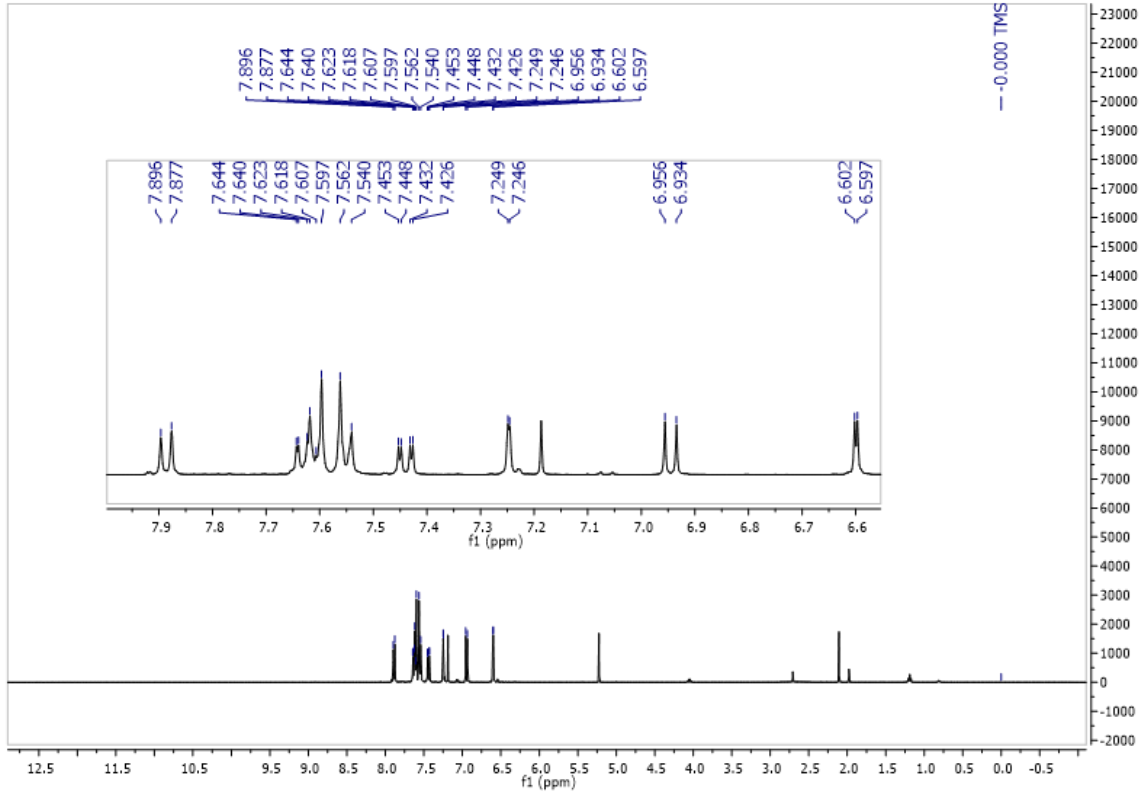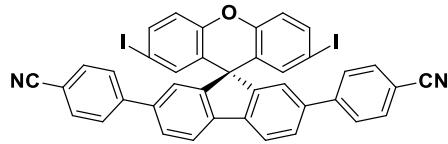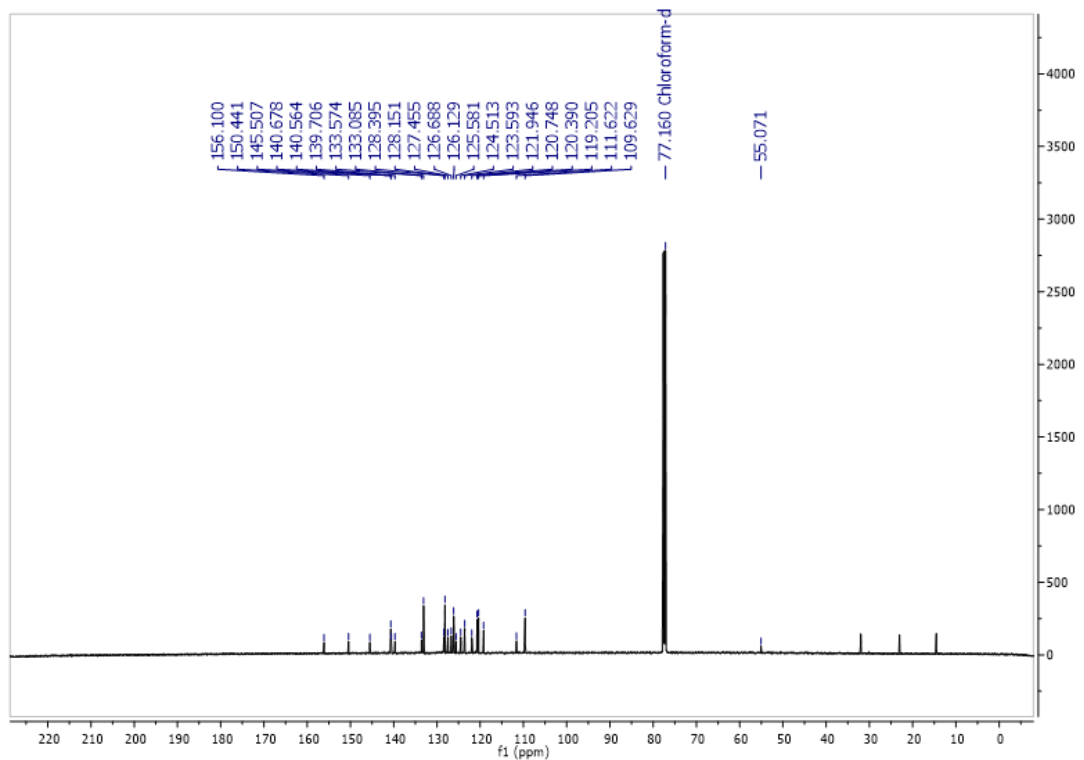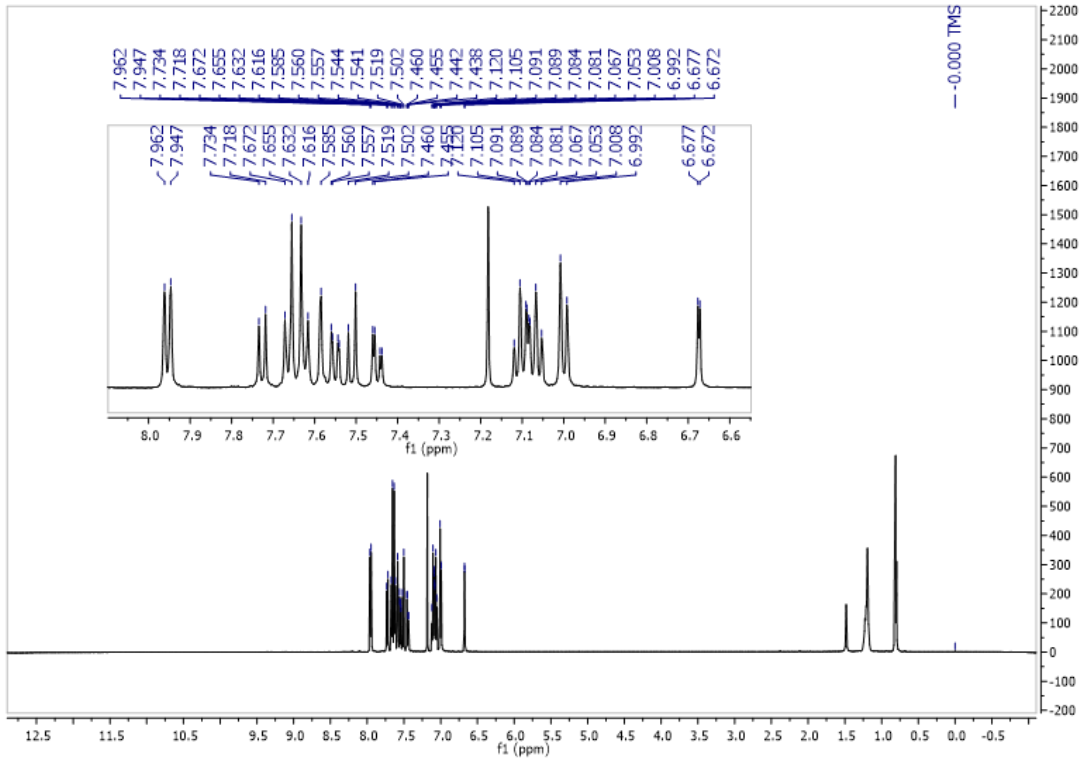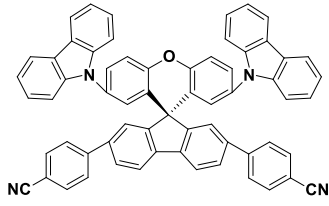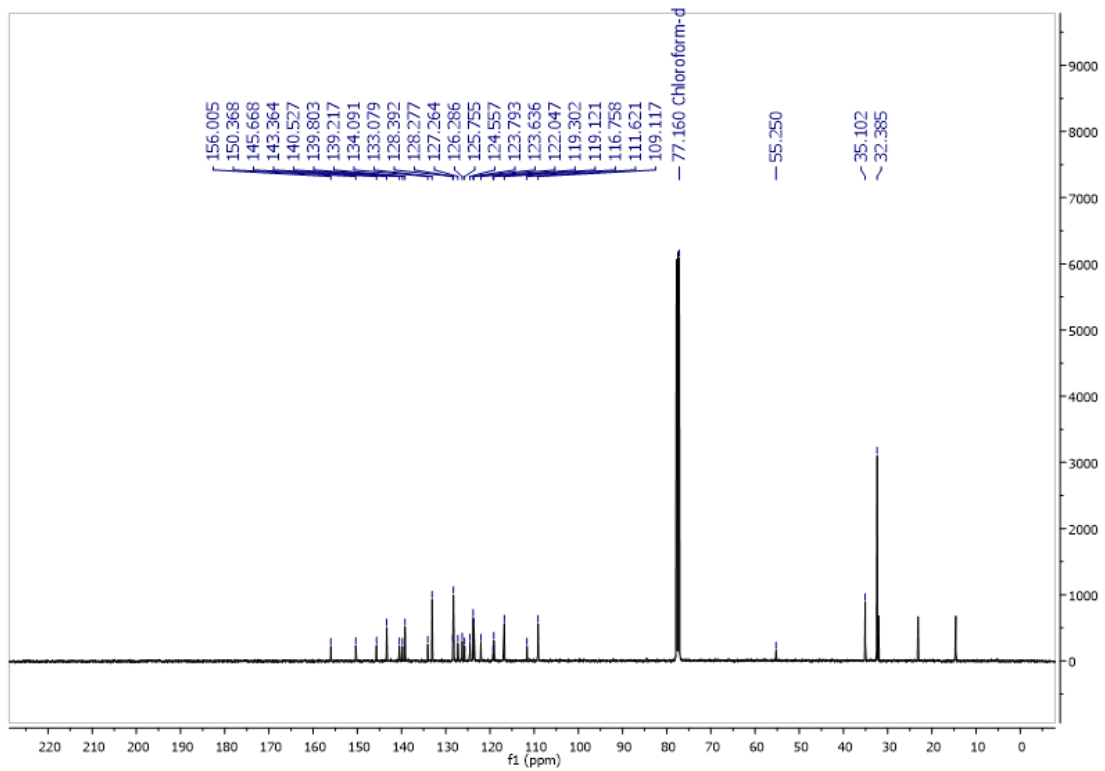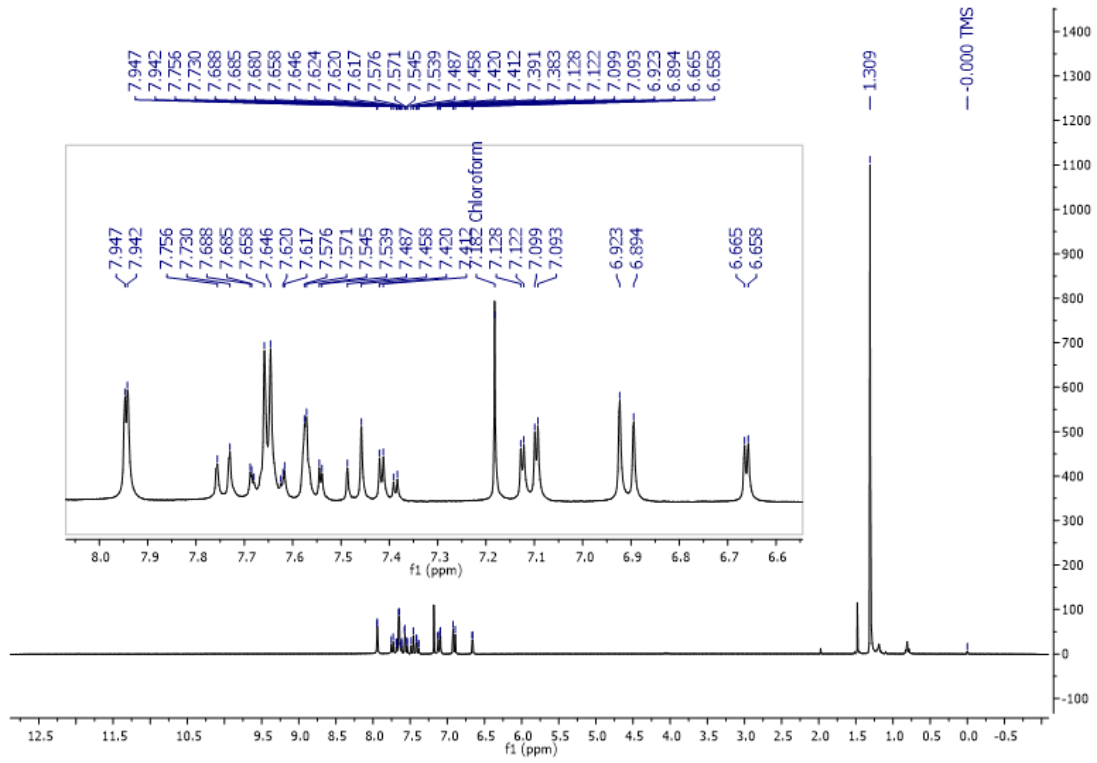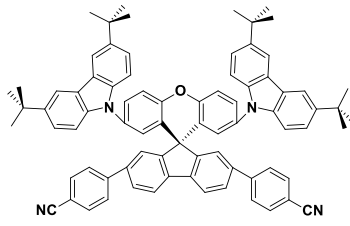
5.8 References

107. Frisch, M. J.; Trucks, G. W.; Schlegel, H. B.; Scuseria, G. E.; Robb, M. A.; Cheeseman, J. R.; Scalmani, G.; Barone, V.; Petersson, G. A.; Nakatsuji, H.; Li, X.; Caricato, M.; Marenich, A. V.; Bloino, J.; Janesko, B. G.; Gomperts, R.; Mennucci, B.; Hratchian, H. P.; Ortiz, J. V.; Izmaylov, A. F.; Sonnenberg, J. L.; Williams-Young, D.; Ding, F.; Lipparini, F.; Egidi, F.; Goings, J.; Peng, B.; Petrone, A.; Henderson, T.; Ranasinghe, D.; Zakrzewski, V. G.; Gao, J.; Rega, N.; Zheng, G.; Liang, W.; Hada, M.; Ehara, M.; Toyota, K.; Fukuda, R.; Hasegawa, J.; Ishida, M.; Nakajima, T.; Honda, Y.; Kitao, O.; Nakai, H.; Vreven, T.; Throssell, K.; Montgomery, J. A.; Peralta, J. E.; Ogliaro, F.; Bearpark, M. J.; Heyd, J. J.; Brothers, E. N.; Kudin, K. N.; Staroverov, V. N.; Keith, T. A.; Kobayashi, R.; Normand, J.; Raghavachari; ; Rendell, A. P.; Burant, J. C.; Iyengar, S. S.; Tomasi, J.; Cossi, M.; Millam, J. M.; Klene, M.; Adamo, C.; Cammi, R.; Ochterski, J. W.; Martin, R. L.; Morokuma, K.; Farkas, O.; Foresman, J. B.; Fox, D. J. Gaussian 16 revision c.01 **2016**, Gaussian Inc. Wallingford CT.

108. Cappai, A.; Melis, C.; Stagi, L.; Mocci, F.; Carbonaro, C.M. Insight into the Molecular Model in Carbon Dots through Experimental and Theoretical Analysis of Citrazinic Acid in Aqueous Solution. *J. Phys. Chem. C*, 2021, **125**, 4836–4845.

109. Mocci, F.; Olla, C.; Cappai, A.; Salis, M.; Carbonaro, C.M. Formation of citrazinic acid ions and their contribution to optical and magnetic features of carbon nanodots: A combined experimental and computational approach. *Materials*, 2021, **14**, 1–16.

110. Cancès, E.; Mennucci, B.; Tomasi, J. A new integral equation formalism for the polarizable continuum model: Theoretical background and applications to isotropic and anisotropic dielectrics. *J. Chem. Phys.* 1997, **107**, 3032–3041.

111. Crosby, G. A.; Demas, J. N., Measurement of Photoluminescence Quantum Yields. *Review. J. Phys. Chem.* 1971, **75** (8), 991-1024

112. Fischer, M.; Georges, J. Fluorescence quantum yield of rhodamine 6G in ethanol as a function of cocentration using thermal lens spectrometry. *Chem. Phys. Lett.* 1996, **260**, 115–118.

113. Greenham, N. C.; Samuel, I. D. W.; Hayes, G. R.; Phillips, R. T.; Kessener, Y. A. R. R.; Moratti, S. C.; Holmes, A. B.; Friend, R. H., Measurement of Absolute Photo-luminescence Quantum Efficiencies in Conjugated Polymers. *Chem. Phys. Lett.* 1995, **241** (1–2), 89-96.

114. Bruker (2016). APEX3, Bruker AXS Inc., Madison, Wisconsin, USA

115. Sheldrick, G.M., ShelXT-Integrated space-group and crystal-structure determina-tion, *Acta Cryst.*, (2015), **A71**, 3-8.

116. Sheldrick, G.M., Crystal structure refinement with ShelXL, *Acta Cryst.*, (2015), **C71**, 3-8.

117. O.V. Dolomanov, L.J. Bourhis, R.J. Gildea, J.A.K. Howard, H. Puschmann, Olex2: A complete structure solution, refinement and analysis program, *J. Appl. Cryst.*, (2009), **42**, 339-341.

Acknowledgments

First, I would like to thank my supervisor, Prof. Francesco Secci, for the guidance, encouragement and advice he has provided during my studies. His enthusiasm and confidence in my research motivated me a lot. My co-supervisors, Prof. Carlo Carbonaro and Prof. Carlo Ricci, which have helped me and have always answered my questions. In addition, all members of the research group of the Secci and co team for providing a stimulating and enjoyable environment to learn and grow.

Thanks to Prof. Eli Zysman-Colman for giving me the opportunity to work within his research group, which has been a pleasure and an honor for me, and guiding me all along through my research.

Also I want to thank my family and friends for their moral support.